NEW FRONTIERS FOR TRIPLE NEGATIVE BREAST CANCER DETECTION AND TREATMENT: FROM MECHANICAL BIOMARKERS TO SPECIFIC NANOPARTICLE ENTRY FOR ROBOTICALLY CONTROLLED LASER-INDUCED HYPERTHERMIA

VANESSA UZONWANNE

A DISSERTATION

PRESENTED TO THE FACULTY

OF WORCESTER POLYTECHNIC INSTITUTE

IN CANDIDACY FOR THE DEGREE

OF DOCTOR OF PHILOSOPHY

RECOMMENDED FOR ACCEPTANCE

BY THE DEPARTMENT OF

MATERIALS SCIENCE AND ENGINEERING

ADVISOR: PROFESSOR WINSTON O. SOBOYEJO

MAY 2022

Abstract

This thesis presents the results of a combined experimental, computational, and theoretical study of triple negative breast cancer (TNBC) cells and non-tumorigenic breast cells. It explores the interactions of these cells with biosynthesized gold nanoparticles (GNP), PEG-coated GNP (GNP-PEG), triptorelin functionalized GNP (GNP-TRP), and triptorelin-conjugated PEG-coated GNP (GNP-PEG-TRP) that are relevant to the treatment of triple negative breast cancer. Salient conclusions arising from the study of the adhesion, entry, and photothermal properties of GNP, GNP-PEG, GNP-TRP, and GNP-PEG-TRP in TNBC/non-tumorigenic cells are presented.

The adhesion is studied at the nanoscale using atomic force microscopy (AFM) experiments. The AFM measurements showed that the GNP-TRP and GNP-PEG-TRP have higher adhesion to TNBC than non-tumorigenic breast cells. The increased adhesion of GNP-TRP and GNP-PEG-TRP to TNBC is also attributed to the overexpression of LHRH receptors on the surfaces of TNBCs. Finally, a three to nine-fold increase in the adhesion is predicted between triptorelin-functionalized PEG-coated gold nanoparticles (GNP-PEG-TRP) and TNBC cells. Hence, the experimental observation indicates that specific receptor-ligand adhesion facilitates the targeting of TNBC cells with GNP-PEG-TRP. These results highlight the potential to develop Triptorelin functionalized PEG-coated gold nanoparticles into tumor-specific photothermal agents and drug carriers.

Next, the entry of GNP, GNP-PEG, GNP-TRP, and GNP-PEG-TRP into TNBC and non-tumorigenic cells were studied using in vitro nanoparticle entry experiments and thermodynamics-kinetics models to predict the wrapping times and optimal cluster size of uptake into TNBC cells. This nanoparticle entry study provides new insights into these biosynthesized nanoparticles' selectivity, clustering, wrapping time, and optimum sizes. In addition, these results highlight the role of receptor density distribution and cluster surface energy in nanoparticle uptake into TNBC and non-tumorigenic breast cells.

Specifically, the nanoparticle cluster size distribution results in TNBC (MDA-MB-231, MDA-MB-468) and non-tumorigenic breast cells (MCF 10A) were consistent with the theoretical models. Interestingly, the cluster size distribution of all nanoparticles in the cells increased as a function of metastatic cells. This increase in the cluster size distribution is attributed to the overexpression of LHRH receptors on the surfaces of both TNBC cells.

Lastly, this thesis presents an experimental and finite element (FE) study of the photothermal effects of GNP, GNP-PEG, GNP-TRP, and GNP-PEG-TRP in TNBC using in-vitro laser-nanoparticle hyperthermia (41°C - 45°C) experiments on TNBC cells and tissue models. The heating effects of near infrared (808 nm) laser interactions with the different gold nanoparticles are explored using a fluid and a tissue model. Also, the influence of robotics-assisted laser positioning on hyperthermic heating in tissue was investigated.

Results from the laser-nanoparticle interactions were validated using finite element analysis (FEA) and found to be consistent with the experimental results. Notably, all the biosynthesized gold nanoparticles achieved hyperthermia and thermal ablation temperatures in water. Furthermore, the photothermal conversion efficiency of the gold nanoparticles decreased with surface modification. Finally, the robotics-controlled laser positioning assisted heating in tissue reveals that axial and rotational laser interactions with the biosynthesized gold nanoparticles yield temperatures suitable for hyperthermia in tissue. The implications of the results are discussed for the development of a laser-nanoparticle-based medical robotics system for the specific hyperthermia treatment of TNBC.

Table of Contents

List of Figures

List of Tables

Acknowledgements

The completion of this thesis was made possible by the contributions of so many people, to whom I am grateful. I am thankful to God for Life and the opportunity I have had during this work.

First, my appreciation goes to my Advisor, Prof. W. O. Soboyejo for his mentorship, guidance, encouragement, constructive feedback and input towards the objectives of this work. I would like to thank the entire Soboyejo research group, especially Prof. John Obayemi, Prof. Ali Salifu and Jingjie Hu for introducing me to the various laboratory techniques and for their feedback at times when I had trouble making sense of various concepts. Also, my collaborators Prof. Nima Rahbar, Dr. Arvand Navabi and Dr. Habibeh Ashouri who enriched this thesis with their scientific contributions.

I would like to thank members of my thesis committee Prof. Nancy Burnham, Prof. Nima Rahbar, Prof. John Obayemi, and Prof. Ali Salifu for taking the time to read through my thesis and for providing constructive feedback. Special thanks go to Prof. Nancy Burnham for access to her Asylum AFM facility and Dr. Victoria Huntress for access to the confocal imaging facility at WPI. I am also grateful for the mental health and wellness support I received from the student counseling center at WPI.

A big thank you to my family, friends and church family, my support groups, for their love, support, and endless encouragement. I am grateful to the entire Materials Science and Engineering staff and student community and the administrative staff at WPI especially Ms. Kim Hollan, Ms. Pam St. Louis, Ms. Carrie West, Ms. Donna Zuidema, and Ms. Deb Graves.

Finally, I am thankful for the financial support from Worcester Polytechnic Institute, The Pan African Materials Institute of the African University of Science and Technology, and The World Bank African Centers of Excellence.

Chapter1.0. Background and Introduction

1.1 Background

1.1.1. Global Problem of Cancer

Cancer is the leading cause of death and reduced life expectancy globally [1]. In 2020, the global cancer statistics (GLOBACAN) estimated 19.3 million new cases and 10 million deaths. Globally, the cancer burden is expected to increase by 47% in 2040[1].

Despite the progress made in treatment and detection methods, detracting factors such as poor health infrastructure and late-stage cancer presentation in developing countries, resolution limitations in detection equipment for early detection, cancer drug resistance, and systemic treatment side effects present opportunities for more research.

1.1.2. Triple Negative Breast Cancer

Breast cancer in females was reported as the leading cause of global cancer incidence in 2020, accounting for over 2.3 million new cases[1].

Triple Negative Breast Cancer (TNBC) is classified as a sub-group of breast cancer that does not overexpress progesterone, estrogen, and Her 2 negative [2]. It accounts for 15% of female breast cancer diagnoses [3].TNBC is commonly diagnosed amongst women of African and African American descent with BRCA 1 mutation carriers [2][4]. It is very aggressive and, to date, has a poor prognosis[2]. Clinical and pathological studies have shown that despite an increase in the response rates for neoadjuvant treatment, TNBC patients experience a significantly decreased disease-free survival (DFS) and overall survival (OS) compared to other cancer subtypes[2][4]. Although certain TNBCs are sensitive to current chemotherapy, these patients still experience high tumor reoccurrence and relapse[4]. Unfortunately, over 50% of TNBC patients with poor OS do not benefit from the available endocrine therapy[2]. Hence, early diagnostic tools are needed to discriminate between chemoresistant TNBC patients and therapeutic tools to cater to this group[2]. Many targeted therapies are being explored to improve the poor prognosis of TNBC. Such treatments include the use of poly(adenosine diphosphate ribose) polymerase (PARP) inhibitors to prevent DNA damage repair, antiangiogenic therapy for targeting vascular endothelial growth factor (VEGF), and using epidermal growth factor receptor (EGFR) inhibitors to disrupt tumor progression, improve OS and DFS of TNBC patients[2][4]. Others include Luteinizing Hormone Releasing Hormone (LHRH) based targets done by our group over a few decades[5]–[9].

1.1.3. The Challenges of Cancer Detection and Treatment

Cancer diagnosis requires precise imaging tools for screening tissue and biopsy to distinguish between benign and malignant tissue[10]. Mammography is the most used screening method for breast cancer detection but is less effective for subjects less than 40 years old due to the denser nature of the breast tissue[11]. Mammography can also not track cancer progression or therapeutic effects on the tumor and is less sensitive to tumor sizes less than 1mm; thus, early detection of breast cancer is limited [10]. Contrast-enhanced digital mammography offers more diagnostic accuracy than mammography and ultrasound in denser tissue, but this is not very accessible due to its cost and the high radiation levels associated with the diagnostic process[12]. Early detection has been identified as a critical point to providing a better prognosis and ultimately lower mortality rates for cancer patients[13]. Although Magnetic Resonance Imaging (MRI) can detect smaller tumor sizes(<1mm), it has low specificity to malignant tissue, which often leads to overdiagnosis [14]. Positron emission tomography (PET) is currently the most popular method for visualizing tumor progression and their response to therapy, but they are costly and have a resolution of 4mm[15].

Molecular biomarker-based biopsy methods are commonly used due to their relative sensitivity and selectivity[10]. For Instance, techniques such as radioimmunoassay, immunohistochemistry, enzyme-linked immunosorbent assay (ELISA), and fluoroimmunoassay have been used in the biopsy process[10]. However, these methods involve complex labeling techniques that are time-consuming, expensive, and require skilled personnel[13]. Thus, there is an urgent need to develop highly sensitive, selective, and label-free methods for rapid cancer diagnosis.

1.2. Unresolved Issues

1.2.1. Cancer Detection

Despite the vast number of cancer biomarkers being identified, only a few have been approved for use by the FDA[16][17]. To be effective, cancer biomarkers need to distinguish between people with cancer (sensitivity) and people without cancer(specificity). An Ideal cancer biomarker should be measurable and have 100% sensitivity and specificity[17]. It should also indicate normal biological processes, disease processes, and therapeutic responses over time[18]. Unfortunately, none of the available biomarkers have 100% sensitivity and selectivity[16]. For example, the CA15.3 breast cancer biomarker currently has only 23% sensitivity and 69% specificity; hence, it is only useful for monitoring therapeutic response and reoccurrence[16]. Prostate-specific antigen (PSA) has the best sensitivity (>90%) but low specificity (~25%), leading to overdiagnosis [19][16]. Furthermore, most detection methods cannot identify early-stage cancer or micro-sized metastasis, crucial for aggressive cancers like TNBC[16]. Tumor heterogeneity is also an important factor that detracts from the development of biomarkers. Most biomarkers are measured by genetics, proteomics, or cellular molecular substances. One tumor mass can contain several types of the clonal population, each with different mutations and phenotypes[13]. This heterogeneity in tumor cells also varies based on stage/age of cancer (new or recurrent) and tumor DNA instability from exposure to treatment[13].

Thus, there is an urgent need to develop highly sensitive, selective, and label-free methods for rapid cancer diagnosis.

Prior work done by our group focused on exploring mechanical biomarkers by measuring TNBC viscoelastic properties (modulus, viscosity, and relaxation time) and assessing their use as diagnostic discriminators between TNBC and normal breast cells[20].

1.2.2. Localized treatment

The standard cancer treatment plan for intermediate stage cancer involves tumor resection followed by adjuvant treatments such as chemotherapy and or radiation therapy for very aggressive cancer types[21]. The long-term side effects of these adjuvant therapies do not allow for positive overall survival of the patient[22]. Hence the emergence of various drug delivery studies. These efforts work to increase the bioavailability and concentration of chemotherapy drugs at the tumor site[21]. One approach being considered is the systemic delivery of nanomaterials. These nanomaterials find tumors by passive diffusion through the leaky tumor vasculature, active targeting via bioconjugation to a molecule with high affinity for over-expressed tumor biomarker, or by environment (pH, temperature) triggered drug release[21][23]. Most nanomaterials are intended to be delivered intravenously, but localization of the nanomaterials at therapeutic concentrations is challenging due to the removal and sequestration of these nanomaterials by the reticuloendothelial system and uptake by non-targeted cells or other non-specific interactions. [23][21].

Another delivery approach uses polymeric controlled release drug delivery reservoir systems such as drug-eluting films and gels. These are designed to be implanted intratumorally or inserted after initial tumor resection[23]. Despite this progress, localized treatment with implantable drug delivery systems becomes problematic in cases of metastasis to other cellular tissue or the lymph nodes.

1.2.2.1. Targeted Drugs

The increasing sophistication of sequencing technologies has generated extensive genomic data intended for cancer drug formulation and targeted therapy[24]. Despite this feat, very few of these have translated to advanced clinical studies[24][13]. This is mainly due to tumor heterogeneity and acquired drug resistance. First, these genetic mutations are often too specific when used in the formulation of cancer drugs; thus, they only apply to a particular subset of patients[24]. The second is the difficulty in meeting the critical number of cases for valid randomized clinical studies and the cost of running such a study. In some instances, identified mutations represent only 1-5% of all patients and may not be feasible in rare tumors [24]. Perhaps looking at targets that are more generalized but still specific to tumors, such as overexpressed receptors, might help with drug resistance issues and provide enough cases for randomized trials.

1.2.2.2. Targeted Nanoparticles

Nanoparticles are considered for targeted cancer treatment due to their small size, surface modification capabilities, which enable a large array of requirements to be met, ability to overcome biological barriers such as the blood-brain barrier, as is the case of gold nanoparticles [25], and potential to push past the problem of multidrug resistance in cancer therapies[26].

Coating gold nanoparticles with polyethylene glycol (PEG) prevents the uptake of the nanoparticles by the reticuloendothelial system (RES) clearance in the body, thus prolonging their circulation time while increasing their concentration in tumor tissue [27]. The size dependence of nanoparticles is also an important factor as extremely small particles less than 10 nm can be removed by the kidney, while larger particles greater than 200 nm are removed by the mononuclear phagocyte system [28]. At the cellular level, nanoparticles can be internalized through receptor-mediated endocytosis processes [29][30].

1.2.2.3. Targeted/ Localized Heat Delivery

The use of hyperthermia in cancer therapy is advantageous due to its minimal side effect and potential to improve the therapeutic effects of conventional cancer therapies[31][32]. Despite the advantages of hyperthermia therapy, the challenge of heating only malignant cells remains daunting. Interstitial hyperthermia such as radiofrequency (RF) electrode needles, microwave antennas and inductively heated ferromagnetic implants have been explored in various studies[33][34][35][32]. But issues of biocompatibility and corrosion associated with these methods are detractors to their long term use[36][37][32]. Also the use of inductively heated ferromagnetic implants requires high density of thermoseeds [38].

Our group has studied stimuli responsive polymeric nanocomposites to mitigate biocompatibility and corrosion issues common with metallic implants. This was done by fabricating nanocomposites using plasmonic nanomaterials such as magnetite and gold in combination with polymer matrices[32][35][39]. Interacting these nanocomposite with laser in the near infrared region (NIR) localizes heating within the region of implantation[32][35][39].

Another approach our group is exploring used PEGylated Molecularly labeled nanoparticles that can be localized in tumor or near tumor surroundings. Because of their size, these nanoparticles are intended for applications where targeting both primary and metastasized tumor or tumors that are difficult to resection is a priority.

1.3. Scope of Thesis

This thesis focuses on the Adhesion and entry of targeted gold nanoparticles into TNBC cells and Tissues.

This Includes studies of the adhesion of biosynthesized GNP and it's polyethylene glycol (PEG) and triptorelin ligand modified forms; entry and the interaction of such with lasers for in vitro conditions. These would be addressed in the scope of this thesis which includes:

The introduction in Chapter 1 and a literature review in Chapter 2. This presents relevant literature on functionalized gold nanoparticles for targeted cancer therapy; atomic force microscopy (AFM) principles; nanoparticle entry pathways; and current techniques for cell mechanical properties. In Chapter 3, the synthesis, characterization, and conjugation process of Triptorelin PEG-coated GNPs is discussed. The combined AFM adhesion experiments and molecular dynamics (MD) simulations are also detailed in this chapter to provide new insights into the adhesive interactions between Triptorelin PEG-coated GNPs and TNBC.

In chapter 4, experimental and theoretical studies of GNP entry into TNBC are discussed. Subsequently, Chapter 5 details the near-infrared NIR laser interactions with various GNPs, highlighting the effects of surface coatings on the photothermal efficiency of these nanoparticles and their impact on cell viability. Additionally, comparisons are made between two robotics-assisted laser positioning devices (a modified 3D printer nozzle and a robotic arm with six degrees of freedom) for uniform heat distribution within a chicken tissue model.

Finally, Chapter 6 presents salient conclusions arising from this study and suggestions for future work.

1.4. References

[1] H. Sung et al., “Global Cancer Statistics 2020: GLOBOCAN Estimates of Incidence and Mortality Worldwide for 36 Cancers in 185 Countries,” CA. Cancer J. Clin., vol. 71, no. 3, pp. 209–249, 2021.

[2] O. Gluz, C. Liedtke, N. Gottschalk, L. Pusztai, U. Nitz, and N. Harbeck, “Triple-negative breast cancer - Current status and future directions,” Ann. Oncol., vol. 20, no. 12, pp. 1913–1927, 2009.

[3] W. D. Foulkes, I. E. Smith, and J. S. Reis-Filho, “Triple-Negative Breast Cancer,” 2010.

[4] W. J. Irvin and L. A. Carey, “What is triple-negative breast cancer ?,” Eur. J. Cancer, vol. 44, no. 18, pp. 2799–2805, 2008.

[5] J. Zhou, C. Leuschner, C. Kumar, J. Hormes, and W. O. Soboyejo, “A TEM study of functionalized magnetic nanoparticles targeting breast cancer cells,” Mater. Sci. Eng. C, vol. 26, no. 8, pp. 1451–1455, 2006.

[6] J. D. Obayemi et al., “Adhesion of ligand-conjugated biosynthesized magnetite nanoparticles to triple negative breast cancer cells,” J. Mech. Behav. Biomed. Mater., vol. 68, no. January, pp. 276–286, Apr. 2017.

[7] J. Meng, E. Paetzell, a. Bogorad, and W. O. Soboyejo, “Adhesion between peptides/antibodies and breast cancer cells,” J. Appl. Phys., vol. 107, no. 11, p. 114301, 2010.

[8] J. Hu, S. Youssefian, J. Obayemi, K. Malatesta, N. Rahbar, and W. Soboyejo, “Investigation of adhesive interactions in the specific targeting of Triptorelin-conjugated PEG-coated magnetite nanoparticles to breast cancer cells,” Acta Biomater., vol. 71, no. February, pp. 363–378, 2018.

[9] Y. Oni et al., “Gold nanoparticles for cancer detection and treatment: The role of adhesion,” J. Appl. Phisics, vol. 115, no. 084305, pp. 1–9, 2014.

[10] L. Wang, “Early diagnosis of breast cancer,” Sensors (Switzerland), vol. 17, no. 7, 2017.

[11] H. D. Nelson, K. Tyne, A. Naik, C. Bougatsos, B. K. Chan, and L. Humphrey, “Screening for breast cancer: An update for the U.S. Preventive Services Task Force,” Annals of Internal Medicine, vol. 151, no. 10. pp. 727–737, 2009.

[12] M. B. I. Lobbes, M. L. Smidt, J. Houwers, V. C. Tjan-Heijnen, and J. E. Wildberger, “Contrast enhanced mammography: Techniques, current results, and potential indications,” Clin. Radiol., vol. 68, no. 9, pp. 935–944, Sep. 2013.

[13] E. R. Sauter, “Reliable Biomarkers to Identify New and Recurrent Cancer,” Eur. J. Breast Heal., vol. 13, no. 4, pp. 162–167, 2017.

[14] Z. Zhou et al., “MRI detection of breast cancer micrometastases with a fibronectin-targeting contrast agent,” Nat. Commun., vol. 6, 2015.

[15] E. E. Yusuf, “Limits of Tumor Detectability in Nuclear Medicine and PET,” Malecular Imaging Radionucl. Ther., vol. 21, no. 2, pp. 23–28, 2012.

[16] U. Manne, R. G. Srivastava, and S. Srivastava, “Keynote review: Recent advances in biomarkers for cancer diagnosis and treatment,” Drug Discov. Today, vol. 10, no. 14, pp. 965–976, 2005.

[17] A. K. Füzéry, J. Levin, M. M. Chan, and D. W. Chan, “Translation of proteomic biomarkers into FDA approved cancer diagnostics: Issues and challenges,” Clin. Proteomics, vol. 10, no. 1, 2013.

[18] FDA-NIH Biomarker Working, “BEST (Biomarkers , EndpointS , and other Tools) Resource.” 2016.

[19] D. Gillatt and J. Reynard, “What is the ‘normal range’ for prostate-specific antigen? Use of a receiver operating characteristic curve to evaluate a serum marker.,” Br J Urol. 1995, vol. 75(3), pp. 341–6, 1995.

[20] J. Hu, Y. Zhou, J. D. Obayemi, J. Du, and W. O. Soboyejo, “An investigation of the viscoelastic properties and the actin cytoskeletal structure of triple negative breast cancer cells,” J. Mech. Behav. Biomed. Mater., 2018.

[21] J. B. Wolinsky, Y. L. Colson, and M. W. Grinstaff, “Local drug delivery strategies for cancer treatment: Gels, nanoparticles, polymeric films, rods, and wafers,” J. Control. Release, vol. 159, no. 1, pp. 14–26, 2012.

[22] C. Pucci, C. Martinelli, and G. Ciofani, “Innovative approaches for cancer treatment: Current perspectives and new challenges,” Ecancermedicalscience, vol. 13, pp. 1–26, 2019.

[23] A. A. Exner and G. M. Saidel, “Drug-eluting polymer implants in cancer therapy,” Expert Opin. Drug Deliv., vol. 5, no. 7, pp. 775–788, 2008.

[24] J. Zugazagoitia, C. Guedes, S. Ponce, I. Ferrer, S. Molina-Pinelo, and L. Paz-Ares, “Current Challenges in Cancer Treatment,” Clin. Ther., vol. 38, no. 7, pp. 1551–1566, 2016.

[25] J. F. Hainfeld, L. Lin, D. N. Slatkin, F. Avraham Dilmanian, T. M. Vadas, and H. M. Smilowitz, “Gold nanoparticle hyperthermia reduces radiotherapy dose,” Nanomedicine Nanotechnology, Biol. Med., vol. 10, no. 8, pp. 1609–1617, 2014.

[26] A.K. Larsen, A.E. Escargueil, and A. Skladanowski, “Resistance mechanisms associated with altered intracellular distribution of anticancer agents,” Pharmacol. Ther., vol. 85, no. 3, pp. 217–229, 2000.

[27] J. C. Y. Kah et al., “Critical parameters in the pegylation of gold nanoshells for biomedical applications: An in vitro macrophage study,” J. Drug Target., vol. 17, no. 3, pp. 181–193, 2009.

[28] A. Rodzinski et al., “Targeted and controlled anticancer drug delivery and release with magnetoelectric nanoparticles,” Nat. Publ. Gr., no. November 2015, pp. 1–14, 2016.

[29] J. Meng et al., “LHRH-functionalized superparamagnetic iron oxide nanoparticles for breast cancer targeting and contrast enhancement in MRI,” Mater. Sci. Eng. C, vol. 29, no. 4, pp. 1467–1479, 2009.

[30] H. Gao, W. Shi, and L. B. Freund, “Mechanics of receptor-mediated endocytosis,” Proc. Natl. Acad. Sci., vol. 102, no. 27, pp. 3–8, 2005.

[31] P. Cherukuri, E. S. Glazer, and S. A. Curley, “Targeted hyperthermia using metal nanoparticles,” Adv. Drug Deliv. Rev., vol. 62, no. 3, pp. 339–345, 2010.

[32] K. Kan-Dapaah, N. Rahbar, and W. Soboyejo, “Implantable magnetic nanocomposites for the localized treatment of breast cancer,” J. Appl. Phys., 2014.

[33] T. Nguyen, E. Hattery, and V. P. Khatri, “Radiofrequency ablation and breast cancer: a review.,” Gland Surg., vol. 3, no. 2, pp. 128–12835, 2014.

[34] T. P. Ryan and C. L. Brace, “Interstitial microwave treatment for cancer: historical basis and current techniques in antenna design and performance,” International Journal of Hyperthermia, vol. 33, no. 1. pp. 3–14, 2017.

[35] K. Kan-Dapaah, N. Rahbar, A. Tahlil, D. Crosson, N. Yao, and W. Soboyejo, “Mechanical and hyperthermic properties of magnetic nanocomposites for biomedical applications,” J. Mech. Behav. Biomed. Mater., vol. 49, no. April, pp. 118–128, 2015.

[36] R. F. Brem, “Radiofrequency ablation of breast cancer: A step forward,” Radiology, vol. 289, no. 2, pp. 325–326, 2018.

[37] E. Tammam, A. M. Said, A. A. Ibrahim, and A. I. A. Galal, “About the interstitial microwave cancer ablation: Principles, advantages and challenges,” IEEE Access, vol. 8, pp. 49685–49694, 2020.

[38] A. Baeza, D. Arcos, and M. Vallet-Regí, “Thermoseeds for interstitial magnetic hyperthermia: From bioceramics to nanoparticles,” J. Phys. Condens. Matter, vol. 25, no. 48, 2013.

[39] Y. Danyuo et al., “Laser Application of Nanocomposite Hydrogels on Cancer Cell Viability,” MRS Adv., vol. 5, no. 26, pp. 1377–1385, 2020.

Chapter 2.0. Literature Review

2.1. Introduction

This chapter presents a review of the relevant literature to this work. It includes an overview of cancer biology and selected techniques for measuring cell viscoelastic properties and adhesion. The chapter concludes with an overview of the current cancer treatment methods and discusses the receptor-mediated mechanisms by which nanoparticles enter biological cells.

2.2. Cancer Biology

Cancer is a collective term used to describe a diseased state characterized by uncontrolled cell division and growth[1]. The word tumor represents a collective of abnormal cells that can be benign or malignant. Malignant tumors usually lead to life-threatening situations and are more likely to metastasize throughout the body[1]–[3].

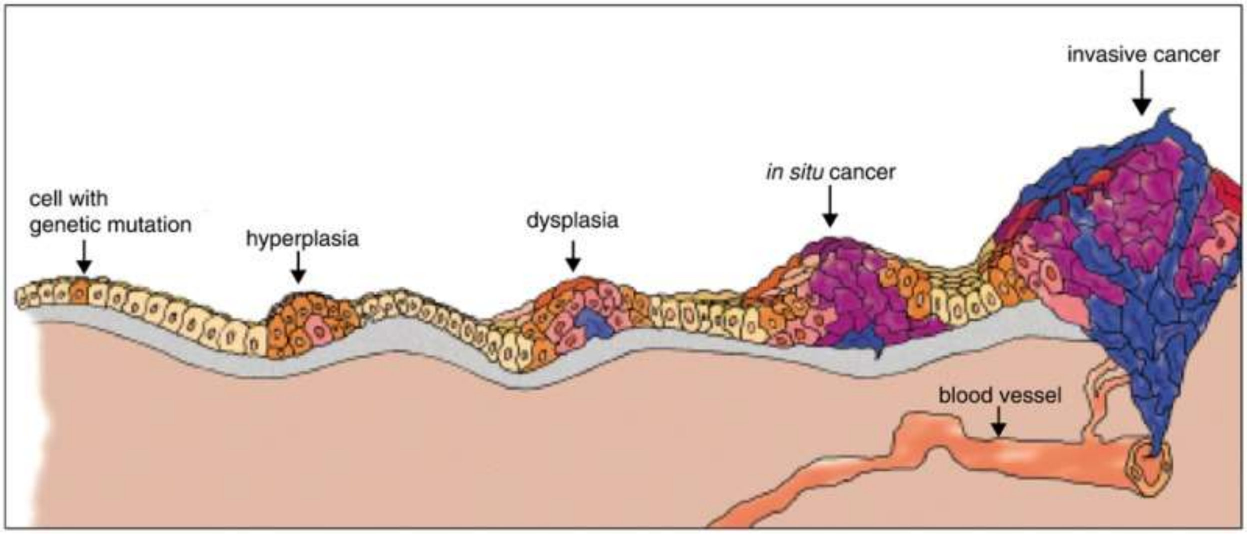

Fig. 2.1. The stages of tumor development [3].

Fig.2.1. shows a schematic of the various stages of malignant tumor development. Although it (Fig.2.1) depicts a sequence of four mutations from a normal cell to a fully malignant cell, the number of gene mutations involved in actual tumors varies. Tumor development starts when a cell (orange) undergoes a genetic mutation that triggers abnormal cell division. The mutated cell proliferates rapidly while maintaining a normal cell appearance and orientation(hyperplasia). After some years, another cell (pink) suffers further mutation and loss of normal cell regulation. In addition to proliferating uncontrollably, the appearance and orientations of these cells deviate from the standard cell shape and orientation(dysplasia). At this deviated state, the tumor can remain contained in its tissue of origin(in situ) or experience further mutations that trigger the invasion of adjacent tissues or escape into the bloodstream or lymph, fostering metastases and damage to vital organs [3].

2.3. Structure and Properties of Cancer Cells

Biological cells are dynamic units that adapt to changes in their typical chemo-mechanical environment and diseased state[4]–[6]. Therefore, the cell cytoskeletal network is a significant feature of the cell. Cell cytoskeletal structures are composed of actin filaments, microtubules, and intermediate filaments[7]–[9]s. Also, they contribute to the overall cell elasticity, mechanical/ structural support, cell shape, mobility, and intracellular transport[6], [10]–[15].

In normal cells, actin polymerization/depolymerization, stimuli induced remodeling, transport vesicles, focal adhesions, cadherin adhesions, formation and elongation of actin-rich locomotion protrusions such as lamellipodia and filopodia, are all controlled by various proteins (binding proteins, capping/severing proteins, crosslinking/bundling proteins, stabilizing proteins, and signaling proteins)[7], [10]. Hence, any alteration in the typical functioning of cytoskeletal structure and its associated proteins results in abnormal cell behavior observed in various diseases such as cancer[4], [10], [12], [16]–[20].

Some reported cancer-induced abnormalities are disorganized crosslinked actin fiber networks with no defined striations and sparse actin distribution at the basal plane[8], [9], [21], [22]. These abnormalities deviate from the long, parallel, dense stress fibers distributed across the entire healthy cell. The mechanical integrity of cancer cells is also compromised as various studies report a decrease in the apparent Young’s modulus, stiffness, viscosity, cell-ECM adhesion, and cell-cell adhesion [8]–[10], [20], [23]–[28]. The crucial findings in these studies suggest a strong correlation between cell deformability and cell malignancy[22], [26], [37], [29]–[36].

Metastasis which is the cause of 90% of cancer deaths, has been linked to the disruption of the cell’s cytoskeletal function and a phenomenon called epithelial to mesenchymal transition [7], [38], [39]. During EMT, cancer cells acquire migratory abilities characteristic of mesenchymal phenotypes and travel to new sights where it transitions back to their epithelial form and proliferates [39]. In addition, remodeling of the typical cytokeratin-rich intermediate filament network to a vimentin-rich network has increased EMT effects and metastasis in all cancer types[7].

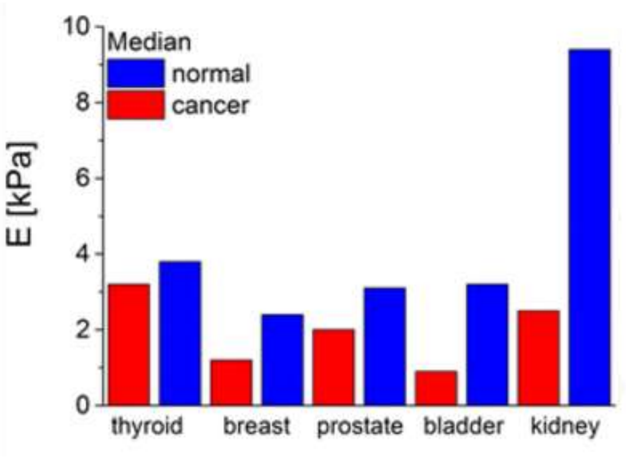

Fig. 2.2. Single-cell Young's modulus values for various cancer [29], [33]–[36], [40]

2.4. Mechanical Characterization of Cells

In recent years, a vast number of experimental techniques have been explored for the mechanical characterization of cells [6], [14], [46]–[48], [21], [22], [31], [41]–[45].

These can be grouped into three categories [11], namely:

1. Type A: The local probing of only a portion of a single cell.

2. Type B: Mechanically loading the entire single cell.

3. Type C: The simultaneous loading of a population of cells.

Type A and B measure single-cell deformation, while the Type C method measures shear flow over a group of cells [11].

2.4.1. Local Probing of a Portion of the Cell

As the name implies, only a part of the cell is probed for its mechanical properties. Examples of experimental techniques that utilize this principle are: (i) Atomic Force Microscopy (AFM); (ii) Instrumented depth-sensing indentation methods; and (iii) Magnetic twisting cytometry (MTC).

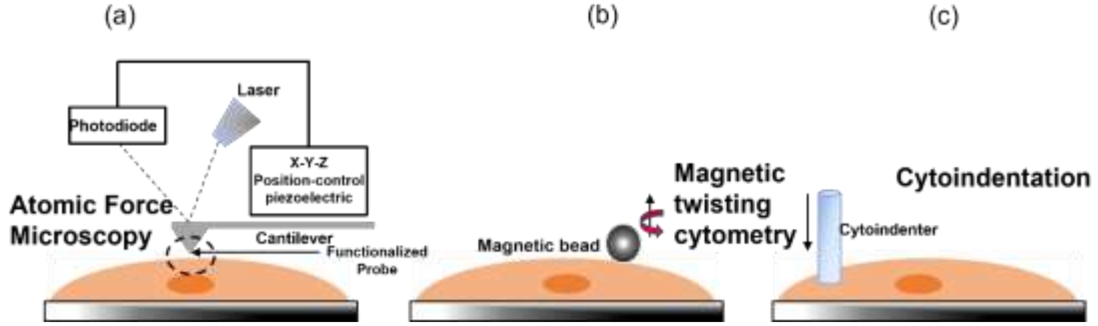

Fig. 2.3. Schematic showing the use of (a) Atomic force microscopy, (b) Magnetic twisting cytometry, and(c) Cytoindentation to probe a portion of the cell [49]

AFM probes the cell surface with a sharp tip attached to a flexible cantilever. It detects deflection using a photodiode [50]. MTC attaches magnetic beads to functionalized surfaces. The applied magnetic field causes a twisting moment in the cell, from which the elastic properties can be deduced [13]. The forces used usually range from 10^{-2} to $10^{-6} N$ while the displacements are typically less than 1nm [11].

2.4.2.Mechanically loading the entire cell

The entire cell is mechanically loaded to extract its mechanical properties by measuring the forces and displacements applied to the cell geometry. Examples of experimental techniques that utilize this approach include (i) Micropipette Aspiration (MA), (ii) Optical Tweezers (OT), (iii) Microplate Stretchers (MS) [11], and (iv) Shear Assay (SA)[26], [30], [31].

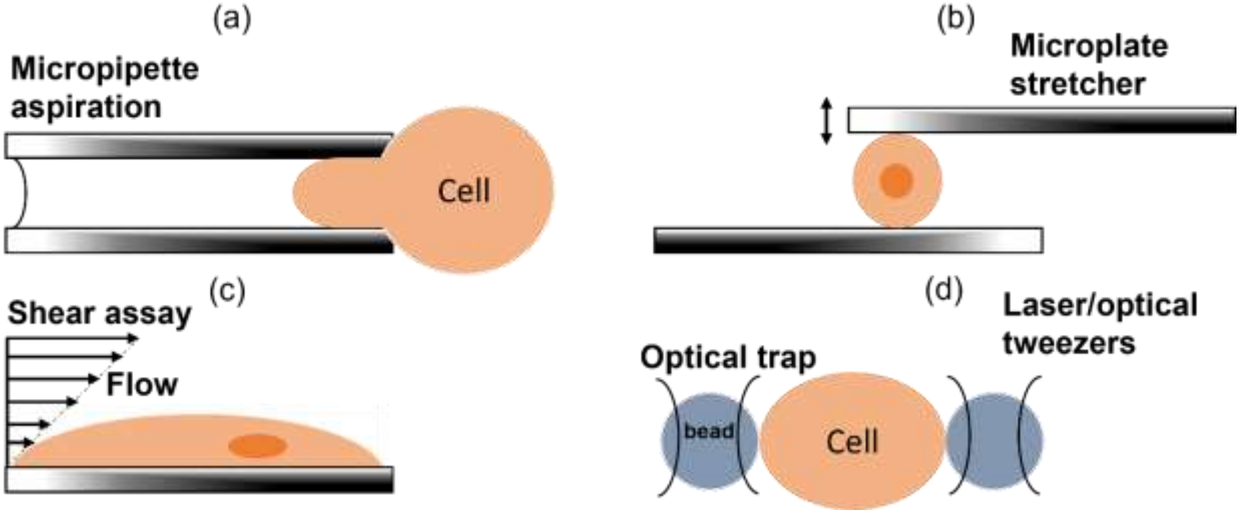

Fig. 2.4. Schematic showing the use of (a) Micropipette aspirator, (b) Microplate stretcher, (c) Shear Assay, and (d) Laser/optical tweezers[49] to probe the entire cell.

Here forces applied range from 10^{-12} to 10^{-7} N and measures displacements that are less than a micrometer[49]. OT works like a laser trap, and attractive forces are set up between the laser beam and two beads placed on opposite sides of the cell or between one bead and a glass side on opposite sides of the cell. In both cases, the cell boundaries are displaced and measured [51], [52]. In the microplate stretcher, shear deformation is induced on the cell by two functionalized glass plates attached to the cell surface [49]. MA works by aspirating a portion of a cell or the whole-cell through a micropipette, and changes in geometry provide the mechanical response of the cell [41]. The SA system measures the interfacial shear strength of single cells. This interfacial shear strength results from a laminar flow of a viscous fluid through a parallel plate flow chamber and an in-situ optical microscope observation of individual cells being deformed by shear flow [22], [26], [30], [31].

2.4.3. Loading of a population of cells

In this loading style, the deformation characteristics of the substrate and the adhesive forces between the cells and substrates are measured by monitoring the shear resistance of cells to fluid flow using a parallel plate flow chamber or a cone and plate viscometer [49][11]. In addition**,** microfluidic and nanofluidic devices are also used to simulate the flow of cells through blood vessels [49] and offer new opportunities to control the concentration of molecules and cells in space and time [53]. Examples include induced sickling and vassocclusion of erythrocytes [54] and the complex behavior of uninfected red blood cells and red blood cells infected with plasmodium falciparum [55].

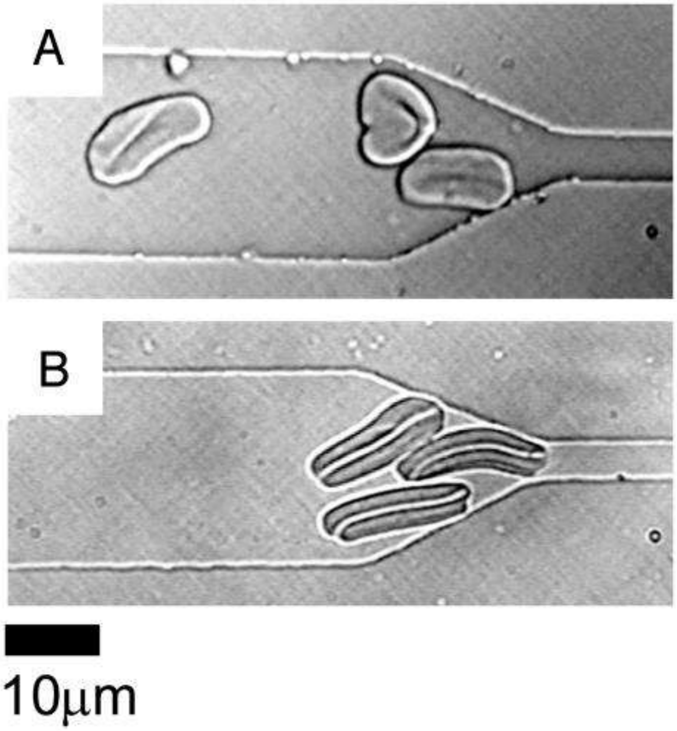

Fig. 2.5. Shows differences in recovery of compressed infected cells. (A) Early trophozoite stages of infected RBCs were partially distorted after passage through a 4-μm constriction and remained compressed for ≈30 sec after emerging from the channels. (B) Schizont forms of RBC infections were more severely deformed and did not relax back to their original shape after passage through a 4-μm constriction even 1–2 min after compression[55].

2.4.4. Measurement of Cell Adhesion

Measurements of the adhesion of nanoparticles to diseased/normal cells can provide valuable insights for the design of functionalized nanoparticles for the targeting, detection, and killing of diseased cells [56]–[58]. For example, the measured adhesive forces between GNP-Antibody conjugates and cancer cells have been four to five times greater than those of normal cells [57] and suggest that nanoparticles may be used to target cancer cells[57].

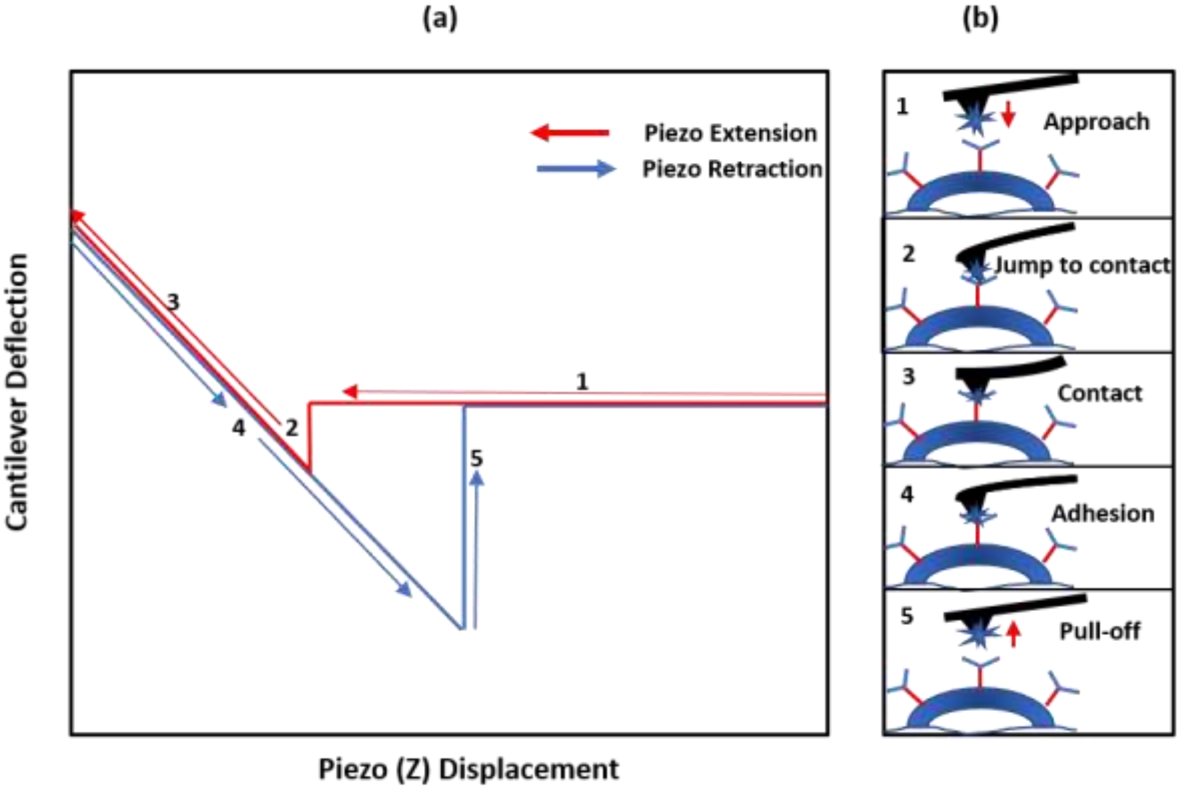

Fig. 2.6. (a) One cycle Deflection–displacement plot with corresponding stages of force-displacement behavior (b) In one approach-retract cycle, the AFM tip approaches the sample surface (1), jumps to contact (2), Indents surface (3), adheres to surface (4), detaches, but requires more force to pull off adhered AFM tip from the substrate(5)[59].

Fig.2.6. presents a schematic of a typical AFM force-displacement plot with the corresponding stages of force-displacement behavior. Initially, the AFM tip approaches the sample's surface (1). It then jumps into contact with the surface when significant adhesive interactions occur (often due

to secondary bonds) that become significant as the cell membrane and receptors on the membrane are approached at point (2). Upon contact with the receptor/cell membrane, elastic bending of the membrane occurs along (3). The retraction of tip (4) is then continued until the tip is pulled-off at (5). The pull-off does not occur when force is zero because of adhesive interactions. In addition, the force plots obtained provide insights into adhesion forces, weak links, and potential failure sites. Finally, laser beams detect the deflection of cantilevers and track changes in deflection with position-sensitive photodiodes (PSPD).

2.5. Mechanical Biomarkers

Cancer diagnosis requires precise imaging tools for screening tissue and biopsy to distinguish between benign and malignant tissue [60]. Mammography is the most used screening method for breast cancer detection but is less effective for subjects less than 40 years old due to the denser nature of the breast tissue [61]. Mammography can also not track cancer progression or therapeutic effects on the tumor and is less sensitive to tumor sizes less than 1mm; thus, early detection of breast cancer is limited [60].

Molecular biomarker-based biopsy methods are commonly used due to their relative sensitivity and selectivity[60]. In addition, techniques such as radioimmunoassay, immunohistochemistry, enzyme-linked immunosorbent assay (ELISA), and fluoroimmunoassay have been used in the biopsy process[60]. However, these methods involve complex labeling techniques that are time-consuming, expensive, and require skilled personnel[62]. Thus, there is an urgent need to develop highly sensitive, selective, and label-free methods for rapid cancer diagnosis.

2.5.1. Adhesion

In search of alternative biomarkers for cancer, pull-off adhesion forces between ligand functionalized AFM tips and cancer cells with overexpressed receptors have gained much interest. Specifically, measurements of adhesive forces between AFM probes coated with gold nanoparticle-antibody conjugates and breast cancer cells have been reported to be four to five times greater than normal breast cells [57]. Similarly, other AFM adhesion studies on TNBC report a three to six-fold increase in the adhesion of ligand functionalized AFM tips to breast cancer cells compared to the non-tumorigenic breast cells[56], [58], [63], [64].

Quite notably, these adhesion studies on cancerous and non-tumorigenic cells provide valuable insights into the design of effective functionalized nanoparticles for theranostic cancer treatment[56]–[58], [63], [64]. In addition, these results suggest that adhesion force measurements with AFM may be used as biomarkers for diagnosis and prognostic purposes in targeted cancer therapeutics[56]–[58], [63], [64]. However, it is essential to note that reported AFM adhesion forces between single cancer cells, and multiple ligands are typically in the nN range[56]–[58], [63], [64]. In contrast, single-molecule ligand-receptor interactions typically have unbinding forces in the pN range[65]–[70].

2.5.2. Viscoelasticity

The cell is a viscoelastic material with a dynamic cytoskeletal protein network that regulates the overall functioning and shape of the cell[5]. Changes in the structure and distribution of these cytoskeletal structures lead to changes in the mechanical properties of single cells[7], [10], [16], [17], [19], [27], [39], [71], [72]. Furthermore, these changes in cell cytoskeletal structures are linked to disease progression and aging in cells[44], [72][7], [10], [16], [17], [19], [27], [39], [71],

[72]. Hence, the mechanical properties of cancer cells have gained much attention as biomarkers for cancer detection[8], [10], [19]–[21], [32], [44], [71], [73], [74]. Generally, cancer cells are found to be more deformable than their corresponding non-tumorigenic cells[8], [17], [20], [21], [32], [75]. In addition, the reduced cancer cell stiffness is due to the actin cytoskeletal remodeling that enhances the ability of such cells to escape the primary tumor[10], [17], [21].

2.6. Nanoparticle Uptake

Receptor-ligand interactions are one of the entry pathways for biological cells to internalize food, viruses, and nanoparticles [76]–[78]. Therefore, most targeted nanoparticles have been designed to mimic viruses, which have surface proteins that can interact with specific receptors that are overexpressed on the surfaces of the biological cell membrane [78]–[80].

.

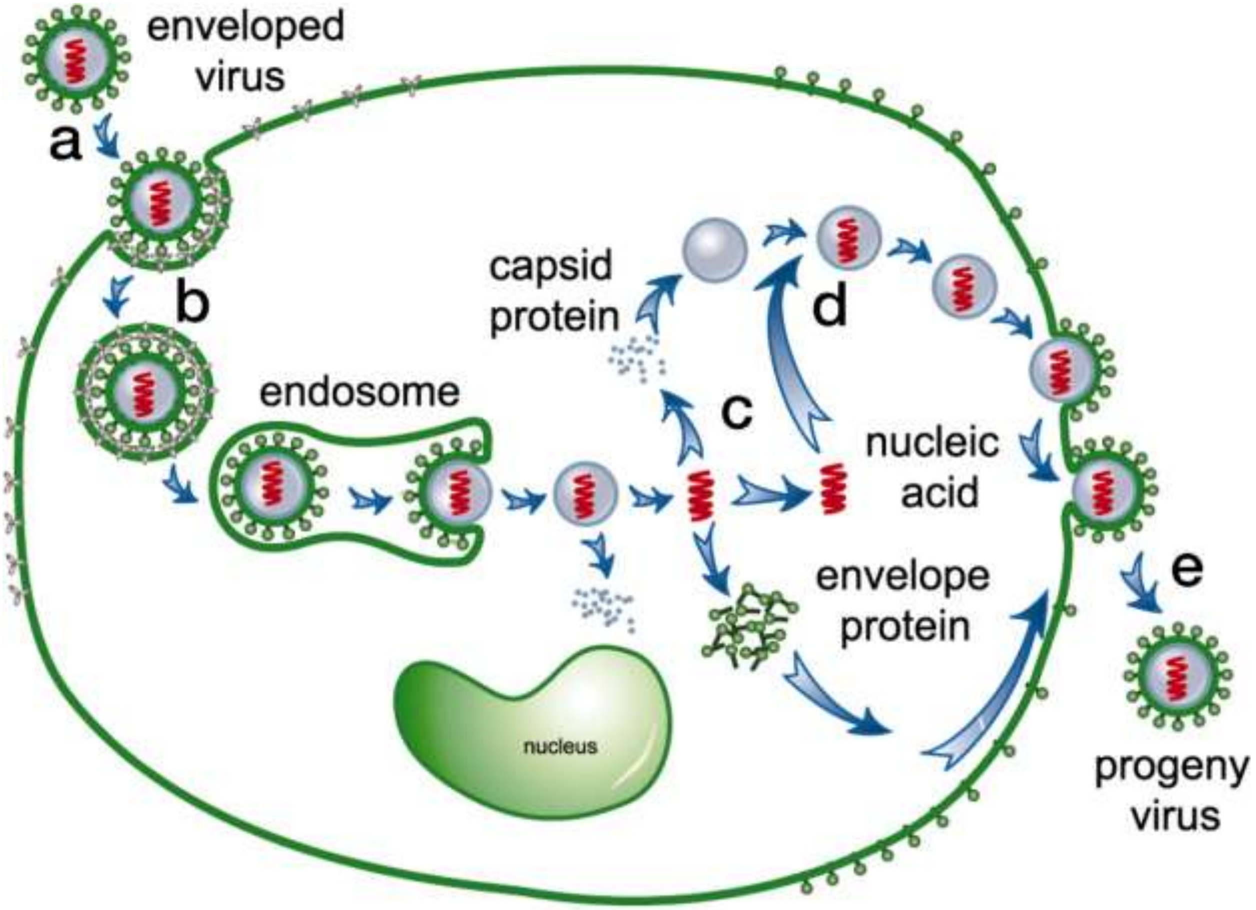

Fig. 2.7. The life cycle of an animal virus. (a) Adsorption or docking with the host receptor protein. (b) Entry into the host cytoplasm. (c) Biosynthesis of viral components. (d) Assembly of viral components into complete viral units. (e) Budding from the host cell[77].

Various theoretical, computational, and experimental studies on targeted nanoparticle and drug delivery systems identify particle size, ligand density, and receptor density as limiting factors to the efficient uptake of these nanostructures[77], [81]–[89]

In particular, nanoparticle sizes designed for in-vitro application typically range from 10-300nm[79], [89]. Interestingly, nanoparticles with diameters less than 10 nm were observed to cluster at the cell membrane before being engulfed by the cells. In contrast, larger particles greater than 100 nm were directly internalized without clustering at the different cell membranes [87]. Furthermore, results from in-vitro uptake of gold nanoparticles show that the nucleus of HEp-2 cells internalized nanoparticles of 3 to 10 nm in diameter after 1hr of incubation as opposed to the accumulation of nanoparticles sized 25 to 50 nm in the cytoplasm [90].

It is important to note that surface charge also affects nanoparticle uptake. In particular, lower endocytosis rates have been shown for anionic nanoparticles than cationic nanoparticles [87][91]. This surface charge effect occurs due to the long-range columbic repulsion between the negatively charged cell surface and charged nanoparticles[77], [91], [92]. For instance, positively charged nanoparticles favor the non-specific binding to cell receptors and plasma proteins[77], [91], [92]. However, this non-specific binding is not desirable for targeted cancer applications as it triggers reticuloendothelial sequestration[91]. In addition, if the overall energy balance decreases the Gibbs free energy, the membrane will wrap around the nanoparticle in a vesicle-like structure, which then buds off and fuses with other vesicles to form endosomes [77].

Earlier models for virus budding on a host cell membrane focused on a single nanoparticle size [82], [93], [94]. In contrast, recent models extended those studies using front tracking diffusion models to estimate nanoparticle wrapping time for varying nanoparticle sizes [77], [79], modeled effects of the energy barrier between nanoparticles when in a fully wrapped and partially wrapped state[81] and predicted the binding of receptors relative to a fixed ligand density on nanoparticle surfaces for a range of nanoparticle sizes[79], [85], [89], [95], [96] These models assume uptake of single-particle entry or discrete multiple-particle entry at various positions on the cell membrane. Despite experimental evidence [87], [97], [98], which shows that nanoparticle clusters can also be internalized by the biological cell membrane, the cluster effect on free energy associated with nanoparticle uptake remains unresolved for many nanoparticle systems developed for cancer therapeutic applications

Presently, some studies explored modified thermodynamic-kinetic models that include surface energy effects on the free energy function associated with nanoparticle wrapping[97], [99]. Specifically, reports on the influence of receptor density, ligand density, and surface energy on the wrapping time and uptake efficiency of Luteinizing Hormone Releasing Hormone (LHRH) conjugated superparamagnetic iron oxide nanoparticles (SPION) in human breast cancer Hs 578T [97] were elucidated. Similarly, the surface energy effects, amongst others, were explored using LHRH conjugated Magnetite nanoparticles in non-tumorigenic breast cells(MCF 10A) and tumorigenic TNBC (MDA-MB-231)[100].

2.7. Cancer Treatment by Bulk Systemic Chemotherapy

Chemotherapy is one of the standard systemic therapies for cancer treatment[101]–[103]. Currently, cytotoxic chemotherapy agents induce cell death by disrupting single/multiple cell cycle processes and essential proteins and DNA[101], [104].

In general, pathological complete response (pCR) in cancer patients is mainly achieved when chemotherapy is combined with surgery, either as adjuvant or neoadjuvant treatment[105]. Although, significantly, the addition of platinum compounds to standard chemotherapy has doubled the portion of TNBC patients achieving pCR [104], [106], patients who do not acquire pCR exhibit worse outcomes than patients with residual diseases from other subtypes of breast cancer [104], [107]. In addition, the treatment of metastatic TNBC with chemotherapy is often incurable and is mostly palliative[108], [109]. In addition, chemotherapy is often associated with numerous side effects due to its immunosuppressant characteristics[101], [110], [111]. However, these side effects vary per patient and generally occur due to the cytotoxic impacts on normal dividing cells and often result in nausea, hair loss, and acute cholinergic gastrointestinal problems[101], [110], [111]. Notably, 90% of chemotherapeutic treatment failure is caused by multidrug resistance [110], [111]. Mainly, drug resistance could occur by insufficient drug delivery to tumors because of poor blood supply, decreased drug uptake due to changes in protein structure responsible for drug transport, increase in drug efflux, mutations in b-tubulin that interfere with tubulin stabilization, and an increase in DNA repair associated with platinum resistance[101], [110], [111]. These challenges drive research into identifying an effective therapeutic strategy for TNBC[101], [105], [109], [112]–[115].

2.7.1. Targeted Cancer Drugs

Until recently, the standard treatment for TNBC has been chemotherapy. Although neo-adjuvant(NA) systemic chemotherapy with platinum compounds seems to optimize the pCR of patients with early-stage TNBC[105], [108], patients with residual TNBC have a greater risk of relapse than other breast cancer subtypes. In addition, patients with metastatic TNBC still exhibit poor prognosis and have a median overall survival (OS) of 18 months [104], [107], [109].

Therefore, improved biomarkers are needed to inform better patient selection and treatment. Particularly, molecular and gene expression profiling studies have identified possible target pathways and molecules that are expressed in cancer cells and within the tumor microenvironment[103], [108], [120]–[127], [109], [113]–[119]

Remarkably, Poly (ADP-ribose) Polymerase (PARP) inhibitors have been used to target tumors with BRCA 1 and BRCA 2 mutations[103] and have been identified as a potential target for treating metastatic TNBC that overexpress program cell death ligand 1 (PD-L1) [108]. This interest in PARP is due to PARP's vital role in several cellular processes such as DNA repair, genomic stability, and programmed cell death [103].

Also, the receptor tyrosine kinases (RTK) family has gained much interest [103], [109], [114], [115], [118], [119] because RTKs are transmembrane proteins that help intercellular interaction, cell proliferation, differentiation, metabolism and are reported to be overexpressed in most cancers, including TNBC[103], [108], [113]–[115], [117]. A few RTKs researched include epidermal growth factor receptors (EGFRs), fibroblast growth factors receptor (FGFR), TGF-β (receptor), platelet-derived growth factor receptor (PDGFR), and vascular endothelial growth factor (VEGFR). However, although preclinical models validate these RTK targets in cell lines, none of them are suitable as single-agent targets to curb the aggressiveness of TNBC, as observed in clinical trials[103].

Another unique approach to targeted TNBC therapy is the inhibition of mitogen-activated protein kinases/extracellular signal-regulated kinases (MAPK/ERK) pathway using the mammalian target of rapamycin (mTOR), phosphoinositide 3-kinases (PI3K), and protein kinase B (PKB or AKT) molecules, to alter cell proliferative and survival mechanisms[103], [109], [114], [115], [118]–[121]. PI3K inhibition with chemotherapy saw a significant improvement in pCR in metastatic TNBC in recent clinical phase 1 trials[122]. Furthermore, in-vitro suppression of PI3K increased tumor sensitivity to PARP inhibition [128]; nevertheless, more clinical trial studies are still needed[103].

Interestingly, the cell cycle and DNA damage repair checkpoints in TNBC through Cyclin-dependent Kinase (CDK1/2/4/6) and Checkpoint kinases (CHK1/2) are considered for targeted therapeutics [103]. Specifically, targeting DNA damage-induced cell cycle arrest to interfere with cell cycle control has the potential to cause inappropriate cell cycle progression resulting in DNA damage accumulation and cancer cell death[103], [123]–[126]. In addition, disrupting cell cycle arrest weakens cancer cell survival mechanism and prevents DNA repair, activating various apoptotic processes[103]. However, although CHK1/2 is not overexpressed or mutated in TNBC, CHK1/2 inhibition in aggressive breast tumors with Tumor protein 53 (TP53) mutation such as TNBC helps to arrest their cell cycle by increasing sensitivity to chemotherapeutic drugs[103], [127].

It is commonly known amongst breast cancer researchers that TBNC is not highly immunogenic[103], [118]. However, about 20% of TNBC cells express a mutated BRCA1 gene that increases their sensitivity to PD-L1 immunotherapy inhibitors [103], [118]. Therefore, the overexpression of PD-L1 receptors and tumor-infiltrating lymphocytes (TILs) are proposed as prognostic markers for TNBC[103], [108]. In addition, gene expression/profiling and immunohistochemistry studies suggest that increased TIL's are associated with better prognosis[103], [108], [119], [129]–[131]. However, the major limitation of immunotherapy for TBNC treatment is the lack of models for human TNBC cells because patient-derived xenografts do not trigger the same immunomodulatory responses that activate anti-tumor immunity[103], [132].

Currently, antibody-drug conjugates (ADCs) are part of the ligand-drug conjugates generating much excitement and may allow re-examining of prior cytotoxic agents that failed in development due to toxicity[119]. In particular, ADCs are novel drug conjugates that permit the targeted delivery of cytotoxic drugs to cancer cells through the specific binding of an antibody to a selective cancer cell surface molecule. Over time, ADCs have transitioned into clinical studies for many cancer types, including TNBC[119]. However, although antibodies possess many desirable technical attributes[119], [133]–[136] they are often associated with immunogenicity and promote non-specific binding[137][138].

Notably, other ligands such as aptamers, proteins, DARpins, transferrin, small molecules(folates and mannose derivatives), and peptides [133], [134], [139] are explored for targeted TNBC. However, although each ligand has its merits and demerits[134], [137]–[142], peptides are advantageous because of their small size, low molecular weight, and cell-penetrating ability[133], [143]. Furthermore, peptides can be chemically synthesized at a large scale relatively inexpensively [133]. Some peptides such as RGD have binding affinities (K_D) comparable to some antibodies (3.2 to 100nM)[144], [145]. Quite notably, Luteinizing Hormone Releasing Hormone(LHRH) and its peptide analogs or are characterized by high binding affinity to LHRH receptors (K_D in nM range) and possess the ability to recognize a broad variety of tumors including TNBC but not normal cells[138], [146]–[151]. These LHRH/Triptorelin ligands are proposed as theranostic agents delivering them directly to cancer cells with overexpression of LHRH receptors[57], [58], [155], [63], [64], [97], [99], [138], [152]–[154].

Recently, the FDA has approved three targeted therapies for TNBC, including the PARP inhibitors olaparib and talazoparib for germline BRCA mutation-associated breast cancer (gBRCAm-BC) and most recently, the checkpoint inhibitor atezolizumab in combination with nab-paclitaxel for programmed death-ligand 1 (PD-L1+) and advanced TNBC[119]. However, the use of PARP, MAPK/ERK, DNA damage response (DDR), CHEK1/2, CDK1/2/4/6 pathways, and PD-L1 receptors as standalone therapies for TNBC fails to elicit the desired pCR outcome in clinical trials, mainly due to intrinsic resistance (drugs with proven efficacy in preclinical studies fails to produce any detectable response upon initial treatment) and acquired drug resistance (tumor cells that were initially sensitive to targeted inhibitors stop responding despite continued administration of the drug)[103], [156]–[158] Nevertheless, combination therapies may be promising[103], [159]–[161]. Interestingly, multidrug conjugates have been explored to overcome the challenges of tumor heterogeneity and drug resistance[162].

It is essential to note that sources of resistance in targeted cancer treatment involve signaling pathway redundancies and reprogramming the kinome, effectively bypassing targeted inhibition[103], [159]. Other sources of acquired resistance might involve intratumoral heterogeneity of TNBC that allows a specific population of tumor cells (often stem cell-like) to be enriched and contribute to tumor recurrence and resistance after treatments, as shown in xenograft studies. In addition, acquired resistance also impacts the duration of the response rate[103], [159]. Although most targeted resistance mechanisms are not entirely understood, studies suggest implementing time staggered and sequential treatment to prevent rewiring of molecular pathways and overcome drug resistance to targeted chemotherapy[103], [159]–[161]. In the future, the determination of appropriate targeted drug combinations for TNBC treatment and their estimated toxicity (therapeutic Index) on non-tumorigenic cells will be valuable.

2.7.2. Localized Cancer Drug Delivery Systems

Many chemotherapeutic drugs exhibit low solubility in aqueous solutions; hence, drug delivery through intravenous channels is complicated without chemical modification or adding a surfactant-containing solution to the chemotherapy drugs[163]. These approaches to improving cancer drugs' aqueous solubility often result in low bioavailability, sensitization reactions, and the inability to achieve therapeutic levels of drug within or adjacent to the tumor[164], [165]. Furthermore, untargeted intravenous drug delivery leads to toxic levels of drug accumulation in healthy tissue, resulting in numerous side effects which limit the drug dose [166]. Unfortunately, less than 0.5% of intravenous injected paclitaxel drug dose is locally available for cancer treatment; much of it is eliminated from the body[163], [167]. Localized chemotherapy intends to enhance treatment efficacy at the tumor site and improve OS. Specifically, drug-loaded implants administered directly to the tumor site are reported to stabilize embedded drug molecules, preserve anti-cancer activity, and sustain controlled drug release of the cytotoxic drug[163], [168]–[174].

In addition, localized drug delivery results in less drug waste and diminished side effects due to the avoidance of systemic circulation of chemotherapeutic drugs[168]–[172][163][173][174].

Localized drug delivery systems can be grouped into two based on their delivery mechanism. The first relies on intravenous systemic delivery and consists of both natural and synthetic polymer nanoparticles, liposomes, and dendrimers[175]–[178][179][163]. These drug delivery systems localize in cancer tumors by passive diffusion and enhanced permeation and retention (EPR) of the leaky tumor vasculature [170], [178], [180]–[182] or by actively targeting over-expressed receptor or protein markers on the surfaces of tumor cells via ligand/protein bioconjugation[163], [183]–[186]. Also, localized drug depots could be environment-responsive and drug release triggered by an environmental stimulus[163], [179]. Notably, polyethylene glycol (PEG) coating reduces nanoparticle sequestration by the reticuloendothelial system to combat reported issues of short circulation time[187]–[190].

Subsequently, the second group of drug delivery systems is designed for implant within or adjacent to cancerous tumors. Advantageously, these implantable systems have predictable, sustained, and controlled drug release kinetics. In addition, most of these drug delivery devices are biodegradable, which eliminates the need for device removal surgery [163], [179], [191], [192]. Examples of such drug release depot systems include; drug-eluting films, gels, wafers, milli rods, transdermal patches, microneedles, and microparticles [163], [179], [186], [193]–[199].

2.7.3. Localized Heat Delivery Systems for Hyperthermia and Tissue Ablation

The clinical use of heat for cancer therapeutics has received significant attention due to its minimal side effects, flexible treatment regime, and potential to enhance the therapeutic efficacy of conventional cancer therapies[200]–[204].

Notably, high-temperature doses (50-100ºC) on tumor cells cause necrosis, while hyperthermia temperature doses(40-45 ºC) have been reported to induce apoptosis in tumor cells[200], [203], [205]–[209]. In addition, sublethal temperature doses have been found to sensitize cancer cells to radiation and chemotherapeutic drugs[200], [201], [204].

Whole-body (WB) or regional radiotherapy (RT) often serves as an adjuvant treatment to eliminate residual tumors and reoccurrence after surgery. However, issues related to treatment schedules of WBRT impose a lot of stress on patients due to a lack of preferential and localized heating[200], [201]. Significant efforts have been made to localize heating in tumor cells by the insertion of a susceptor material that generates heat by applied electromagnetic field[201], [210]–[212]. In addition, localized heat can be generated via molecular oscillations of tissue material by ultrasonic pressure waves or by interstitial hyperthermia devices such as radiofrequency (RF) electrode needles, microwave antennas, and inductively heated ferromagnetic implants[201], [210]–[212]. However, issues of biocompatibility and corrosion plague these methods and detract from their long-term use[201], [213], [214]. Furthermore, inductively heated ferromagnetic implants require a high density of thermoseeds [215] and radiofrequency/microwave treatment suffers from energy deposition in intervening tissues when the energy source is also the heat source or the heat from the susceptor substance damages normal tissue.

Interestingly, polymeric composite materials with polymer matrices and plasmonic or ferromagnetic nanomaterials are being explored to develop implantable biomedical devices that mitigate biocompatibility/corrosion issues common with metallic implants [201], [212], [216]. Furthermore, these polymeric composite devices are especially promising for targeted/localized heating when exposed to a laser source or alternating magnetic field[201], [212], [216].

2.8. References

[1] R. A. Weinberg, “Fundamental Understandings,” Sci. Am., vol. 275, no. 3, pp. 61–61, 1996.

[2] D. Hanahan and R. A. Weinberg, “Hallmarks of cancer: The next generation,” Cell, vol. 144, no. 5, pp. 646–674, 2011.

[3] National Institutes of Health (US)., “Understanding Cancer, Biological Sciences Curriculum Study. NIH Curriculum Supplement Series [Internet],” National Institutes of Health (US), 2007. [Online]. Available: www.ncbi.nlm.nih.gov/books/NBK20362/.

[4] S. Suresh et al., “Reprint of: Connections between single-cell biomechanics and human disease states: Gastrointestinal cancer and malaria,” Acta Biomater., vol. 23, no. S, pp. S3–S15, 2015.

[5] K. E. Kasza et al., “The cell as a material,” Curr. Opin. Cell Biol., vol. 19, no. 1, pp. 101–107, 2007.

[6] K. Haase, A. E. Pelling, and K. Haase, “Investigating cell mechanics with atomic force microscopy Author for correspondence :,” no. March 2015, 2016.

[7] J. Aseervatham, “Cytoskeletal remodeling in cancer,” Biology, vol. 9, no. 11. pp. 1–40, 2020.

[8] Q. S. Li, G. Y. H. Lee, C. N. Ong, and C. T. Lim, “AFM indentation study of breast cancer cells,” Biochem. Biophys. Res. Commun., vol. 374, no. 4, pp. 609–613, 2008.

[9] A. N. Ketene, E. M. Schmelz, P. C. Roberts, and M. Agah, “The effects of cancer progression on the viscoelasticity of ovarian cell cytoskeleton structures,” Nanomedicine Nanotechnology, Biol. Med., vol. 8, no. 1, pp. 93–102, 2012.

[10] W. Xu, R. Mezencev, B. Kim, L. Wang, J. McDonald, and T. Sulchek, “Cell Stiffness Is a Biomarker of the Metastatic Potential of Ovarian Cancer Cells,” PLoS One, vol. 7, no. 10, 2012.

[11] G. Bao and S. Suresh, “Cell and molecular mechanics of biological materials,” Nat. Mater., vol. 2, pp. 715–725, 2003.

[12] S. Suresh, “Cancer Biomechanics,” Mater. Sci., vol. 3, no. 4, pp. 413–438, 2010.

[13] M. L. Rodriguez, P. J. McGarry, and N. J. Sniadecki, “Review on Cell Mechanics: Experimental and Modeling Approaches,” Appl. Mech. Rev., vol. 65, no. 6, p. 60801, 2013.

[14] G. Thomas, N. A. Burnham, T. A. Camesano, and Q. Wen, “Measuring the Mechanical Properties of Living Cells Using Atomic Force Microscopy,” J. Vis. Exp., 2013.

[15] M. E. Grady, R. J. Composto, and D. M. Eckmann, “Cell elasticity with altered cytoskeletal architectures across multiple cell types,” J. Mech. Behav. Biomed. Mater., vol. 61, pp. 197–207, 2016.

[16] M. N. Starodubtseva, “Mechanical properties of cells and ageing,” Ageing Res. Rev., vol. 10, no. 1, pp. 16–25, 2011.

[17] N. Schierbaum, J. Rheinlaender, and T. E. Schäffer, “Viscoelastic properties of normal and cancerous human breast cells are affected differently by contact to adjacent cells,” Acta Biomater., vol. 55, pp. 239–248, 2017.

[18] Y. Xie, M. Wang, M. Cheng, Z. Gao, and G. Wang, “The viscoelastic behaviors of several kinds of cancer cells and normal cells,” J. Mech. Behav. Biomed. Mater., vol. 91, no. February 2018, pp. 54–58, 2019.

[19] M. Pachenari, S. M. Seyedpour, M. Janmaleki, S. B. Shayan, S. Taranejoo, and H. Hosseinkhani, “Mechanical properties of cancer cytoskeleton depend on actin filaments to microtubules content: Investigating different grades of colon cancer cell lines,” J. Biomech., vol. 47, no. 2, pp. 373–379, 2014.

[20] K. Hayashi and M. Iwata, “Stiffness of cancer cells measured with an AFM indentation method,” J. Mech. Behav. Biomed. Mater., vol. 49, pp. 105–111, 2015.

[21] J. Hu, Y. Zhou, J. D. Obayemi, J. Du, and W. O. Soboyejo, “An investigation of the viscoelastic properties and the actin cytoskeletal structure of triple negative breast cancer cells,” J. Mech. Behav. Biomed. Mater., vol. 86, no. May, pp. 1–13, 2018.

[22] G. Fu et al., “Shear assay measurements of cell adhesion on biomaterials surfaces,” Mater. Sci. Eng. C, 2009.

[23] M. J. Paszek et al., “Tensional homeostasis and the malignant phenotype,” Cancer Cell, vol. 8, no. 3, pp. 241–254, 2005.

[24] S. Huang and D. E. Ingber, “Cell tension, matrix mechanics, and cancer development,” Cancer Cell, vol. 8, no. 3. pp. 175–176, 2005.

[25] R. W. Ruddon, Cancer biology, 3rd ed. 1995.

[26] C. J. Ani et al., “A shear assay study of single normal/breast cancer cell deformation and detachment from poly-di-methyl-siloxane (PDMS) surfaces,” J. Mech. Behav. Biomed. Mater., vol. 91, 2019.

[27] L. Li, W. Zhang, and J. Wang, “A viscoelastic – stochastic model of the effects of cytoskeleton remodelling on cell adhesion Subject Category : Subject Areas : Author for correspondence :,” R. Soc. Open Sci., vol. 3, p. 160539, 2016.

[28] J. Hu, Y. Zhou, J. D. Obayemi, J. Du, and W. O. Soboyejo, “An investigation of the viscoelastic properties and the actin cytoskeletal structure of triple negative breast cancer cells,” J. Mech. Behav. Biomed. Mater., vol. 86, no. January, pp. 1–13, 2018.

[29] M. Prabhune, G. Belge, A. Dotzauer, J. Bullerdiek, and M. Radmacher, “Comparison of mechanical properties of normal and malignant thyroid cells,” Micron, vol. 43, no. 12, pp. 1267–1272, 2012.

[30] J. Hu, Y. Zhou, J. D. Obayemi, J. Du, and W. O. Soboyejo, “An investigation of the viscoelastic properties and the actin cytoskeletal structure of triple negative breast cancer cells,” J. Mech. Behav. Biomed. Mater., 2018.

[31] Y. Cao, R. Bly, W. Moore, Z. Gao, A. M. Cuitino, and W. Soboyejo, “On the measurement of human osteosarcoma cell elastic modulus using shear assay experiments,” J. Mater. Sci. Mater. Med., vol. 18, no. 1, pp. 103–109, 2007.

[32] K. Onwudiwe et al., “Actin cytoskeletal structure and the statistical variations of the mechanical properties of non-tumorigenic breast and triple-negative breast cancer cells,” J. Mech. Behav. Biomed. Mater., vol. 119, p. 104505, Jul. 2021.

[33] L. M. Rebelo, J. S. de Sousa, J. Mendes Filho, and M. Radmacher, “Comparison of the viscoelastic properties of cells from different kidney cancer phenotypes measured with atomic force microscopy.,” Nanotechnology, vol. 24, p. 055102, 2013.

[34] M. Lekka, P. Laidler, D. Gil, J. Lekki, Z. Stachura, and a Z. Hrynkiewicz, “Elasticity of normal and cancerous human bladder cells studied by scanning force microscopy.,” Eur. Biophys. J., vol. 28, no. 4, pp. 312–316, 1999.

[35] E. C. Faria et al., “Measurement of elastic properties of prostate cancer cells using AFM.,” Analyst, vol. 133, no. 11, pp. 1498–1500, 2008.

[36] G. Coceano et al., “Investigation into local cell mechanics by atomic force microscopy mapping and optical tweezer vertical indentation,” Nanotechnology, vol. 27, no. 6, p. 65102, 2016.

[37] T. Korb et al., “Integrity of actin fibers and microtubules influences metastatic tumor cell adhesion,” Exp. Cell Res., vol. 299, no. 1, pp. 236–247, 2004.

[38] T. Ochalek, F. J. Nordt, K. Tullberg, and M. M. Burger, “Correlation between Cell Deformability and Metastatic Potential in B16-F1 Melanoma Cell Variants,” Cancer Res., vol. 48, no. 18, pp. 5124–5128, 1988.

[39] M. Izdebska, W. Zielinska, D. Grzanka, and M. Gagat, “The Role of Actin Dynamics and Actin-Binding Proteins Expression in Epithelial-to-Mesenchymal Transition and Its Association with Cancer Progression and Evaluation of Possible Therapeutic Targets,” 2018.

[40] M. Lekka, “Discrimination Between Normal and Cancerous Cells Using AFM,” Bionanoscience, vol. 6, no. 1, pp. 65–80, 2016.

[41] R. M. Hochmuth, “Micropipette aspiration of living cells,” J. Biomech., vol. 33, no. 1, pp. 15–22, 2000.

[42] K. J. Van Vliet, G. Bao, and S. Suresh, “The biomechanics toolbox : experimental approaches for living cells and biomolecules ఙ,” Acta Biomater., vol. 51, pp. 5881–5905, 2003.

[43] H. Zhang and K. K. Liu, “Optical tweezers for single cells,” J. R. Soc. Interface, vol. 5, no. 24, pp. 671–690, 2008.

[44] L. Li et al., “The biomechanics toolbox : experimental approaches for living cells and biomolecules,” J. Mech. Behav. Biomed. Mater., vol. 33, no. 1, pp. 371–388, 2003.

[45] R. Wang, H. Ding, M. Mir, K. Tangella, and G. Popescu, “Effective 3D viscoelasticity of red blood cells measured by diffraction phase microscopy,” vol. 2, no. 3, pp. 485–490, 2011.

[46] G. Massiera, K. M. Van Citters, P. L. Biancaniello, and J. C. Crocker, “Mechanics of single cells: Rheology, time dependence, and fluctuations,” Biophys. J., vol. 93, no. 10, pp. 3703–3713, 2007.

[47] J. P. Mills, L. Qie, M. Dao, C. T. Lim, and S. Suresh, “Nonlinear elastic and viscoelastic deformation of the human red blood cell with optical tweezers.,” Mechanics & chemistry of biosystems : MCB, vol. 1, no. 3. pp. 169–180, 2004.

[48] G. Bao and S. Suresh, “Cell and molecular mechanics of biological materials.,” Nat. Mater., vol. 2, no. 11, pp. 715–725, 2003.

[49] S. Suresh, “Biomechanics and biophysics of cancer cells,” Acta Mater., vol. 55, no. 12, pp. 3989–4014, 2007.

[50] Bruker, “The AFM Probe - Fundamentals , Selection , and Applications Introduction.”

[51] M. Dao, C. T. Lim, and S. Suresh, “Mechanics of the human red blood cell deformed by optical tweezers,” in Journal of the Mechanics and Physics of Solids, 2003, vol. 51, no. 11–12, pp. 2259–2280.

[52] C. T. Lim and M. Dao, “Large deformation of living cells using laser traps,” vol. 52, pp. 1837–1845, 2004.

[53] G. M. Whitesides, “The origins and the future of microfluidics,” Nat. Mater., vol. 442, pp. 368–373, 2006.

[54] J. M. Kwan, Q. Guo, D. L. Kyluik-Price, H. Ma, and M. D. Scott, “Microfluidic analysis of cellular deformability of normal and oxidatively damaged red blood cells.,” Am. J. Hematol., vol. 88, no. 8, pp. 682–9, Aug. 2013.

[55] J. P. Shelby, J. White, K. Ganesan, P. K. Rathod, and D. T. Chiu, “A microfluidic model for single-cell capillary obstruction by Plasmodium falciparum- infected erythrocytes,” vol. 100, no. 25, pp. 14618–14622, 2003.

[56] Y. Oni et al., “Gold nanoparticles for cancer detection and treatment: The role of adhesion,” J. Appl. Phisics, vol. 115, no. 084305, pp. 1–9, 2014.

[57] E. Hampp, R. Botah, O. Odusanya, N. Anuku, K. Malatesta, and W. Soboyejo, “Biosynthesis and adhesion of gold nanoparticles for breast cancer detection and treatment,” J. Mater. Res., vol. 27, no. 22, pp. 2891–2901, 2012.

[58] J. Meng, E. Paetzell, a. Bogorad, and W. O. Soboyejo, “Adhesion between peptides/antibodies and breast cancer cells,” J. Appl. Phys., vol. 107, no. 11, p. 114301, 2010.

[59] J. D. Obayemi et al., “Adhesion of ligand-conjugated biosynthesized magnetite nanoparticles to triple negative breast cancer cells,” J. Mech. Behav. Biomed. Mater., vol. 68, no. January, pp. 276–286, Apr. 2017.

[60] L. Wang, “Early diagnosis of breast cancer,” Sensors (Switzerland), vol. 17, no. 7, 2017.

[61] H. D. Nelson, K. Tyne, A. Naik, C. Bougatsos, B. K. Chan, and L. Humphrey, “Screening for breast cancer: An update for the U.S. Preventive Services Task Force,” Annals of Internal Medicine, vol. 151, no. 10. pp. 727–737, 2009.

[62] E. R. Sauter, “Reliable Biomarkers to Identify New and Recurrent Cancer,” Eur. J. Breast Heal., vol. 13, no. 4, pp. 162–167, 2017.

[63] J. D. Obayemi et al., “Adhesion of Ligand-Conjugated Biosynthesized Magnetite Nanoparticles to Triple Negative Breast Cancer Cells,” J. Mech. Behav. Biomed. Mater., 2017.

[64] J. Hu, S. Youssefian, J. Obayemi, K. Malatesta, N. Rahbar, and W. Soboyejo, “Investigation of adhesive interactions in the specific targeting of Triptorelin-conjugated PEG-coated magnetite nanoparticles to breast cancer cells,” Acta Biomater., vol. 71, no. February, pp. 363–378, 2018.

[65] K. J. Painter, N. J. Armstrong, and J. A. Sherratt, “The impact of adhesion on cellular invasion processes in cancer and development,” J. Theor. Biol., vol. 264, no. 3, pp. 1057–1067, Jun. 2010.

[66] D. Alsteens, H. E. Gaub, R. Newton, M. Pfreundschuh, C. Gerber, and D. J. Müller, “Atomic force microscopy-based characterization and design of biointerfaces,” Nat. Rev. Mater., vol. 2, no. 5, 2017.

[67] D. Alsteens, H. Trabelsi, P. Soumillion, and Y. F. Dufrêne, “Multiparametric atomic force microscopy imaging of single bacteriophages extruding from living bacteria,” Nat. Commun., vol. 4, pp. 4–5, 2013.

[68] C. Lo Giudice, A. C. Dumitru, and D. Alsteens, “Probing ligand-receptor bonds in physiologically relevant conditions using AFM,” Anal. Bioanal. Chem., vol. 411, no. 25, pp. 6549–6559, 2019.

[69] F. Kienberger, A. Ebner, H. J. Gruber, and P. Hinterdorfer, “Molecular recognition imaging and force spectroscopy of single biomolecules,” Acc. Chem. Res., vol. 39, no. 1, pp. 29–36, 2006.

[70] P. Hinterdorfer, W. Baumgartner, H. J. Gruber, K. Schilcher, and H. Schindler, “Detection and localization of individual antibody-antigen recognition events by atomic force microscopy,” Proc. Natl. Acad. Sci. U. S. A., vol. 93, no. 8, pp. 3477–3481, 1996.

[71] S. Suresh et al., “Reprint of: Connections between single-cell biomechanics and human disease states: Gastrointestinal cancer and malaria,” Acta Biomater., vol. 23, no. S, pp. S3–S15, 2015.

[72] M. E. Grady, R. J. Composto, and D. M. Eckmann, “Cell elasticity with altered cytoskeletal architectures across multiple cell types,” J. Mech. Behav. Biomed. Mater., vol. 61, pp. 197–207, Aug. 2016.

[73] H. W. Hou, Q. S. Li, G. Y. H. Lee, A. P. Kumar, C. N. Ong, and C. T. Lim, “Deformability study of breast cancer cells using microfluidics,” Biomed. Microdevices, vol. 11, no. 3, pp. 557–564, 2009.

[74] S. Qiu et al., “Characterizing viscoelastic properties of breast cancer tissue in a mouse model using indentation,” J. Biomech., vol. 69, pp. 81–89, 2018.

[75] A. N. Ketene, E. M. Schmelz, P. C. Roberts, and M. Agah, “The effects of cancer progression on the viscoelasticity of ovarian cell cytoskeleton structures,” Nanomedicine Nanotechnology, Biol. Med., vol. 8, no. 1, pp. 93–102, Jan. 2012.

[76] Z. Farfel, “Receptor-mediated endocytosis,” Harefuah, vol. 116, no. 6, p. 340, 1989.

[77] H. Gao, W. Shi, and L. B. Freund, “Mechanics of receptor-mediated endocytosis,” Proc. Natl. Acad. Sci., vol. 102, no. 27, pp. 3–8, 2005.

[78] F. Osaki, T. Kanamori, S. Sando, T. Sera, and Y. Aoyama, “A Quantum Dot Conjugated Sugar Ball and Its Cellular Uptake. On the Size Effects of Endocytosis in the Subviral Region Scheme 2. Formation of GNP and Glycovirus from 1a,” J. AM. CHEM. SOC, vol. 126, pp. 6520–6521, 2004.

[79] S. Zhang, H. Gao, and G. Bao, “Physical Principles of Nanoparticle Cellular Endocytosis,” ACS Nano, vol. 9, no. 9, pp. 8655–8671, 2015.

[80] S. Xu, B. Z. Olenyuk, C. T. Okamoto, and S. F. Hamm-Alvarez, “Targeting receptor-mediated endocytotic pathways with nanoparticles: Rationale and advances,” Adv. Drug Deliv. Rev., vol. 65, no. 1, pp. 121–138, Jan. 2013.

[81] M. Deserno, “Elastic deformation of a fluid membrane upon colloid binding,” Phys. Rev. E - Stat. Nonlinear, Soft Matter Phys., vol. 69, no. 3 1, pp. 1–14, 2004.

[82] S. Tzlil, M. Deserno, W. M. Gelbart, and A. Ben-Shaul, “A Statistical-Thermodynamic Model of Viral Budding,” Biophys. J., vol. 86, no. 4, pp. 2037–2048, 2004.

[83] X. Yi and H. Gao, “Kinetics of receptor-mediated endocytosis of elastic nanoparticles,” Nanoscale, vol. 9, no. 1, pp. 454–463, 2017.

[84] H. R. Kim et al., “Low-density lipoprotein receptor-mediated endocytosis of PEGylated nanoparticles in rat brain endothelial cells,” Cell. Mol. Life Sci., vol. 64, no. 3, pp. 356–364, 2007.

[85] P. Decuzzi and M. Ferrari, “The role of specific and non-specific interactions in receptor-mediated endocytosis of nanoparticles,” Biomaterials, vol. 28, no. 18, pp. 2915–2922, Jan. 2007.

[86] L. B. Freund and Y. Lin, “The role of binder mobility in spontaneous adhesive contact and implications for cell adhesion,” J. Mech. Phys. Solids, vol. 52, no. 11, pp. 2455–2472, Nov. 2004.

[87] L. Shang et al., “Nanoparticle interactions with live cells: Quantitative fluorescence microscopy of nanoparticle size effects,” Beilstein J. Nanotechnol., vol. 5, no. 1, pp. 2388–2397, 2014.

[88] D. M. Richards and R. G. Endres, “The Mechanism of Phagocytosis : Two Stages of Engulfment,” Biophysj, vol. 107, no. 7, pp. 1542–1553, 2014.

[89] H. Yuan and S. Zhang, “Effects of particle size and ligand density on the kinetics of receptor-mediated endocytosis of nanoparticles,” Appl. Phys. Lett., vol. 96, no. 3, p. 33704, 2010.

[90] C. Boyoglu et al., “Microscopic Studies of Various Sizes of Gold Nanoparticles and Their Cellular Localizations,” ISRN Nanotechnol., vol. 2013, pp. 1–13, 2013.

[91] A. Verma and F. Stellacci, “Effect of surface properties on nanoparticle-cell interactions,” Small, vol. 6, no. 1. pp. 12–21, 2010.

[92] J. Lee, D. K. Chatterjee, M. H. Lee, and S. Krishnan, “Gold nanoparticles in breast cancer treatment: Promise and potential pitfalls,” Cancer Letters, vol. 347, no. 1. pp. 46–53, 2014.

[93] P. Quinn, G. Griffiths, and G. Warren, “Density of newly synthesized plasma membrane proteins in intracellular membranes II. Biochemical studies,” J. Cell Biol., vol. 98, no. 6, pp. 2142–2147, 1984.

[94] H. Garoff and K. Simons, “Location of the spike glycoproteins in the Semliki Forest virus membrane,” Proc. Natl. Acad. Sci. U. S. A., vol. 71, no. 10, pp. 3988–3992, 1974.

[95] H. Yuan, C. Huang, and S. Zhang, “Virus-Inspired Design Principles of Nanoparticle-Based Bioagents,” PLoS One, vol. 5, no. 10, p. 13495, 2010.

[96] R. V Acha, F. J. Martinez-Veracoechea, and D. Frenkel, “Receptor-Mediated Endocytosis of Nanoparticles of Various Shapes,” Nano Lett, vol. 11, p. 55, 2011.

[97] J. Meng et al., “LHRH-functionalized superparamagnetic iron oxide nanoparticles for breast cancer targeting and contrast enhancement in MRI,” Mater. Sci. Eng. C, vol. 29, no. 4, pp. 1467–1479, 2009.

[98] J. Hu, J. D. Obayemi, K. Malatesta, A. Košmrlj, and W. O. Soboyejo, “Enhanced cellular uptake of LHRH-conjugated PEG-coated magnetite nanoparticles for specific targeting of triple negative breast cancer cells,” Mater. Sci. Eng. C, 2018.

[99] J. Hu, J. D. Obayemi, K. Malatesta, A. Košmrlj, and W. O. Soboyejo, “Enhanced cellular uptake of LHRH-conjugated PEG-coated magnetite nanoparticles for specific targeting of triple negative breast cancer cells,” Mater. Sci. Eng. C, vol. 88, no. March, pp. 32–45, 2018.

[100] J. Hu, J. D. Obayemi, K. Malatesta, A. Košmrlj, and W. O. Soboyejo, “Enhanced cellular uptake of LHRH-conjugated PEG-coated magnetite nanoparticles for specific targeting of triple negative breast cancer cells,” Mater. Sci. Eng. C, vol. 88, no. July 2017, pp. 32–45, 2018.

[101] E. Dickens and S. Ahmed, “Principles of cancer treatment by chemotherapy,” Surg. (United Kingdom), vol. 36, no. 3, pp. 134–138, 2018.

[102] J. Collignon, L. Lousberg, H. Schroeder, and G. Jerusalem, “Triple-negative breast cancer: Treatment challenges and solutions,” Breast Cancer Targets Ther., vol. 8, pp. 93–107, 2016.

[103] M. Kalimutho, K. Parsons, D. Mittal, J. A. López, S. Srihari, and K. K. Khanna, “Targeted Therapies for Triple-Negative Breast Cancer: Combating a Stubborn Disease,” Trends in Pharmacological Sciences, vol. 36, no. 12. Elsevier Current Trends, pp. 822–846, 01-Dec-2015.

[104] M. Kalimutho, K. Parsons, D. Mittal, J. A. López, S. Srihari, and K. K. Khanna, “Targeted Therapies for Triple-Negative Breast Cancer: Combating a Stubborn Disease,” Trends Pharmacol. Sci., vol. 36, no. 12, pp. 822–846, Dec. 2015.

[105] L. Y. Xia, Q. L. Hu, J. Zhang, W. Y. Xu, and X. S. Li, “Survival outcomes of neoadjuvant versus adjuvant chemotherapy in triple-negative breast cancer: A meta-analysis of 36,480 cases,” World J. Surg. Oncol., vol. 18, no. 1, pp. 1–8, 2020.

[106] H. Masuda et al., “Predictive factors for the eVectiveness of neoadjuvant chemotherapy and prognosis in triple-negative breast cancer patients,” Cancer Chemother Pharmacol, vol. 67, pp. 911–917, 2011.

[107] O. Gluz, C. Liedtke, N. Gottschalk, L. Pusztai, U. Nitz, and N. Harbeck, “Triple-negative breast cancer - Current status and future directions,” Ann. Oncol., vol. 20, no. 12, pp. 1913–1927, 2009.

[108] A. R. T. Bergin and S. Loi, “Triple-negative breast cancer: Recent treatment advances [version 1; peer review: 2 approved],” F1000Research, vol. 8, 2019.

[109] S. Al-Mahmood, J. Sapiezynski, O. B. Garbuzenko, and T. Minko, “Metastatic and triple-negative breast cancer: challenges and treatment options,” Drug Deliv. Transl. Res., vol. 8, no. 5, pp. 1483–1507, 2018.

[110] K. Bukowski, M. Kciuk, and R. Kontek, “Mechanisms of multidrug resistance in cancer chemotherapy,” Int. J. Mol. Sci., vol. 21, no. 9, May 2020.

[111] S. Keith and G. E. Keith, Treatment of cancer, 5th Editio., vol. 2, no. 2503. London, 1908.

[112] M. Núñez Abad et al., “Update on systemic treatment in early triple negative breast cancer,” Ther. Adv. Med. Oncol., vol. 13, 2021.

[113] J. Collignon, L. Lousberg, H. Schroeder, and G. Jerusalem, “Triple-negative breast cancer: Treatment challenges and solutions,” Breast Cancer Targets Ther., vol. 8, pp. 93–107, 2016.

[114] S. Zhao, W.-J. Zuo, Z.-M. Shao, Y.-Z. Jiang, and Y.-Z. Jiang Fudan, “Molecular subtypes and precision treatment of triple-negative breast cancer,” Ann Transl Med, vol. 8, no. 7, p. 499, 2020.

[115] V. G. Abramson and I. A. Mayer, “Molecular heterogeneity of triple-negative breast cancer,” Curr. Breast Cancer Rep., vol. 6, no. 3, pp. 154–158, 2014.

[116] Y. T. Lee, Y. J. Tan, and C. E. Oon, “Molecular targeted therapy: Treating cancer with specificity,” Eur. J. Pharmacol., vol. 834, no. January, pp. 188–196, 2018.

[117] L. Yin, J. J. Duan, X. W. Bian, and S. C. Yu, “Triple-negative breast cancer molecular subtyping and treatment progress,” Breast Cancer Res., vol. 22, no. 1, pp. 1–13, 2020.

[118] L.-M. Tseng et al., “A comparison of the molecular subtypes of triple-negative breast cancer among non-Asian and Taiwanese women,” Breast Cancer Res. Treat., vol. 163, pp. 241–254, 2017.

[119] T. G. Lyons, “Targeted Therapies for Triple-Negative Breast Cancer,” Curr. Treat. Options Oncol., vol. 20, no. 11, p. 82, 2019.

[120] S. E. Park et al., “Induction of apoptosis in MDA-MB-231 human breast carcinoma cells with an ethanol extract of Cyperus rotundus L. by activating caspases,” Oncol. Rep., vol. 32, no. 6, pp. 2461–2470, 2014.

[121] B. D. B. Lehmann et al., “Identification of human triple-negative breast cancer subtypes and preclinical models for selection of targeted therapies,” J. Clin. Invest., vol. 121, no. 7, pp. 2750–2767, 2011.

[122] P. Ganesan et al., “Triple-negative breast cancer patients treated at MD Anderson Cancer Center in phase I trials: Improved outcomes with combination chemotherapy and targeted agents,” Mol. Cancer Ther., vol. 13, no. 12, pp. 3175–3184, 2014.

[123] I. Migliaccio, A. Di Leo, and L. Malorni, “Cyclin-dependent kinase 4/6 inhibitors in breast cancer therapy.,” Curr. Opin. Oncol., vol. 26, no. 6, pp. 568–575, Nov. 2014.

[124] S. R. Vora et al., “Ribociclib (LEE011) and letrozole in estrogen receptor-positive (ER+) , HER2-negative (HER2-) advanced breast cancer (aBC): phase Ib safety, preliminary efficacy and molecular analysis.,” J. Clin. Oncol., vol. 26, no. 1, pp. 136–149, 2015.

[125] J. L. Dean et al., “Therapeutic response to CDK4/6 inhibition in breast cancer defined by ex vivo analyses of human tumors,” Cell Cycle, vol. 11, no. 14, pp. 2756–2761, 2012.

[126] A. K. McClendon et al., “CDK4/6 inhibition antagonizes the cytotoxic response to anthracycline therapy,” Cell Cycle, vol. 11, no. 14, pp. 2747–2755, 2012.

[127] P. Dent, Y. Tang, A. Yacoub, Y. Dai, P. B. Fisher, and S. Grant, “CHK1 inhibitors in combination chemotherapy thinking beyond the cell cycle,” Mol. Interv., vol. 11, no. 2, pp. 133–140, 2011.

[128] A. Juvekar et al., “Combining a PI3K inhibitor with a PARP inhibitor provides an effective therapy for BRCA1-related breast cancer,” Cancer Discov., vol. 2, no. 11, pp. 1048–1063, 2012.

[129] S. Loi et al., “Tumor infiltrating lymphocytes are prognostic in triple negative breast cancer and predictive for trastuzumab benefit in early breast cancer: Results from the FinHER trial,” Ann. Oncol., vol. 25, no. 8, pp. 1544–1550, 2014.

[130] S. K. Skriver, M. B. Jensen, A. S. Knoop, B. Ejlertsen, and A. V. Laenkholm, “Tumour-infiltrating lymphocytes and response to neoadjuvant letrozole in patients with early oestrogen receptor-positive breast cancer: Analysis from a nationwide phase II DBCG trial,” Breast Cancer Res., vol. 22, no. 1, pp. 1–8, 2020.

[131] S. Adams et al., “Prognostic value of tumor-infiltrating lymphocytes in triple-negative breast cancers from two phase III randomized adjuvant breast cancer trials: ECOG 2197 and ECOG 1199.,” J. Clin. Oncol. Off. J. Am. Soc. Clin. Oncol., vol. 32, no. 27, pp. 2959–2966, Sep. 2014.

[132] R. R. Rosato et al., “Evaluation of anti-PD-1-based therapy against triple-negative breast cancer patient-derived xenograft tumors engrafted in humanized mouse models,” Breast Cancer Res., vol. 20, no. 1, pp. 1–16, 2018.

[133] M. Toporkiewicz, J. Meissner, L. Matusewicz, A. Czogalla, and A. F. Sikorski, “Toward a magic or imaginary bullet? Ligands for drug targeting to cancer cells: Principles, hopes, and challenges,” Int. J. Nanomedicine, vol. 10, pp. 1399–1414, 2015.

[134] G. Zhu, G. Niu, and X. Chen, “Aptamer-Drug Conjugates,” Bioconjug. Chem., vol. 26, no. 11, pp. 2186–2197, 2015.

[135] M. Giulio Casi and D. Neri, “Antibody−Drug Conjugates and Small Molecule−Drug Conjugates: Opportunities and Challenges for the Development of Selective Anticancer Cytotoxic Agents,” J. Med. Chem, vol. 37, p. 52, 1950.

[136] A. Bardia et al., “JOURNAL OF CLINICAL ONCOLOGY Efficacy and Safety of Anti-Trop-2 Antibody Drug Conjugate Sacituzumab Govitecan (IMMU-132) in Heavily Pretreated Patients With Metastatic Triple-Negative Breast Cancer,” J Clin Oncol, vol. 35, pp. 2141‑2148, 2017.

[137] L. Peng, R. Liu, J. Marik, X. Wang, Y. Takada, and K. S. Lam, “Combinatorial chemistry identifies high-affinity peptidomimetics against α4β1 integrin for in vivo tumor imaging,” Nat. Chem. Biol., vol. 2, no. 7, pp. 381–389, 2006.

[138] K. Xiao et al., “LHRH-Targeted Redox-Responsive Crosslinked Micelles Impart Selective Drug Delivery and Effective Chemotherapy in Triple-Negative Breast Cancer,” Adv. Healthc. Mater., vol. 10, no. 3, 2021.

[139] V. Thakur and R. V. Kutty, “Recent advances in nanotheranostics for triple negative breast cancer treatment,” J. Exp. Clin. Cancer Res., vol. 38, no. 1, pp. 1–22, 2019.

[140] B. D. Ratner, A. S. Hoffman, F. J.Schoen, and J. E.Lemons, Biomaterialscience, 2nd Editio. London: Elsevier Academic Press, 2004.

[141] I. Ekladious, Y. L. Colson, and M. W. Grinstaff, “Polymer–drug conjugate therapeutics: advances, insights and prospects,” Nature Reviews Drug Discovery, vol. 18, no. 4. pp. 273–294, 2019.

[142] P. L. Turecek, M. J. Bossard, F. Schoetens, and I. A. Ivens, “PEGylation of Biopharmaceuticals: A Review of Chemistry and Nonclinical Safety Information of Approved Drugs,” J. Pharm. Sci., vol. 105, no. 2, pp. 460–475, 2016.

[143] M. Alas, A. Saghaeidehkordi, and K. Kaur, “Peptide−Drug Conjugates with Different Linkers for Cancer Therapy,” Cite This J. Med. Chem, vol. 64, p. 232, 2021.

[144] G. Huang et al., “Affinity manipulation of surface-conjugated RGD peptide to modulate binding of liposomes to activated platelets,” Biomaterials, vol. 29, no. 11, pp. 1676–1685, 2008.

[145] D. Alloatti et al., “Camptothecins in tumor homing via an RGD sequence mimetic,” Bioorg. Med. Chem. Lett., vol. 22, no. 20, pp. 6509–6512, Oct. 2012.

[146] E. V YoungLai and E. C. Todoroff, “The pituitary gonadotropin-releasing hormone (GnRH) receptor of the female rabbit: characterization and developmental aspects.,” Can. J. Physiol. Pharmacol., vol. 70, no. 12, pp. 1639–1646, Dec. 1992.

[147] S. S. Kakar, H. Jin, B. Hong, J. W. Eaton, and K. A. Kang, “LHRH receptor targeted therapy for breast cancer,” Adv. Exp. Med. Biol., vol. 614, pp. 285–296, 2008.

[148] J. B. Engel and A. V. Schally, “Drug insight: Clinical use of agonists and antagonists of luteinizing-hormone-releasing hormone,” Nat. Clin. Pract. Endocrinol. Metab., vol. 3, no. 2, pp. 157–167, 2007.

[149] C. W. Kwok, O. Treeck, S. Buchholz, S. Seitz, O. Ortmann, and J. B. Engel, “Receptors for luteinizing hormone-releasing hormone (GnRH) as therapeutic targets in triple negative breast cancers (TNBC),” Target. Oncol., vol. 10, no. 3, pp. 365–373, 2015.

[150] S. Seitz et al., “Triple negative breast cancers express receptors for LHRH and are potential therapeutic targets for cytotoxic LHRH-analogs, AEZS 108 and AEZS 125,” 2014.

[151] S. Buchholz et al., “Triple-negative breast cancers express receptors for luteinizing hormone-releasing hormone (LHRH) and respond to LHRH antagonist Cetrorelix with growth inhibition,” Int. J. Oncol., vol. 35, pp. 789–796, 2009.

[152] A. M. Bajo, A. V Schally, and G. Halmos, “Targeted Doxorubicin-containing Luteinizing Hormone-releasing Hormone Analogue AN-152 Inhibits the Growth of Doxorubicin-resistant MX-1 Human Breast Cancers Targeted Doxorubicin-containing Luteinizing Hormone-releasing Hormone Analogue AN-152 Inhibits the,” Clin. Cancer Res., vol. 9, pp. 3742–3748, 2003.

[153] J. D. Obayemi et al., “LHRH-Conjugated Drugs as Targeted Therapeutic Agents for the Specific Targeting and Localized Treatment of Triple Negative Breast Cancer,” Sci. Rep., 2020.

[154] Y. Oni et al., “Gold nanoparticles for cancer detection and treatment: The role of adhesion,” J. Appl. Phys., vol. 115, no. 8, 2014.

[155] H. K. Sun, H. J. Ji, H. L. Soo, W. K. Sung, and G. P. Tae, “LHRH receptor-mediated delivery of siRNA using polyelectrolyte complex micelles self-assembled from siRNA-PEG-LHRH conjugate and PEI,” Bioconjug. Chem., vol. 19, no. 11, pp. 2156–2162, 2008.

[156] J. S. Duncan et al., “Dynamic reprogramming of the kinome in response to targeted MEK inhibition in triple-negative breast cancer,” Cell, vol. 149, no. 2, pp. 307–321, 2012.

[157] G. Hatzivassiliou et al., “ERK inhibition overcomes acquired resistance to MEK Inhibitors,” Mol. Cancer Ther., vol. 11, no. 5, pp. 1143–1154, 2012.

[158] A. A. Midland et al., “Defining the expressed breast cancer kinome,” Cell Res., vol. 22, no. 4, pp. 620–623, 2012.

[159] T. A. Yap, A. Omlin, and J. S. de Bono, “Development of therapeutic combinations targeting major cancer signaling pathways.,” J. Clin. Oncol. Off. J. Am. Soc. Clin. Oncol., vol. 31, no. 12, pp. 1592–1605, Apr. 2013.

[160] K. Yang, H. Bai, Q. Ouyang, L. Lai, and C. Tang, “Finding multiple target optimal intervention in disease-related molecular network,” Mol. Syst. Biol., vol. 4, no. 228, 2008.

[161] A. E. Motter, “Improved network performance via antagonism: From synthetic rescues to multidrug combinations,” BioEssays, vol. 32, no. 3, pp. 236–245, 2010.

[162] M. Hasan, R. K. Leak, R. E. Stratford, D. P. Zlotos, and P. A. Witt-Enderby, “Drug conjugates—an emerging approach to treat breast cancer,” Pharmacol. Res. Perspect., vol. 6, no. 4, 2018.

[163] J. B. Wolinsky, Y. L. Colson, and M. W. Grinstaff, “Local drug delivery strategies for cancer treatment: Gels, nanoparticles, polymeric films, rods, and wafers,” J. Control. Release, vol. 159, no. 1, pp. 14–26, 2012.

[164] R. B. Weiss, “Hypersensitivity reactions from taxol,” J. Clin. Oncol., vol. 8, no. 7, pp. 1263–1268, Jul. 1990.

[165] H. Gelderblom, J. Verweij, K. Nooter, and A. Sparreboom, “Cremophor EL: the drawbacks and advantages of vehicle selection for drug formulation,” Eur. J. Cancer, vol. 37, no. 13, pp. 1590–1598, Sep. 2001.

[166] J. K. Vasir and V. Labhasetwar, “Targeted drug delivery in cancer therapy.,” Technol. Cancer Res. Treat., vol. 4, no. 4, pp. 363–374, 2005.

[167] C. Polgár and T. Major, “Current status and perspectives of brachytherapy for breast cancer,” Int. J. Clin. Oncol., vol. 14, no. 1, pp. 7–24, 2009.

[168] I. Major and C. McConville, “Vaginal drug delivery for the localised treatment of cervical cancer,” Drug Deliv. Transl. Res., vol. 7, no. 6, pp. 817–828, 2017.

[169] X. Wang, S. Liu, Y. Guan, J. Ding, C. Ma, and Z. Xie, “Vaginal drug delivery approaches for localized management of cervical cancer,” Adv. Drug Deliv. Rev., vol. 174, pp. 114–126, Jul. 2021.

[170] D. Y. Fan, Y. Tian, and Z. J. Liu, “Injectable Hydrogels for Localized Cancer Therapy,” Front. Chem., vol. 7, p. 675, 2019.

[171] A. C. Anselmo and S. Mitragotri, “An overview of clinical and commercial impact of drug delivery systems,” Journal of Controlled Release, vol. 190. Elsevier, pp. 15–28, 28-Sep-2014.

[172] L. Nam et al., “Drug delivery nanosystems for the localized treatment of glioblastoma multiforme,” Materials (Basel)., vol. 11, no. 5, 2018.

[173] S. E. Shackney, G. W. McCormack, and G. J. J. Cuchural, “Growth rate patterns of solid tumors and their relation to responsiveness to therapy: an analytical review.,” Ann. Intern. Med., vol. 89, no. 1, pp. 107–121, Jul. 1978.

[174] V. Keskar, P. S. Mohanty, E. J. Gemeinhart, and R. A. Gemeinhart, “Cervical cancer treatment with a locally insertable controlled release delivery system,” J. Control. Release, vol. 115, no. 3, pp. 280–288, Oct. 2006.

[175] A. Fernandez-Fernandez, R. Manchanda, and A. J. McGoron, “Theranostic applications of nanomaterials in cancer: Drug delivery, image-guided therapy, and multifunctional platforms,” Appl. Biochem. Biotechnol., vol. 165, no. 7–8, pp. 1628–1651, 2011.

[176] G. T. Hermanson, “Liposome Conjugates and Derivatives,” Bioconjugate Tech., pp. 921–949, 2013.

[177] D. R. Khan, “The use of nanocarriers for drug delivery in cancer therapy,” J. Cancer Sci. Ther., vol. 2, no. 3, pp. 58–62, 2010.

[178] S. G. Antimisiaris et al., “Overcoming barriers by local drug delivery with liposomes,” Adv. Drug Deliv. Rev., vol. 174, pp. 53–86, Jul. 2021.

[179] R. De Souza, P. Zahedi, C. J. Allen, and M. Piquette-Miller, “Polymeric drug delivery systems for localized cancer chemotherapy,” Drug Deliv., vol. 17, no. 6, pp. 365–375, 2010.

[180] M. Khodadadi, S. Alijani, M. Montazeri, N. Esmaeilizadeh, S. Sadeghi-Soureh, and Y. Pilehvar-Soltanahmadi, “Recent advances in electrospun nanofiber-mediated drug delivery strategies for localized cancer chemotherapy,” J. Biomed. Mater. Res. - Part A, vol. 108, no. 7, pp. 1444–1458, 2020.

[181] M. M. Essawy et al., “Function of gold nanoparticles in oral cancer beyond drug delivery: Implications in cell apoptosis,” Oral Dis., vol. 27, no. 2, pp. 251–265, 2021.

[182] A. Rodzinski et al., “Targeted and controlled anti-cancer drug delivery and release with magnetoelectric nanoparticles,” Sci. Rep., vol. 6, 2016.

[183] F. Danhier, O. Feron, and V. Préat, “To exploit the tumor microenvironment: Passive and active tumor targeting of nanocarriers for anti-cancer drug delivery,” Journal of Controlled Release, vol. 148, no. 2. pp. 135–146, 2010.

[184] J. H. Lee and A. Nan, “Combination Drug Delivery Approaches in Metastatic Breast Cancer,” J. Drug Deliv., vol. 2012, pp. 1–17, 2012.

[185] K. Cho, X. Wang, S. Nie, Z. G. Chen, and D. M. Shin, “Therapeutic nanoparticles for drug delivery in cancer.,” Clin. Cancer Res., vol. 14, no. 5, pp. 1310–6, 2008.

[186] S. M. Jusu et al., “Drug-encapsulated blend of PLGA-PEG microspheres: in vitro and in vivo study of the effects of localized/targeted drug delivery on the treatment of triple-negative breast cancer,” Sci. Rep., vol. 10, no. 1, p. 14188, 2020.

[187] B. Pelaz et al., “Surface Functionalization of Nanoparticles with Polyethylene Glycol: Effects on Protein Adsorption and Cellular Uptake,” ACS Nano, vol. 9, no. 7, pp. 6996–7008, 2015.

[188] B. Bahmani, S. Gupta, S. Upadhyayula, V. I. Vullev, and B. Anvari, “Effect of polyethylene glycol coatings on uptake of indocyanine green loaded nanocapsules by human spleen macrophages in vitro,” J. Biomed. Opt., vol. 16, no. 5, p. 051303, 2011.

[189] D. Pozzi et al., “Effect of polyethyleneglycol (PEG) chain length on the bio-nano-interactions between PEGylated lipid nanoparticles and biological fluids: From nanostructure to uptake in cancer cells,” Nanoscale, vol. 6, no. 5, pp. 2782–2792, 2014.

[190] R. Mankamna Kumari, N. Sharma, and S. Nimesh, Clinical studies and future prospects. Elsevier Ltd, 2017.

[191] A. A. Exner and G. M. Saidel, “Drug-eluting polymer implants in cancer therapy,” Expert Opin. Drug Deliv., vol. 5, no. 7, pp. 775–788, 2008.

[192] A. Mishra et al., “The Red Blood Cell,” Bioconjugate Tech., vol. 11, no. 1, pp. 1–9, Jul. 2017.

[193] Y. Danyuo et al., “Extended pulsated drug release from PLGA-based minirods,” J. Mater. Sci. Mater. Med., vol. 28, no. 4, 2017.

[194] Y. Danyuo et al., “Swelling of poly(N-isopropylacrylamide) P(NIPA)-based hydrogels with bacterial-synthesized prodigiosin for localized cancer drug delivery,” Mater. Sci. Eng. C, vol. 59, pp. 19–29, 2016.

[195] Y. Danyuo et al., “Prodigiosin Release from an Implantable Biomedical Device: Effect on Cell Viability,” Adv. Mater. Res., vol. 1132, pp. 3–18, 2015.

[196] J. D. Obayemi et al., “Degradable porous drug-loaded polymer scaffolds for localized cancer drug delivery and breast cell/tissue growth,” Mater. Sci. Eng. C, vol. 112, p. 110794, Jul. 2020.

[197] A. B. Fleming and W. M. Saltzman, “Pharmacokinetics of the carmustine implant,” 2002.

[198] A. P. Griset, J. Walpole, R. Liu, A. Gaffey, Y. L. Colson, and M. W. Grinstaff, “Expansile nanoparticles: Synthesis, characterization, and in vivo efficacy of an acid-responsive polymeric drug delivery system,” J. Am. Chem. Soc., vol. 131, no. 7, pp. 2469–2471, 2009.

[199] Y. L. Colson et al., “The performance of expansile nanoparticles in a murine model of peritoneal carcinomatosis,” Biomaterials, vol. 32, no. 3, pp. 832–840, Jan. 2011.

[200] P. Cherukuri, E. S. Glazer, and S. A. Curley, “Targeted hyperthermia using metal nanoparticles,” Adv. Drug Deliv. Rev., vol. 62, no. 3, pp. 339–345, 2010.

[201] K. Kan-Dapaah, N. Rahbar, and W. Soboyejo, “Implantable magnetic nanocomposites for the localized treatment of breast cancer,” J. Appl. Phys., 2014.

[202] T. M. Zagar et al., “Hyperthermia combined with radiation therapy for superficial breast cancer and chest wall recurrence: A review of the randomised data,” Int. J. Hyperth., vol. 26, no. 7, pp. 612–617, 2010.

[203] M. W. Dewhirst, B. L. Viglianti, M. Lora-Michiels, M. Hanson, and P. J. Hoopes, “Basic principles of thermal dosimetry and thermal thresholds for tissue damage from hyperthermia,” in International Journal of Hyperthermia, 2003, vol. 19, no. 3, pp. 267–294.

[204] G. L. DeNardo and S. J. DeNardo, “Turning the heat on cancer,” Cancer Biother. Radiopharm., vol. 23, no. 6, pp. 671–679, 2008.

[205] M. Dewhirst, P. R. Stauffer, S. Das, O. I. Craciunescu, and Z. Vujaskovic, “Hyperthermia,” Clin. Radiat. Oncol., pp. 381-398.e6, Jan. 2016.

[206] P. S. Yarmolenko et al., “Thresholds for thermal damage to normal tissues: An update,” Int. J. Hyperth., vol. 27, no. 4, pp. 320–343, 2011.

[207] H. W. Huang and T. L. Horng, “Bioheat Transfer and Thermal Heating for Tumor Treatment,” Heat Transf. Fluid Flow Biol. Process., pp. 1–42, Jan. 2015.

[208] R. Haghniaz, R. D. Umrani, and K. M. Paknikar, “Temperature-dependent and time-dependent effects of hyperthermia mediated by dextran-coated La0.7Sr0.3MnO3: In vitro studies,” Int. J. Nanomedicine, vol. 10, pp. 1609–1623, 2015.

[209] Y. Zhang et al., “Temperature-dependent cell death patterns induced by functionalized gold nanoparticle photothermal therapy in melanoma cells.”

[210] T. Nguyen, E. Hattery, and V. P. Khatri, “Radiofrequency ablation and breast cancer: a review.,” Gland Surg., vol. 3, no. 2, pp. 128–12835, 2014.

[211] T. P. Ryan and C. L. Brace, “Interstitial microwave treatment for cancer: historical basis and current techniques in antenna design and performance,” International Journal of Hyperthermia, vol. 33, no. 1. pp. 3–14, 2017.

[212] K. Kan-Dapaah, N. Rahbar, A. Tahlil, D. Crosson, N. Yao, and W. Soboyejo, “Mechanical and hyperthermic properties of magnetic nanocomposites for biomedical applications,” J. Mech. Behav. Biomed. Mater., vol. 49, no. April, pp. 118–128, 2015.

[213] R. F. Brem, “Radiofrequency ablation of breast cancer: A step forward,” Radiology, vol. 289, no. 2, pp. 325–326, 2018.

[214] E. Tammam, A. M. Said, A. A. Ibrahim, and A. I. A. Galal, “About the interstitial microwave cancer ablation: Principles, advantages and challenges,” IEEE Access, vol. 8, pp. 49685–49694, 2020.

[215] A. Baeza, D. Arcos, and M. Vallet-Regí, “Thermoseeds for interstitial magnetic hyperthermia: From bioceramics to nanoparticles,” J. Phys. Condens. Matter, vol. 25, no. 48, 2013.

[216] Y. Danyuo et al., “Laser Application of Nanocomposite Hydrogels on Cancer Cell Viability,” MRS Adv., vol. 5, no. 26, pp. 1377–1385, 2020.

Chapter 3.0. Adhesion of Targeted Gold Nanoparticles to Triple Negative Breast Cancer Cells

3.1. Introduction

The need for targeted cancer therapeutics and imaging techniques drives cancer research efforts toward developing various configurations of targeted nanoparticles and drugs[1]–[7].These rely on molecular recognition units (MRU) that can interact with specific receptors that are over-expressed on the surfaces of the cancer cells. There is, therefore, the need to understand the specific interactions (between MRUs and specific receptors on surfaces of cancer cells) to guide the targeted delivery of nanoparticles to tumor sites.

Prior efforts by our research group have explored the adhesion of magnetite nanoparticles to triple negative breast cancer cells (TNBC) using atomic force microscope (AFM) and condensed phase molecule interaction [2], [3]. Magnetite nanoparticles were used in those studies because of their potential for enhancing the contrast of magnetic resonance imaging (MRI) [8]as well as their ability to induce apoptosis due to heating associated with oscillating magnetic fields[9], [10].

Besides its ability to be functionalized with targeted MRU's, gold nanoparticles have also been studied for their plasmon resonant and optical properties [11]–[15]. Their ability to absorb and scatter near-infrared (NIR) wavelengths (700-900 nm) transparent to tissue, hemoglobin and melanin lends itself to enhanced localized heating within cancerous tumors [16], [17].

Our recent efforts have explored alternative synthesis methods for producing gold nanoparticles using bacteria [5], [18], and leaf extract processes [19]. In these studies, we explored the influence of physical parameters (pH, concentration and time) on the synthesis of gold nanoparticles [18],

[19]. These studies also designed Ligand conjugated gold nanoparticles, and measured their adhesion to multiple receptors that are overexpressed on the surfaces of TNBC [4], [5]. However, the stability and adhesion of biosynthesized gold nanoparticles (GNP), PEG-coated biosynthesized gold nanoparticles (GNP-PEG), Triptorelin (TRP)-functionalized biosynthesized gold nanoparticles (GNP-TRP) and Triptorelin (TRP)-functionalized biosynthesized PEG-coated gold nanoparticles (GNP-PEG-TRP) to two types of TNBC have not been studied at an atomic scale using AFM on ligand-receptors interactions.

Within this context, the basic understanding of the interaction between multiple biological cell receptors and multiple ligands could provide a physical basis for the design of nanoparticle structures with well-controlled adhesion characteristics. Hence, this chapter presents results from AFM adhesion experiments in the development of a understanding of the adhesion of ligand-conjugated nanoparticles and receptors on the surfaces of TNBC.

This work presents results from the synthesis, conjugation, and adhesion of various biosynthesized gold nanoparticle systems (GNP, GNP-PEG, GNP-TRP, GNP-PEG-TRP) to two types of TBNC cells (MDA-MB-231 and MDA-MB-468). First, biosynthesized gold nanoparticle systems are characterized.After that, long-term stability studies (6 months) are carried out on all the biosynthesized gold nanoparticle systems in distilled water (DI water). The Adhesive interactions between the biosynthesized gold nanoparticle systems, TNBC, and normal breast cells (MCF10A) are studied using the AFM.

Finally, Alamar blue cell viability studies were carried out on normal non-tumorigenic breast cells (MCF 10A) incubated with all the biosynthesized gold nanoparticle systems. The implications of the results are discussed for the design of ligand-conjugated, PEG-coated gold nanoparticles for the specific targeting of triple-negative breast cancer cells, and laser-assisted photothermal treatment.

3.2.Theory

3.2.1. Atomic Force Spectroscopy

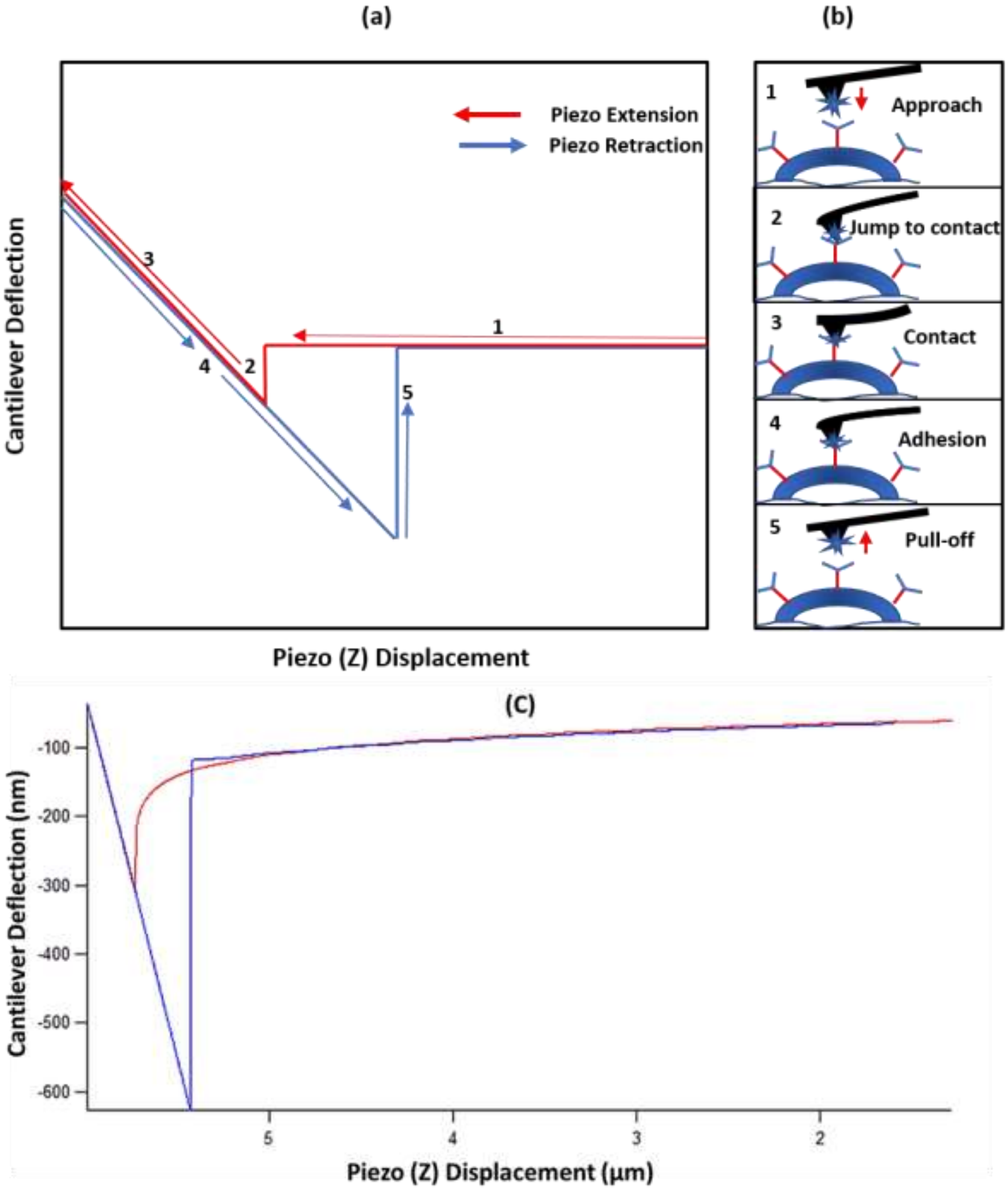

Fig. 3.1. (a) One cycle Deflection–displacement plot with corresponding stages of force displacement behavior (b) In one approach-retract cycle, the AFM tip approaches the sample surface (1), jumps to contact (2), Indents surface (3) detaches (4). AFM tip requires more force to pull off adhered AFM tip from substrate(5)[3], (c) Deflection-Displacement plot showing the interaction between GNP-TRP coated AFM tip and MDA-MB-231 TNBC cell.

At large separations (few micrometers), the attractive forces between the atoms in the tip and the atoms in the sample are almost negligible (Fig.3.1 (a). Upon further reduction in tip sample distance, the tip jumps into contact at point 2. From 2 to 3, the cantilever indents into with the cell until the cantilever deflection reaches a preset set point. At the maximum set point, the cantilever is withdrawn at point 4 but deflects further downwards due to adhesion between the AFM tip and the cell. The additional force required to detach the AFM tip from the cell surface is called the pull-off force. Upon detachment the cantilever returns to its initial position at point 1[20], [21].

The pull off point provides information about the type of interaction happening between the sample and the tip[2]–[5].

The adhesive (pull-off) force can be deduced using to Hooke's law:

$$F = -k_c \delta_c \tag{3.1}$$

where k_c is the force constant of the cantilever and $\delta_c$is the cantilever displacement.

In the presence of a vapor, water or any liquid, a meniscus is formed between the contact of the AFM probe tip and the sample surfaces. The capillary force due to the liquid meniscus arises from the Laplace pressure of the curved menisci (P_L). The liquid between the AFM probe and the surface deflects the cantilever towards the surface by acting as an attractive force.

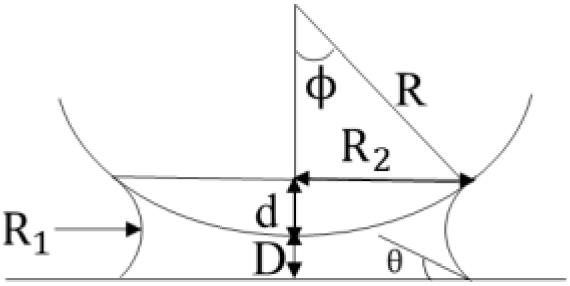

Fig. 3.2. Schematic showing a capillary bridge between a spherical AFM tip and a flat surface. R is the radius of curvature of the AFM tip, R_1 and R_2 are the minimum and maximum curvature radius of the meniscus respectively, ϕ is the fill angle, θ is the contact angle between the liquid and the flat surface, D is the tip-sample separation and d is the AFM tip immersion depth.

$$P_L = \gamma_w \left(\frac{1}{R_1} + \frac{1}{R_2}\right) \tag{3.2}$$

Where R_1 and R_2 are minimum and maximum radius of curvature of the meniscus respectively and γ_w is the surface tension of water.

As the meniscus grows larger $R_2 \to \infty$ and $R_1 \ll R_2$

$$P_L = \gamma_w \left(\frac{1}{R_1}\right) \tag{3.3}$$

Surface area of meniscus between AFM tip and the flat surface is $\approx 2\pi Rd$ (from Fig. 3.2) where R is the radius of curvature of the AFM tip.

Hence, Capillary force $F_{cap} = P_L * 2\pi Rd = 2\pi Rd \frac{\gamma_w}{R_1}$

For small ϕ, $(D + d) \approx 2R_1 \cos\theta$

$$F_{cap} = \frac{4\pi R\gamma_w \cos\theta}{1 + {}^{D}/_{d}} \tag{3.4}$$

At maximum capillary force $D \to 0$

$$F_{cap\_max} = 4\pi R\gamma_w \cos\theta \quad (3.5)$$

At small contact angle ($\theta \rightarrow 0$ for hydrophilic interface), $\text{hence}, \cos\theta \approx 1$

$$F_{cap\_max} = 4\pi R\gamma_w \quad (3.6)$$

3.3. Materials and Experimental Procedures

3.3.1. Synthesis of Gold Nanoparticles

Serratia Marcescens bacteria was obtained and isolated from Sheda Science and Technology Complex (SHESTCO), Abuja, Nigeria. The process of GNP synthesis used was adapted from a previous study done by our group[18]. Gold (III) Chloride Trihydrate (ACS reagent with ≥49.0% Au basis Sigma-Aldrich, St. Louis, USA) was reduced intracellularly and extracellularly using a cell free extract of Serratia Marcescens[18].

Specifically, 5g of Proteose peptone (Sigma-Aldrich, St. Louis, USA) and 10 ml of glycerol (Sigma-Aldrich, St. Louis, USA) were dissolved in 1L of water. The resulting solution was autoclaved for 55 minutes prior to inoculation with Serratia Marcescens in four 250 mL conical flasks. The autoclaved and inoculated solution was kept in an incubator shaker that was vibrated at 90 rpm at a temperature of 32^{o}C for 48 hrs. The resulting culture was centrifuged at 4000 rpm for 15 minutes, while the cell free extract was collected into flasks and stored in a refrigerator at 4^{o}C. Following this, 20 mL cell free extract and 20 mL of a 2.5 mM Tetra-chloro-aurate solution were added to a 50mL Falcon centrifuge tube and incubated in a water bath at 30^{o}C for 1day.

The Biosynthesized Gold Nanoparticles (BGNP) obtained were treated in 1% sodium dodecyl sulfate (SDS) (ACS reagent with ≥99.0% Sigma-Aldrich, St. Louis, USA) [5] to denature the surface bound proteins and heated at 95°C for 30 mins in a vacuum oven. They were then washed three times in Dulbeccos Phosphate Buffer Saline (DPBS) (Life technologies cooperation, Carlsbad, CA) buffer for 15 mins in a centrifuge at 4000 rpm, and twice in in de-ionized water. Following this, BGNPs were concentrated using a centrifugal filter (Amicon Ultra-15, Millipore Billerica, MA) and then re-dissolved in 1 mL of Deionized, Distilled water.

3.3.2. PEGylation of Biosynthesized Gold Nanoparticles

PEGylation of BGNP was done using methyl-PEG$_4$-thiol (MT(PEG)$_4$) and carboxy-PEG$_{12}$-thiol (CT(PEG)$_{12}$) (Thermo Fisher Scientific, Inc. Waltham, MA, USA). These were used in combination to reduce nonspecific protein binding to the nanoparticle surface [22], [23].

A solution of MT(PEG)$_4$ (0.5 mM, 4 mL) and CT(PEG)$_{12}$ (0.5 mM, 4 mL) were added to 10 mL of GNP (0.2 mM) and stirred for 2 h at room temperature. Subsequently, the mixture was washed with DPBS and centrifuged in a spin column with molecular weight cut-off of 50 kDa. The PEG-coated GNPs were resuspended in deionized water.

3.3.3. Ligand Conjugation of PEGylated Biosynthesized Gold Nanoparticles

Conjugation of D-Trp LHRH (BACHEM, Torrance, CA, USA) to GNP and PEG-coated GNP was done using carbodiimide activation process with ethyl (dimethylaminopropyl) carbodiimide (EDC) (Sigma-Aldrich, St. Louis, MO, USA) and N-hydroxysuccinimide (NHS) (Thermo Fisher Scientific, Inc., Waltham, MA, USA)[24][25]. A solution of EDC (13.5 mM, 74µL) and NHS (15.3 mM, 65 µL) were added BGNP (0.2 mM, 5 mL). The mixture was stirred continuously for 2 hours at room temperature and then Triptorelin Ligand (5 mM, 192 µL) added stirred overnight. Subsequently, the mixture was washed with DPBS and centrifuged in a spin column with molecular weight cut-off of 50 kDa. The TRP conjugated PEG-coated GNPs were resuspended in De-ionized.

3.3.4. Stability Studies on Biosynthesized and Conjugated-Gold Nanoparticles

The colloidal stability of GNP, GNP-TRP, GNP-PEG, GNP-PEG-TRP in distilled water, were investigated over a period of six months by measuring the hydrodynamic diameter and zeta potentials using the Malvern Zetasizer (Westborough, MA, USA). The four GNP systems where diluted (0.5mL, 0.2mM) in 0.5 mL of distilled water and their diameter and zeta potentials are measured at month 1, 3 and 6.

3.3.5. Cell Culture and Cell Immobilization

All cell lines used in this study were procured from ATCC, Manassas, Virginia, USA and detailed description of the cell culture and immobilization process has been documented in earlier studies done by our group [2]–[4]. Briefly, 20 µL of 1 x 10^6 of both TNBCs (MDA-MB-231 and MDA-MB-468) and normal breast cells (MCF10A) were grown on 22 x 22 mm sterile uncoated coverslips inside 35 x10 mm sterile Falcon cell culture Petri dishes. The TNBCs were incubated at 37°C under normal atmospheric pressure while the normal breast cells were incubated at 37°C with 5% CO_2 using their respective media [3].

Once 70% confluence of all cells were reached, the samples were fixed with a solution of 4% paraformaldehyde in 0.1 M phosphate Buffer Saline (PBS) (Electron Microscopy Sciences, Hatfield, PA, USA) for 12 min at room temperature (25°C). Fixed cell samples were placed in a vacuum desiccator flask for 2 hours to dry at room temperature prior to cell-nanoparticles adhesion studies.

3.3.6. Coating of AFM Tips

n-doped silicon AFM probes (Bruker, Billerica, MA, USA) were dip-coated using a method detailed previously [26]. This coating method has also been successfully utilized in similar studies done by our group [2]–[4], [6]. Briefly, tips were coated five times with three minutes air drying intervals in solutions containing GNP, TRP, GNP-PEG, GNP-TRP and GNP-PEG-TRP. At least two cantilever probes were used for each configuration.

After the cycle of dip-coating was completed, the coated AFM tips were subjected to a drop of the various GNP systems and air-dried under vacuum in a desiccator flask for a minimum of two hours. Back-scattered electron images of the coated and bare AFM tips are obtained using Environmental Scanning Electron Microscope (ESEM) (FEI Quanta 200 FEG Environmental-SEM, Philips/FEI Corporation, Oregon, USA). These were done to ensure that the tips were coated before and after conducting the AFM adhesion experiments.

3.3.7. Adhesion Measurements

All adhesion experiments in this study were carried using an Asylum MFP3D-Bio atomic force microscope (Asylum Research, Santa Barbara, CA, USA). These measurements were made under ambient conditions at a temperature of 21°C and relative humidity of 20%. Trigger point was 5nN and the photodetector sensitivity was calibrated using a glass slide surface and the spring constant of the coated AFM cantilevers was updated using an in-built thermal tuning application on the Asylum AFM (Table 3.1). The adhesive interactions between the cells (MCF10A, MDA-MB-468 and MDA-MB-231) and each of the probes (bare AFM tips, TRP, GNP, GNP-PEG, GNP-TRP or GNP-PEG-TRP coated tips) were measured. The normal breast cell adhesive interaction with each of the nanoparticle systems served as a positive control with respect to the TNBCs measurements. At least two cantilever probes were used for each configuration and five arbitrary contact regions were selected on the substrates. Within each contact region at least three cells were probed by force mapping hundred points on individual cells over a cell area of 20 x 20 μm^2 .

Table 3.1 Average Spring Constant of Bare and Coated AFM tips

S/N	AFM Tip Coating	Average Spring Constant (N/m)
1	Bare	0.41 ± 0.18
2	GNP	0.38 ± 0.10
3	GNP-TRP	0.66 ± 0.08
4	GNP-PEG	0.54 ± 0.24
5	GNP-PEG-TRP	0.49 ± 0.10

3.3.8. Immunofluorescence Staining for LHRH Receptors

The distribution of LHRH receptors on both TNBC and normal breast cell membranes are revealed using immunofluorescence staining, with the help of fluorescent dyes as shown in previous studies [3], [27]. After 48 h of cell incubation and growth, the cells were fixed for 12 mins in 4% high grade paraformaldehyde solution to preserve their structures. The fixed cells were then permeabilized for 10 mins and treated for 1 h to reduce non-specific binding of the fluorescent dyes using a 0.1% solution of Triton X-100 (Life technologies Corporation, Carlsbad, CA), and 1% bovine serum albumin (BSA) (Sigma- Aldrich, St. Louis, M, USA), respectively. Subsequently, the permeabilized cells are labeled (3 h) with primary anti-LHRH antibody (EMD

Millipore, Darmstadt, Germany) and secondary anti-mouse IgG antibody conjugated with Alexa fluor 488 (thermo Fisher Scientific, Inc., Waltham, MA, USA) for 45 mins. Lastly, the nuclei of the cell samples were stained with 4',6-Diamidino-2-Phenylindole, Dihydrochloride (DAPI) (Sigma-Aldrich, St. Louis, USA). The stained cell samples were mounted on glass slides using 70% glycerol media and sealed using a sealant (Ted Pella, Inc. Redding, CA, USA). The cells were rinsed three times after each stain reagent. All stained and fixed cell samples were imaged with a 40x oil-immersion objective using the Leica TCS SP5 Scanning Confocal Microscope (Leica, Wetzlar, Germany).

3.3.9. Alamar Blue Cell Viability Assay

For toxicity and cell viability studies, MCF10A (normal breast cells) were harvested in the log growth phase using trypsin-EDTA. MCF10A cells were seeded in 24-well plates containing their growth medium [2]. After a 3h attachment window, 1mL of GNP, GNP-PEG, GNP-TRP, GNP-PEG-TRP were added to the normal breast cells at a concentration of 5 µg/mL. Cell viability was observed using Alamar Blue reagent (Thermo Fisher Scientific, Waltham, MA, USA) at intervals of 0, 24, 48 and 72 h after each of the biosynthesized gold nanoparticle systems were added. At each time point, the culture medium was replaced with 1 mL of 10% Alamar Blue solution (in culture medium) and the 24-well plates were incubated at 37 °C and 5% CO_2 for 3 h.

After the 3hr incubation window, 100 µL aliquots were transferred into triplicate wells of black opaque 96-well plate (Thermo Fisher Scientific, Waltham, MA, USA). The fluorescence intensities were measured at 544 nm excitation and 590 nm emission using a 1420 Victor3 multilabel plate reader (Perkin Elmer, Waltham, MA, USA). The percentage of Alamar Blue reduction was determined using alamar blue assay and cell viability study protocols [28].

3.4. Statistical Analysis

The results are presented as mean ± standard deviation for n =3 (unless otherwise stated). One-way repeated measures ANOVA with post hoc Tukey HSD multiple comparisons tests was used to analyze the differences between the cell viabilities (% alamar blue reduction) under different GNP treatments at different exposure durations. Two-way ANOVA with post hoc Tukey HSD multiple comparisons tests was used to analyze the differences in adhesion forces between the different cell types and the AFM tip coating configurations. The statistical analyses were done using IBM SPSS Statistics 26 software with the statistical differences between means considered significant at $p < 0.05$.

3.5.Results

3.5.1. Nanoparticle Biosynthesis, PEGylation, Conjugation and Characterization

UV-Vis spectrophotometry results (Fig. 3.3) for GNP, GNP-TRP, GNP-PEG and GNP-PEG-TRP were ob++tained with maximum absorption wavelengths ($\lambda_{\max}$) at 565, 571, 570 and 569.5 nm respectively. In addition to gold maximum absorption wavelengths, GNP-TRP and GNP-PEG-TRP spectra reveal TRP ligand signatures at 267 nm. There is a 0.8% increase in $\lambda_{\max}$ when GNP is Pegylated (GNP-PEG), 1% increase in $\lambda_{\max}$ when GNP is functionalized with TRP (GNP-TRP) and a 0.7 % increase in $\lambda_{\max}$ when GNP is modified with both PEG and TRP (GNP-PEG-TRP).

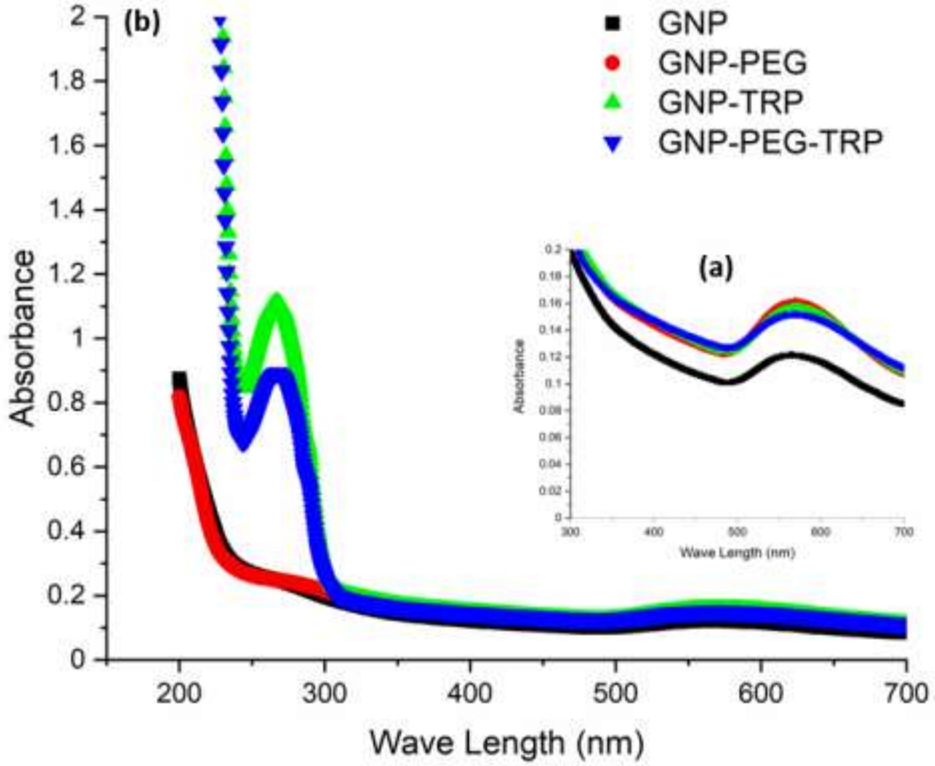

Fig. 3.3. UV-Vis absorption spectra of (a) biosynthesized gold nanoparticle systems (GNP, GNP-PEG, GNP-TRP, GNP-PEG-TRP with maximum absorption wavelengths at 565, 571, 570 and 569.5 nm respectively and TRP ligand signatures at 267 nm (b).

TEM micrographs and core diameter size distribution for the four GNP systems are presented in Fig. 3.4 and Fig. 3.5, respectively. These show predominantly spherical nanoparticles with a broad size distribution of 10 – 30 nm and average diameter sizes of 16.7 ± 4.1 nm (GNP), 15.6 ± 5.6 nm (GNP-TRP), 14.6 ± 4.2 nm (GNP-PEG), and 15.8 ± 4.6 nm (GNP-PEG-TRP). However, the hydrodynamic diameter(D) for the freshly prepared nanoparticles were measured (GNP (64.7 ± 1.0 nm), GNP- TRP (139.7 ± 1.1 nm), GNP-PEG (55.2 ± 0.2 nm), GNP-PEG-TRP (76.9 ± 0.1 nm)) as well as their polydispersity index (PDI) (GNP (0.29 ± 0.05), GNP-TRP (0.22 ± 0.01),

GNP-PEG (0.23 ± 0.00), GNP-PEG-TRP (0.23 ± 0.03)) and zeta potential (ξ) (GNP (-24.9 ± 1.6 mV), GNP-TRP (-26.2 ± 2.9 mV), GNP-PEG (-30.2 ± 1.1 mV), GNP-PEG-TRP (-29.6 ± 0.8 mV)).

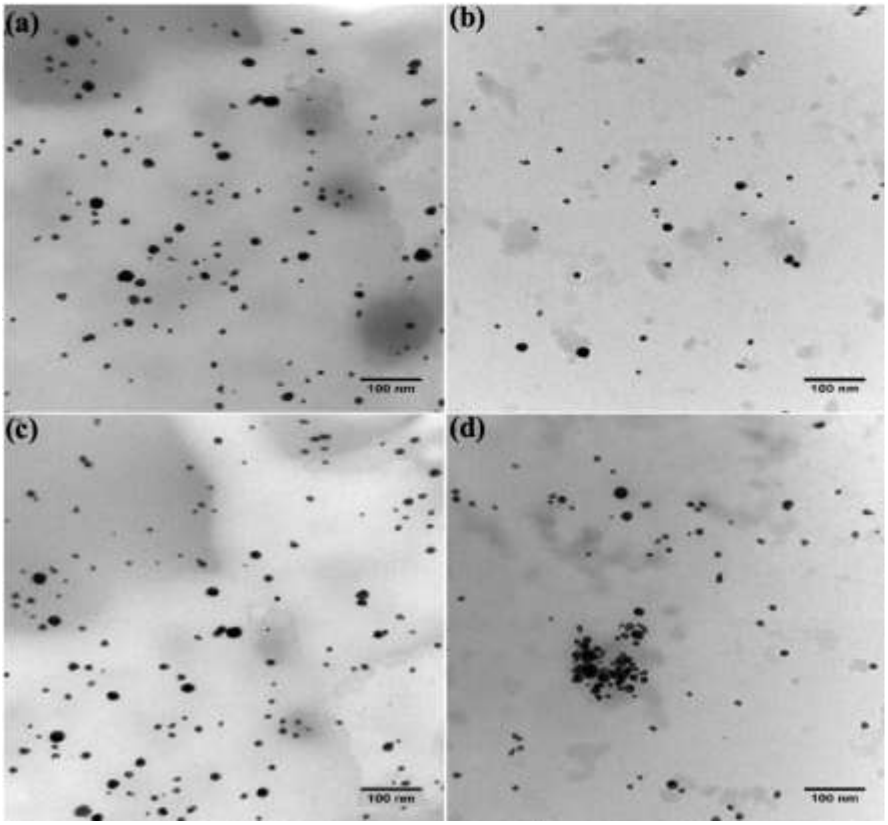

Fig. 3.4. TEM micrographs of (a) GNP; (b) GNP-TRP; (c) GNP-PEG; (d) GNP-PEG-TRP.

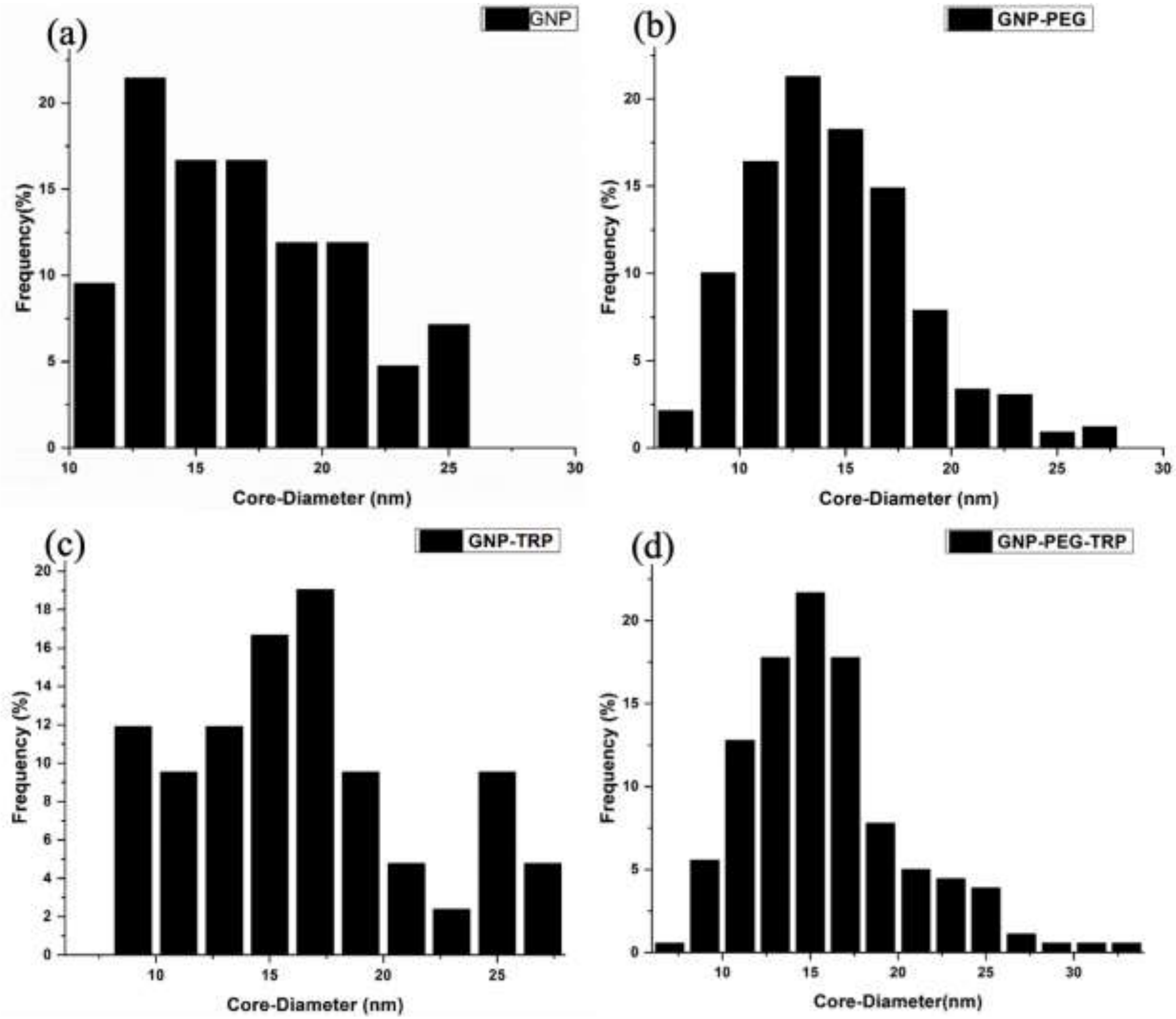

Fig. 3.5. (a) TEM core diameter distribution of GNP; (b) TEM core diameter distribution of GNP-PEG; (c) TEM core diameter distribution of GNP-TRP; (d) TEM core diameter distribution of GNP-PEG-TRP.

The colloidal stability of the biosynthesized gold nanoparticles systems (GNP, GNP-TRP, GNP-PEG, GNP-PEG-TRP) in water were characterized using Dynamic light scattering (DLS) analysis over a 6-month period. Table 3.2 summarizes the PDI and Zeta potential values after 1-month, 3-months and 6-months of synthesis. An increase in the hydrodynamic diameter (D) of the GNP, GNP-PEG, GNP-TRP, GNP-PEG-TRP was observed over time and their PDI's range between 0.2

and 0.3. Zeta potential values of GNP, GNP-TRP and GNP-PEG-TRP show no consistent trend but+ GNP-PEG values remained below -25 mV ($\xi < -25$ mV).

Table 3.2 Six (6) month Summary of DLS and Zetasizer measurements showing hydrodynamic diameter (d), polydispersity index (PDI) and Zeta potential (ξ) values for GNP, GNP-TRP, GNP-PEG, GNP-PEG-TRP in Distilled water (Di-water).

			DI-Water			
		GNP		GNP-TRP		
Month	d (nm)	PDI	ξ (mv)	d (nm)	PDI	ξ (mv)
1	77.8±2.8	0.33±0.01	-23.2±2.7	155.3±3.4	0.23±0.01	-25.1±2.7
3	88.9±5.1	0.41±0.05	-22.3 ±0.7	160.9±2.8	0.28±0.04	-20.4±1.0
6	98.4±11.3	0.36±0.03	-21.7±0.2	168.4±1.5	0.27±0.03	-25.6±1.0
		GNP-PEG		GNP-PEG-TRP		
Month	d (nm)	PDI	ξ (mv)	d (nm)	PDI	ξ (mv)
1	62.3±1.3	0.26±0.01	-29.7±1.7	72.2±0.4	0.25±0.04	-29.1±2.0
3	63.9±1.4	0.27±0.03	-28.2±3.8	88.2±0.9	0.26±0.04	-20.5±0.4
6	67.8±0.5	0.32±0.04	-30.0±1.7	90.8±0.9	0.32±0.01	-19.5±0.9

A plot of the percentage alamar blue reduction at different durations is presented in Fig. 3.6. This shows that the incubation of normal breast cells with GNP, GNP-TRP, GNP-PEG, GNP-PEG and GNP-PEG-TRP at a concentration of 5 µg/mL for 72 h had negligible to minimal toxicity effects on the normal breast cells. As shown in Fig. 3.6, there were significant successive increases in cell proliferation, as measured by the increased % alamar blue reduction values, as the exposure duration of cells with the GNP systems increased ($p < 0.001$). After 24 hours of exposure of the

MCF-10A breast cells to the different GNP nanoparticle systems, there were no significant differences in the cell viabilities (% alamar blue reduction) between the untreated cells and the cells treated with the GNP systems ($p > 0.05$). In contrast, there were significant differences between the GNP-TRP- and GNP-PEG-treated cells after 24 hours of treatment ($p = 0.035$). However, no significant differences were observed among the GNP-treatment groups and between them and the untreated cells 48- and 72-hours post-treatment ($p > 0.05$). This suggests that exposure to the different GNP systems did not significantly affect the MCF-10A breast cells' viability and proliferation.

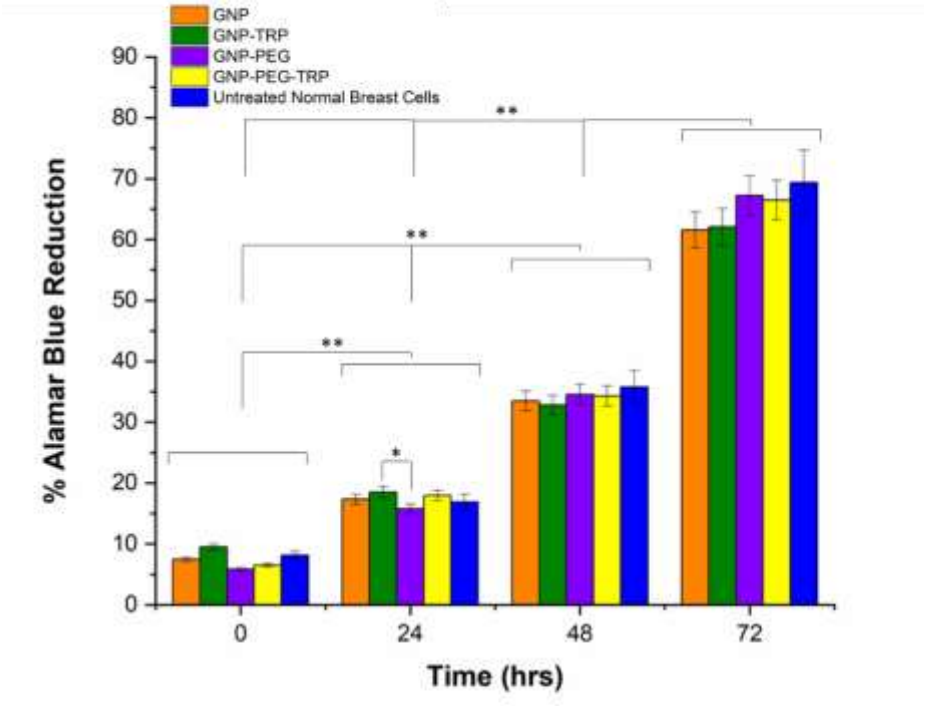

Fig. 3.6. Percentage of alamar blue reduction for untreated normal breast cells and normal breast cells treated with GNP, GNP-TRP, GNP-PEG, and GNP-PEG-TRP. The error bars represent the standard deviations for $n = 3$ measurements. * $p < 0.05$; ** $p < 0.001$

The FTIR spectra for the cell free extract (CFE), Triptorelin (TRP) ligand, GNP, GNP-PEG, GNP-TRP, GNP-PEG-TRP were obtained from wavelength of 400 - 4000 cm^{-1} and shown in Fig. 3.7 The FTIR bands of CFE reveal the presence of carbonyl (aldehyde groups) at 1741 and 1835 cm^{-1}. C-H groups are also present at 2931 cm^{-1}. The GNP spectra showed peaks for carbonyl groups (1835, 1741 and 1692 cm^{-1}) which are also present in the CFE.

The GNP-PEG spectra show carboxylic group peaks at 3360 cm^{-1} for the OH group and C=O peaks at 1710 and 1641 cm^{-1}. In the GNP-TRP spectra, amine functional group peaks (N-H) that were present in the TRP ligand spectra at 1515, 1635 and 3200-3600 cm^{-1} as well as the carbonyl group peaks (C=O) that were present in the GNP spectra were absent, while the FTIR spectra of GNP-PEG-TRP showed the presence of the primary amide bond (C=O at 1692 cm^{-1} and N-H group at 3421 and 3481 cm^{-1}).

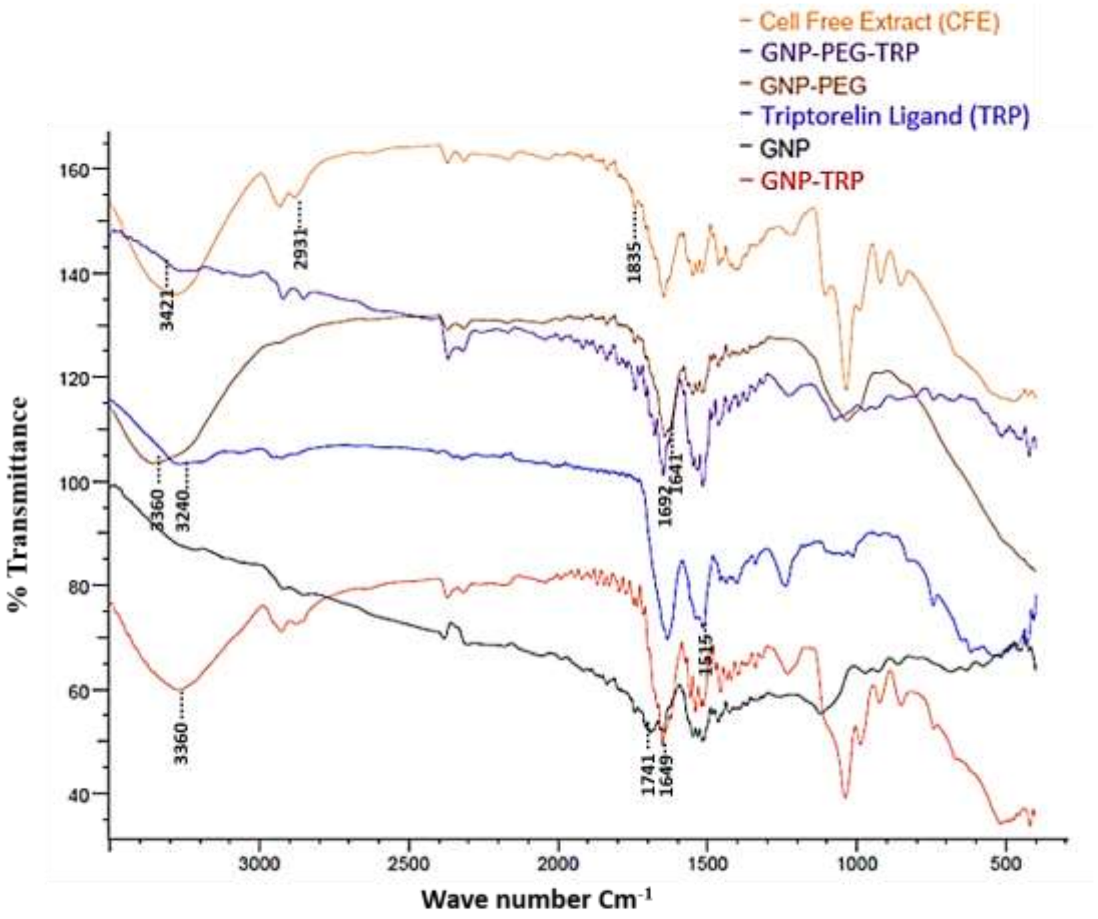

Fig. 3.7. FTIR spectra of cell free extract, GNP-PEG-TRP, GNP-PEG, Triptorelin, GNP-TRP and GNP.

3.5.2. Adhesion Forces

The measured adhesion forces for six different AFM tip/cell configurations are presented in Fig. 3.8. There were statistically significant differences ($p < 0.001$) in the adhesion forces between the different cell types (MCF-10A, MDA-MB-231, and MDA-MB-468) and the different AFM tip coating configurations (bare tip, TRP, GNP, GNP-PEG, GNP-TRP, and GNP-PEG-TRP). The control (bare AFM tip/cell) shows that the adhesion force between the bare AFM tip and MCF-10A normal breast cells is 22.9 ± 4.8 nN. The adhesion forces were greater for the MDA-MB-231 cells than the MCF-10A ($p < 0.001$) and the MDA-MB-468 cells ($p = 0.001$), but no differences existed between the MDA-MB-468 and the MCF-10A cells ($p = 0.719$) for the bare tip configuration.

Generally, coating the AFM tip with GNP increased the adhesion force between the tip and the different cell lines ($p < 0.001$) compared to the bare tip. Further successive increases in adhesion force were observed when the AFM tips were coated with GNP-PEG ($p < 0.001$), GNP-PEG-TRP ($p < 0.001$), GNP-TRP ($p < 0.001$) and TRP ($p < 0.001$), although there were no significant differences between TRP and GNP-TRP ($p = 0.951$). For the different cell types, the adhesion forces between the MDA-MB-231 cells and the different coated AFM tips were greater than those of the MDA-MB-468 cells ($p < 0.001$) and the MCF-10A cells ($p < 0.001$). The adhesion forces for the MDA-MB-468 cells were also higher than for the MCF-10A cells ($p < 0.001$).

The highest adhesion force measured was observed between the TRP-coated AFM tips and the TNBC cells. This was consistent for both TNBC cells. In the MDA-MB-231 cell line, the TRP-coated AFM tip interactions were about nine times (230 ± 58.4 nN) the adhesive interaction between the TRP-coated AFM tip and normal breast cell (26.1 ± 12.5 nN), while the MDA-MB-468 cell interaction with the TRP-coated AFM tip was about seven times (175.5 ± 60.6 nN) the adhesive interaction between the TRP/ normal breast cell pair (26.1 ± 12.5 nN). A similar nine-fold and three-fold increase in adhesion force was observed between GNP-TRP/TNBC and GNP-PEG-TRP/TBNC pairs respectively.

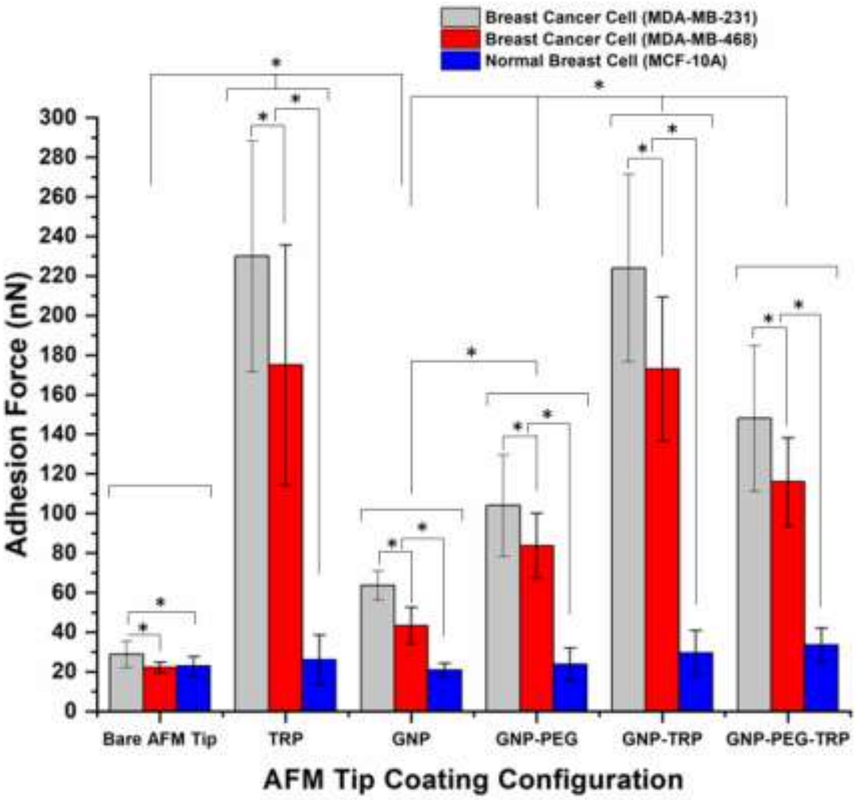

Fig. 3.8. Summary of the adhesion forces between different AFM tip/cell combinations. The error bars represent the standard deviations for n = 100 measurements. * $p < 0.001$

Confocal microscopy results in Fig. 3.9 show blue DAPI-stained nuclei and green labeled LHRH receptors of normal breast (MCF10A) and TNBC (MDA-MB-231) cells. The results reveal an overexpression of LHRH receptors on the surface of MDA-MB-231 and MDA-MB-468 breast cancer cell. This overexpression of the receptors is considered to be the reason for the increase n the adhesive interactions between the LHRH ligands on the AFM tips and the LHRH receptors on the cells.

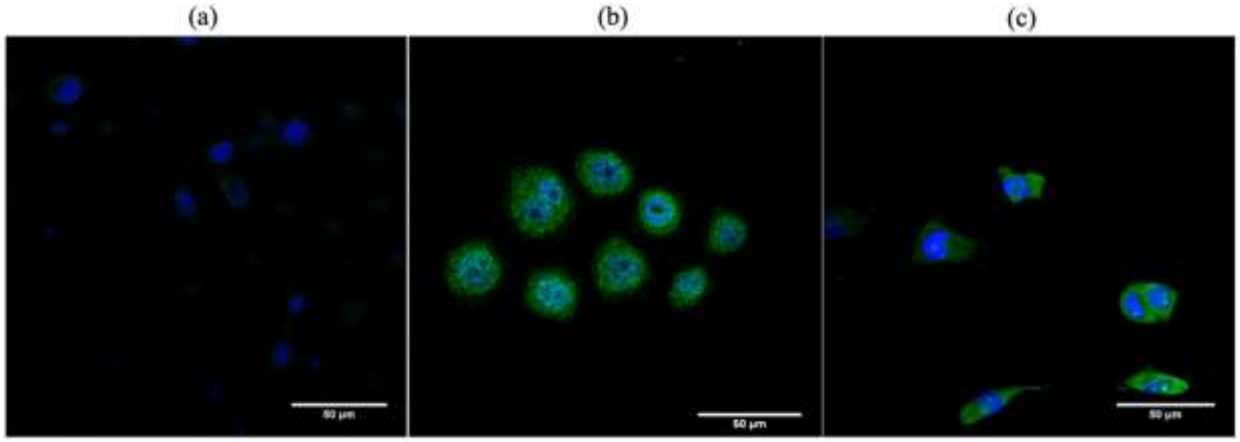

Fig. 3.9. Confocal fluorescent images of blue DAPI-stained nuclei and green labeled LHRH receptors of normal breast (MCF 10A) and TNBC (MDA-MB 231, MDA-MB-468) cells. (a) LHRH receptors expressed on MCF 10A cells (b) green overexpressed LHRH receptors on MDA- MB-468 cells (c) green overexpressed LHRH receptors on MDA-MB 231 cells.

3.6. Discussion

3.6.1. Nanoparticle Biosynthesis, PEGylation, Conjugation, and Characterization

TEM micrographs (Fig. 3.4) and nanoparticle core diameter histograms (Fig. 3.5), show that size distribution of the nanoparticles are within the same range after surface modifications of GNP with PEG and TRP [29].

The observed increase in absorbance values from GNP to GNP-PEG (~ 32%), GNP to GNP-TRP (~ 29%) and GNP to GNP-PEG-TRP (~ 25 %) and spectral redshift of maximum absorption wavelength is due to the changes in the nanoparticle sizes. This result is in agreement with prior studies where size related redshifts were observed because of length of synthesis time and PH variation [5], [18], [30]. In general, the observed maximum absorption wavelength falls within the 10-40 nm size range indicated by other nanoparticle characterization studies where size, shape and structure of the GNPs have been shown to affect the value of the maximum absorption wavelength [5], [30], [31].

The PDI's for all the nanoparticle systems (GNP, GNP-PEG, GNP-TRP and GNP-PEG-TRP) ranged between 0.2 and 0.3. Over the 6-month period, the PDI's of the nanoparticle systems in distilled water remained nearly monodisperse (0.1-0.3). This PDI value falls within the acceptable range for maximum ligand exchange, drug delivery and in-vivo applications [32].

The increase in the hydrodynamic diameter range from the TEM core diameter range is mostly due to contributions of the shell of hydration around the nanoparticles and nanoparticle clusters/aggregation formed as a result the increase in the zeta potential value ($\xi > -25$ mV). Since the DLS works by measuring the variations in scattered light intensity, these intensities are correlated to the hydrodynamic diameter of the particles using the Stokes–Einstein equation and a correlation function [33]. However, from Rayleigh theory, the intensity of scattered light is proportional to the sixth power of the diameter, thus the analysis is heavily tilted towards larger particle sizes while smaller particles are obscured [33].

GNP spectra showed peaks for carbonyl groups (1835, 1741 and 1692 cm^{-1}) present in the CFE. Similar study done using a macro-algae extract (Gracilaria Edulis) to synthesis silver and zinc nanoparticles also showed the present of carbonyls in the extract and on the surface of the biosynthesized nanoparticles [34].

The FTIR bands of CFE reveal the presence of carbonyl (aldehyde groups) and C-H groups commonly found in organic molecules [24], [35]. These carbonyl groups were also present in the GNP spectra and is indicative of the adsorbed proteins on the GNP surface due to the biosynthesis method used.

In the GNP-TRP spectra the amine group peaks (N-H) present in the TRP ligand spectra and carbonyl group peaks (C=O) present in the GNP spectra were absent. This is indicative of the formation of the C=N bonds at 1649 cm^{-1} found within the 1640-1690 cm^{-1} range [2], [35], [36]. Although carbonyls are reactive to primary amines, these interactions do not produce strong stable bonds and require further amination processes [24][25]. The carboxylic group peaks at 3360 cm^{-1} OH group and C=O peaks at 1710 and 1641 cm^{-1} seen in GNP-PEG FTIR bands, confirms the PEGylation process of the GNP with a carboxyl terminated polyethylene glycol. The absence of the Carboxylic acid group in the GNP-PEG-TRP spectra and the presence of the primary amide bond (C=O at 1692 cm^{-1} and N-H group at 3421 and 3481 cm^{-1}) confirms that the carbodiimide conjugation process between the carboxyl and primary amine group using EDC/NHS catalyst occurred [3], [37].

3.6.2. Adhesion Forces

Specific targeting requires that the adhesive interaction between functionalized nanoparticles and triple negative breast cancer cells be strong and selective, hence this section discusses trends observed from experimental AFM adhesion measurements between AFM tip coatings (GNP, GNP-PEG, GNP-TRP and GNP-PEG-TRP) and breast cells (TNBC and normal breast cell).

The preferential adhesion of TRP modified nanoparticles to TNBC is very evident from the results in Fig. 3.8 and this preferential interaction has also been reported in prior experiments [3], [5] with other types of nanoparticles. The significant increase in the average adhesion forces obtained between the TRP/TNBC, GNP-TRP/TNBC and GNP-PEG-TRP/TNBC is attributed to the over-expression of LHRH transmembrane receptors on the surfaces of the TNBC [3], [5],[6]. This was revealed (Fig. 3.9) by the immunofluorescence staining of LHRH receptors on normal (MCF10A) breast cells and TNBC cells (MDA-MB-231 and MDA-MB-468). This over expression of LHRH receptors in TNBC results in increased binding interactions, between the TRP/TNBC, GNP-TRP/TNBC and GNP-PEG-TRP/TNBC pairs.

It is important to note here that large standard deviations were observed in measured average adhesion forces, especially between AFM tip coatings with TRP. These are attributed to significant local variations between the local densities of the LHRH transmembrane receptors. Similar variations in the adhesion forces have been reported in prior AFM studies of adhesion [4]–[6].

UV-Vis analysis done in a prior study by the group [5] showed the presence of surface bound proteins on biosynthesized nanoparticles which contribute to the overall adhesion of GNP to TNBC even when these proteins are denatured by SDS [5]. Polymer extension effects also occur upon retraction if multiple polymer molecules attach to AFM tip and substrate [38]. This extension effect is typically observed as sawtooth pattern on the retraction force-distance curve [38]. Hence, additional force is needed to detach GNP-PEG coated AFM tips from TNBC cells. This leads to an increase in the adhesion force measured in the pair interactions of GNP/Cell and GNP-PEG/Cell (Fig. 3.8)

Finally, comparing the average adhesion forces measured between GNP-TRP/MDA-MB-231 breast cancer cell (224 ± 47.4 nN), and the interaction between GNP-TRP/ MDA-MB-468 breast cancer cell (173 ± 36.7 nN). The adhesion forces between the MDA-MB-231 cells and the different coated AFM tips were greater than those of the MDA-MB-468 cells ($p < 0.001$) and the MCF-10A cells ($p < 0.001$) while MDA-MB-468 cells adhesion forces were higher than the adhesion forces in MCF-10A cells ($p < 0.001$). The higher adhesion forces obtained for the MDA-MB-231cell line suggest an increase in the ligand interact with overexpressed receptor density. It is important to note that the magnitude of adhesion force can be modulated by varying triptorelin concentration and density on the surface of the nanoparticles [2]. The process of PEGylation introduces methyl group spacers with arm length 15.8Å. Qualitatively, these PEG spacers reduce the total surface area available for triptorelin conjugation via the carboxyl terminated PEG (PEG_{12}) and this contributes to the reduction in adhesion observed experimentally in Fig. 3.8 for GNP-PEG-TRP/TNBC as against GNP-TRP/TNBC.

It is also of interest to discuss the potential role that water vapor (in the environment) can have on the measured adhesion forces. In the most extreme case in which capillary forces are caused by a liquid film idealization, as shown schematically in Fig 3.2., the maximum capillary forces can be estimated from the theory presented in section 3.2. using surface tension of water at 21°C ($72.8 \times 10^{-3}\ \mathrm{N}/\mathrm{m}$)[39], and an estimated AFM tip radius of curvature of (48.9nm). The maximum capillary force estimated (equation 3.6) is 44.7 nN. For D/d ratio between 0.25 – 1, such capillary forces range from 35.8-22.4 nN. These capillary forces are comparable to the measured adhesive interactions in the absence of TRP ligand interactions (Fig 3.8) and overexpressed LHRH receptors on MCF-10a cells (Fig.3.9). However, they are much lower than the measured adhesion forces of 230 ± 58.4 nN and 175 ± 60.6 nN that were obtained from interactions between TRP ligand coated AFM tips TNBC cells with overexpressed LHRH receptors. Thus, we conclude that the very high adhesion forces observed in these cases can be attributed largely to specific interactions between TRP ligands and multiple LHRH receptors.

Results from a molecular dynamics simulation which explored the molecular origins of adhesive interactions observed in the AFM experiments report that the intermolecular interactions between LHRH receptors and TRP ligands was dominated by electrostatic and hydrogen bond energies[40].

In addition, it reported variations in the energy interactions with TRP across the transmembrane LHRH receptors[40].This variation in interaction energy is due to the individual characteristics of the receptor-ligand docking points and the conformation of the molecules when in their minimum energy state[40].

3.6.3. Implications

The implications of the above results are significant for the design of gold nanoparticles for the specific targeting and treatment of TNBC. First, the increased adhesion forces that are associated with the interactions between TRP and the receptors on the TNBC cells suggest that such forces can be used to enable the selective attachment of TRP-conjugated PEG coated gold nanoparticles to TNBC cells/tissues. Similar enhancements in adhesion forces have also been observed between TRP-conjugated magnetite nanoparticles to over-expressed LHRH receptors on the surfaces of TNBC cells.

Furthermore, in normal breast cells with limited LHRH receptor expression (Fig. 3.8), adhesion interactions with AFM tip coatings (TRP, GNP-TRP, GNP-PEG, GNP-PEG-TRP) are much lower than the magnitude of adhesion forces (Fig. 3.8) between TBNC cells and the same AFM tip coatings.

In any case, this study suggests that force spectroscopy can be used as a tool for rapid screening of potential targets that can be used for the specific targeting of TNBC. The study also provides a fundamental basis for the design of Triptorelin functionalized PEG coated gold nanoparticles for specific targeting of triple negative breast cancer cells, with potential for photothermal treatment of near surface tumors. However, further work is needed to demonstrate the effectiveness of such specific targeting, and the photothermal treatment of TNBC. These are clearly some of the challenges for future work.

3.7. Conclusions

This paper presents the results of an experimental study of the the adhesion between TNBC/normal breast cells and biosynthesized gold nanoparticles in (GNP), PEG-coated gold nanoparticles (GNP-PEG), and its Triptorelin functionalized forms (GNP-TRP, GNP-PEG-TRP). These were studied using atomic force microscopy. The salient conclusions arising from this study are summarized below.

1. Force microscopy measurements of the adhesion forces between TNBC cells and Triptorelin-functionalized gold nanoparticles (GNP-TRP and GNP-PEG-TRP) are much greater than the adhesion to normal breast cells. The increased adhesion of GNP-TRP and GNP-PEG-TRP to TNBC is also associated with the over-expression of LHRH receptors on the surfaces of TNBC cells. This enhances the selective adhesion of LHRH-conjugated gold nanoparticles to TNBC cells.
2. The PEG coating of biosynthesized gold nanoparticles reduces non-specific nanoparticle/cell interactions. It also has a favorable effect on the adhesion between GNP-PEG-TRP/ LHRH TMD-n receptors pairs. The repulsive interaction between the Triptorelin ligand/ cell membrane and PEG/cell membrane promotes specificity of the GNP-PEG-TRP/ LHRH TMD-n receptors interactions in TNBC. Therefore, the current results suggest that GNP-PEG-TRP nanoparticles could be suitable candidates for the specific targeting of TNBC cells that have over-expressed LHRH receptors on their surfaces.

3.8. References

[1] D. Rosenblum, N. Joshi, W. Tao, J. M. Karp, and D. Peer, “Progress and challenges towards targeted delivery of cancer therapeutics,” *Nat. Commun.*, vol. 9, no. 1, 2018.

[2] J. Hu, S. Youssefian, J. Obayemi, K. Malatesta, N. Rahbar, and W. Soboyejo, “Investigation of adhesive interactions in the specific targeting of Triptorelin-conjugated PEG-coated magnetite nanoparticles to breast cancer cells,” *Acta Biomater.*, vol. 71, no. February, pp. 363–378, 2018.

[3] J. D. Obayemi *et al.*, “Adhesion of ligand-conjugated biosynthesized magnetite nanoparticles to triple negative breast cancer cells,” *J. Mech. Behav. Biomed. Mater.*, vol. 68, no. January, pp. 276–286, Apr. 2017.

[4] Y. Oni *et al.*, “Gold nanoparticles for cancer detection and treatment: The role of adhesion,” *J. Appl. Phisics*, vol. 115, no. 084305, pp. 1–9, 2014.

[5] E. Hampp, R. Botah, O. Odusanya, N. Anuku, K. Malatesta, and W. Soboyejo, “Biosynthesis and adhesion of gold nanoparticles for breast cancer detection and treatment,” *J. Mater. Res.*, vol. 27, no. 22, pp. 2891–2901, 2012.

[6] J. Meng, E. Paetzell, a. Bogorad, and W. O. Soboyejo, “Adhesion between peptides/antibodies and breast cancer cells,” *J. Appl. Phys.*, vol. 107, no. 11, p. 114301, 2010.

[7] J. D. Obayemi *et al.*, “LHRH-Conjugated Drugs as Targeted Therapeutic Agents for the Specific Targeting and Localized Treatment of Triple Negative Breast Cancer,” *Sci. Rep.*, 2020.

[8] J. Hu, J. Obayemi, K. Malatesta, E. Yurkow, D. Adler, and W. Soboyejo, “Luteinizing hormone-releasing hormone (LHRH) conjugated magnetite nanoparticles as MRI contrast agents for breast cancer imaging,” *Appl. Sci.*, 2020.

[9] K. Kan-Dapaah, N. Rahbar, A. Tahlil, D. Crosson, N. Yao, and W. Soboyejo, “Mechanical and hyperthermic properties of magnetic nanocomposites for biomedical applications,” *J. Mech. Behav. Biomed. Mater.*, vol. 49, no. April, pp. 118–128, 2015.

[10] K. Kan-Dapaah, N. Rahbar, and W. Soboyejo, “Implantable magnetic nanocomposites for the localized treatment of breast cancer,” *J. Appl. Phys.*, 2014.

[11] J. F. Hainfeld, L. Lin, D. N. Slatkin, F. Avraham Dilmanian, T. M. Vadas, and H. M. Smilowitz, “Gold nanoparticle hyperthermia reduces radiotherapy dose,” *Nanomedicine Nanotechnology, Biol. Med.*, vol. 10, no. 8, pp. 1609–1617, 2014.

[12] J. Lee, D. K. Chatterjee, M. H. Lee, and S. Krishnan, “Gold nanoparticles in breast cancer treatment: Promise and potential pitfalls,” *Cancer Letters*, vol. 347, no. 1. pp. 46–53, 2014.

[13] J. Beik *et al.*, “Gold nanoparticles in combinatorial cancer therapy strategies,” *Coord. Chem. Rev.*, vol. 387, pp. 299–324, 2019.

[14] J. Peng, X. Liang, and L. Calderon, “Progress in research on gold nanoparticles in cancer management,” *Med. (United States)*, vol. 98, no. 18, 2019.

[15] X. Huang, P. K. Jain, I. H. El-Sayed, and M. A. El-Sayed, “Plasmonic photothermal therapy (PPTT) using gold nanoparticles,” *Lasers Med. Sci.*, vol. 23, no. 3, pp. 217–228, 2008.

[16] D. P. O’Neal, L. R. Hirsch, N. J. Halas, J. D. Payne, and J. L. West, “Photo-thermal tumor ablation in mice using near infrared-absorbing nanoparticles,” *Cancer Lett.*, vol. 209, no. 2, pp. 171–176, 2004.

[17] E. S. Day, J. G. Morton, and J. L. West, “Nanoparticles for thermal cancer therapy,” *J. Biomech. Eng.*, vol. 131, no. 7, pp. 1–5, 2009.

[18] S. . Dozie-Nwachukwu *et al.*, “Biosynthesis of Gold Nanoparticles with Serratia marcescens Bacteria,” *Adv. Mater. Res.*, vol. 1132, no. 19, pp. 19–35, 2016.

[19] S. O. Dozie-Nwachukwu *et al.*, “Biosynthesis of Gold Nanoparticles from *Nauclea latifolia* Leaves,” *Adv. Mater. Res.*, vol. 1132, pp. 36–50, 2015.

[20] J. Drelich, *Atomic Force Microscopy in Adhesion Studies*. CRC Press, 2005.

[21] G. Thomas, N. A. Burnham, T. A. Camesano, and Q. Wen, “Measuring the Mechanical Properties of Living Cells Using Atomic Force Microscopy,” *J. Vis. Exp.*, 2013.

[22] E. L. Bentzen *et al.*, “Surface modification to reduce nonspecific binding of quantum dots in live cell assays,” *Bioconjug. Chem.*, vol. 16, no. 6, pp. 1488–1494, 2005.

[23] M. Zheng, F. Davidson, and X. Huang, “Ethylene glycol monolayer protected nanoparticles for eliminating nonspecific binding with biological molecules,” *J. Am. Chem. Soc.*, vol. 125, no. 26, pp. 7790–7791, 2003.

[24] G. T. Hermanson, *Bioconjugate Techniques: Third Edition*. 2013.

[25] Thermo, “Thermo Scientific Pierce Crosslinking Technical Handbook,” *Ebooks*, 2009.

[26] K. V. Wolf *et al.*, “An investigation of adhesion in drug-eluting stent layers,” *J. Biomed. Mater. Res. - Part A*, 2008.

[27] J. Hu, J. D. Obayemi, K. Malatesta, A. Košmrlj, and W. O. Soboyejo, “Enhanced cellular uptake of LHRH-conjugated PEG-coated magnetite nanoparticles for specific targeting of triple negative breast cancer cells,” *Mater. Sci. Eng. C*, vol. 88, no. July 2017, pp. 32–45, 2018.

[28] E. M. Czekanska, “Assessment of cell proliferation with resazurin-based fluorescent dye.,” *Methods Mol. Biol.*, 2011.

[29] J. Meng *et al.*, “LHRH-functionalized superparamagnetic iron oxide nanoparticles for breast cancer targeting and contrast enhancement in MRI,” *Mater. Sci. Eng. C*, vol. 29, no.

4, pp. 1467–1479, 2009.

[30] P. N. Njoki *et al.*, “Size correlation of optical and spectroscopic properties for gold nanoparticles,” *J. Phys. Chem. C*, vol. 111, no. 40, pp. 14664–14669, 2007.

[31] J. Gao, X. Huang, H. Liu, F. Zan, and J. Ren, “Colloidal stability of gold nanoparticles modified with thiol compounds: bioconjugation and application in cancer cell imaging.,” *Langmuir*, vol. 28, no. 9, pp. 4464–71, 2012.

[32] M. Danaei *et al.*, “Impact of particle size and polydispersity index on the clinical applications of lipidic nanocarrier systems,” *Pharmaceutics*, vol. 10, no. 2, pp. 1–17, 2018.

[33] C. M. Maguire, M. Rösslein, P. Wick, and A. Prina-Mello, “Characterisation of particles in solution–a perspective on light scattering and comparative technologies,” *Science and Technology of Advanced Materials*. 2018.

[34] R. I. Priyadharshini, G. Prasannaraj, N. Geetha, and P. Venkatachalam, “Microwave-Mediated Extracellular Synthesis of Metallic Silver and Zinc Oxide Nanoparticles Using Macro-Algae (Gracilaria edulis) Extracts and Its Anticancer Activity Against Human PC3 Cell Lines,” *Appl. Biochem. Biotechnol.*, vol. 174, no. 8, pp. 2777–2790, 2014.

[35] J. L. G. Wade, *Organic chemistry*, 7th ed., vol. 250, no. 4. 2010.

[36] C. LibreTexts, “Infrared Spectroscopy Absorption Table,” 2019. [Online]. Available: https://chem.libretexts.org/Bookshelves/Ancillary_Materials/Reference/Reference_Tables/Spectroscopic_Parameters/Infrared_Spectroscopy_Absorption_Table.

[37] J. D. Obayemi *et al.*, “Biosynthesis and the conjugation of magnetite nanoparticles with luteinizing hormone releasing hormone (LHRH).,” *Mater. Sci. Eng. C. Mater. Biol. Appl.*, vol. 46C, pp. 482–496, 2015.

[38] W. F. Heinz and J. H. Hoh, “Spatially resolved force spectroscopy of biological surfaces using the atomic force microscope,” *Trends in Biotechnology*, vol. 17, no. 4. pp. 143–150, 1999.

[39] N. B. Vargaftik, B. N. Volkov, and L. D. Voljak, “International Tables of the Surface Tension of Water,” *J. Phys. Chem. Ref. Data*, vol. 12, no. 3, pp. 817–820, 1983.

[40] V. O. Uzonwanne *et al.*, “Triptorelin-functionalized PEG-coated biosynthesized gold nanoparticles: Effects of receptor-ligand interactions on adhesion to triple negative breast cancer cells,” *Biomater. Adv.*, p. 212801, Apr. 2022.

Chapter 4.0. Entry of Triptorelin and PEG-coated Gold Nanoparticles into Triple Negative Breast Cells: Effects of Surface Energy and Receptor Density on Nanoparticle Uptake

4.1. Introduction

Cancer therapeutics has seen an increase in treatment response rates among breast cancer patients. Various clinical and pathological studies report that triple negative breast cancer (TNBC) patients, especially those with residual or metastatic TNBC, have a significantly decreased disease-free survival (DFS) rate and overall survival (OS) rate compared to other breast cancer subtypes [1]–[10]. Unfortunately, over 50% of TNBC patients do not benefit from the available endocrine chemotherapy treatments because it does not overexpress any of the three primary breast tumor markers: progesterone, estrogen, and human epidermal growth factor 2 (HER2) [1], [2], [11], [3]–[10]. Hence, TNBC progression is aggressive with a poor prognosis.

Therefore, the need to improve the DFS and OS of TNBC patients drives cancer research efforts toward targeted therapeutic approaches for TNBC [1], [2], [16]–[20], [5]–[8], [12]–[15]. Current TNBC targeted therapeutic studies have focused on designing small interfering molecules to interact with genetic pathways that arrest TNBC cell lifecycle at different checkpoints or boost the immune response of TNBC patients to induce apoptosis [3], [5], [6], [8], [12]–[15], [21].

Most targeted nanoparticles have been designed to mimic viruses, which have surface proteins that can interact with specific receptors that are overexpressed on the surfaces of biological cells [22]–[24].

Hence, recent targeted cancer treatment studies have focused on the design of theranostic ligand functionalized nanoparticles to target proteins and receptors that are overexpressed on the surfaces of TNBC cells [18]–[20], [25], [26]. These ligand functionalized nanoparticles rely on the receptor-mediated uptake of nanoparticles into biological cells to enhance TNBC selectivity[22], [27]–[32].

Receptor-ligand interactions are essential to targeted TNBC treatment because it is one of the entry pathways for biological cells to internalize food, viruses, and nanoparticles [23], [27], [33].

Various theoretical, computational, and experimental studies on targeted nano-drug delivery systems identify particle size, ligand density, and receptor density as limiting factors to the efficient uptake of these nanostructures[22], [30]–[32], [34]–[39]. For instance, earlier models on the budding of viruses on a host cell membrane focused on the uptake conditions for a single nanoparticle size [34], [40], [41]. Subsequently, Refs. [27][22] introduced receptor diffusive models to estimate the nanoparticle wrapping time for a range of particles sizes. Despite experimental evidence [28], [29], which shows that nanoparticle clusters can also be internalized by cells. These nanoparticle entry models are based on assumptions of single-particle entry. Hence, the nanoparticle cluster effect on cluster uptake has not been investigated for various nanoparticles developed for therapeutic applications.

Prior efforts by our research group have explored thermodynamic-kinetic models that include surface energy effects on the free energy function associated with nanoparticle wrapping[28], [42]. In these studies, we unraveled new insights into the influence of receptor density, ligand density, and surface energy on the entry of Luteinizing Hormone Releasing Hormone (LHRH) conjugated superparamagnetic iron oxide nanoparticles (SPION) in human breast cancer Hs 578T [28] and LHRH conjugated Magnetite nanoparticles in non-tumorigenic breast cell (MCF 10A) and tumorigenic TNBC (MDA-MB-231). Magnetite nanoparticles were used in those studies due to their ability to enhance the contrast of magnetic resonance imaging (MRI) [43], as well as their ability to induce hyperthermic heating associated with oscillating magnetic fields[44], [45].

In this article, we present a modified thermodynamic-kinetic model to explore the effects of ligand density, receptor density, nanoparticle cluster size, and surface energy effects on the wrapping time of ligand-functionalized gold nanoparticles of various sizes, and also present results from invitro nanoparticle cluster distribution and uptake of biosynthesized gold nanoparticles (GNP), PEG-coated GNP (GNP-PEG), Triptorelin (TRP)-functionalized GNP (GNP-TRP), and Triptorelin (TRP)-functionalized PEG-coated GNP (GNP-PEG-TRP) in TNBC cells (MDA-MB-231 and MDA-MB-468) and non-tumorigenic cell line (MCF 10A).

Within this context, a fundamental understanding of the wrapping kinetics and driving forces associated with the entry of functionalized GNP in MDA-MB-231, MDA-MB-468, and non-tumorigenic breast cells (MCF 10A) could provide a physical basis for the design of GNP structures with controlled targeted and cell uptake characteristics for TNBC treatment.

Finally, the implications of the results are discussed for the design of triptorelin-conjugated, PEG-coated biosynthesized gold nanoparticles for specific targeting of triple-negative breast cancer cells and localized laser-assisted photothermal treatment.

4.2. Materials and Experimental Methods

4.2.1. Gold Nanoparticles Synthesis and Characterization

The gold nanoparticles (GNP) were synthesized from processes adapted from a prior study done by our group[46]. Briefly, Gold (III) Chloride Trihydrate (ACS reagent with ≥49.0% Au basis Sigma-Aldrich, St. Louis, USA) was reduced intracellularly and extracellularly using a cell-free extract of Serratia Marcescens bacteria [46].

Subsequently, GNP was PEG-coated using methyl-PEG$_4$-thiol (MT(PEG)$_4$) and carboxy-PEG$_{12}$-thiol (CT(PEG)$_{12}$) (Thermo Fisher Scientific, Inc. Waltham, MA, USA). Notably, (MT(PEG)$_4$) and (CT(PEG)$_{12}$) were used in combination to reduce nonspecific protein binding to the nanoparticle surface [47], [48]. A solution of MT(PEG)$_4$ (0.5 mM, 4 mL) and CT(PEG)$_{12}$ (0.5 mM, 4 mL) were added to 10 mL of GNP (0.2 mM) and stirred for 2 h at room temperature.Next, the mixture was washed with Dulbecco Phosphate Buffer Saline (DPBS) (Life technologies cooperation, Carlsbad, CA) buffer and centrifuged in a spin column with a molecular weight cut-off of 50 kDa. Lastly, the PEG-coated GNPs were resuspended in de-ionized water.

The bare GNP and PEG-coated GNP (GNP-PEG) were modified by the ligand conjugation with triptorelin (D-Trp LHRH)(BACHEM, Torrance, CA, USA) using a carbodiimide activation process with ethyl (dimethyl aminopropyl) carbodiimide (EDC) (Sigma-Aldrich, St. Louis, MO, USA) and N-hydroxysuccinimide (NHS) (Thermo Fisher Scientific, Inc., Waltham, MA, USA)[49][50]. Specifically, a solution of EDC (13.5 mM, 74µL) and NHS (15.3 mM, 65 µL) was added to GNP and GNP-PEG (0.2 mM, 5 mL) and stirred continuously for 2 hours at room temperature before triptorelin ligand (TRP) (5 mM, 192 µL) was added and stirred overnight. After TRP conjugation of GNP (GNP-TRP) and PEG-coated GNP(GNP-PEG-TRP), the mixture was washed with DPBS, then centrifuged in a spin column with a molecular weight cut-off of 50 kDa. Lastly, GNP-TRP and GNP-PEG-TRP were resuspended in de-ionized water.

Finally, the colloidal stability of GNP, GNP-TRP, GNP-PEG, and GNP-PEG-TRP in distilled water was investigated for six months by measuring the hydrodynamic diameter and zeta potentials using the Malvern Zetasizer (Westborough, MA, USA).

4.2.2. In-vitro Uptake of Gold Nanoparticles into TNBC Cells and Normal Breast Cells

All the cell lines used in this study were procured from ATCC, Manassas, Virginia, USA, and a detailed description of the cell culture process has been documented in earlier studies done by our group [17], [19], [20]. Briefly, 1 x 10^6 cells/ml of TNBC cells (MDA-MB-231, MDA-MB-468) and non-tumorigenic MCF-10A cells was prepared. Subsequently, 10 µL of each prepared cell line were grown on 22 x 22 mm sterile uncoated coverslips inside 35 x10 mm sterile Falcon cell culture Petri dishes and incubated.

Specifically. the TNBC cells were incubated at 37°C under normal atmospheric pressure, while the normal breast cells (MCF-10A) were incubated at 37°C with 5% CO_2 in their respective media [17]. In addition, the GNP, GNP-TRP, GNP-PEG, and GNP-PEG-TRP particles were sterilized in 20 ml scintillation glass vials under Ultra-violet rays for 2h in a purifier class II biosafety cabinet (Labconco, MO, USA).

After 48 h, the culture medium from the cultured cells was aspirated and washed with DPBS. Next, 5µl of GNP, GNP-TRP, GNP-PEG, and GNP-PEG-TRP at 5 µg/mL was pipetted onto the coverslips containing normal breast cells (MCF-10A) and breast cancer cells (MDA-MB-231 and MDA-MB-468). Subsequently, 500 µl of the respective cell culture media was added to the cells and colloidal nanoparticles. The cell/nanoparticle mixtures were then placed in an incubator (model 3326, Forma Scientific, Inc. OH, U.S.A) at 5min, 30 min, 1h, and 3h incubation times. Subsequently, cell/nanoparticle samples were fixed in 4% Paraformaldehyde prepared in 0.1M phosphate Buffer Saline (PBS) (Electron Microscopy Sciences, Hatfield, PA, USA) for 12 min at room temperature (25°C).

4.2.2.1. Immunofluorescence Staining for LHRH Receptors

The distribution of LHRH receptors and nanoparticle attachment on the surfaces of MDA-MB-231, MDA-MB-468, and MCF-10A cells were revealed using immunofluorescence staining with fluorescent dyes. A detailed description of the cell receptor staining process has been documented in earlier studies done by our group [17], [19], [20]. In brief, the cells were cultured and grown for 48 h. Subsequently, these cells were fixed for 12 mins in a 4% high-grade paraformaldehyde solution to preserve their structures, permeabilized with 0.1% solution of Triton X-100 (Life Technologies Corporation, Carlsbad, CA), and blocked with 1% bovine serum albumin (BSA) (Sigma- Aldrich, St. Louis, M, USA),

Subsequently, the cell samples were labeled with a primary anti-LHRH antibody (EMD Millipore, Darmstadt, Germany) and a secondary anti-mouse IgG antibody conjugated with Alexa fluor 488 (Thermo Fisher Scientific, Inc., Waltham, MA, USA). Next, the nuclei of the cell samples were stained with 4’,6-Diamidino-2-Phenylindole, Dihydrochloride (DAPI) (Sigma-Aldrich, St. Louis, USA). Finally, 3D Z-stack confocal microscopy images of the internalized nanoparticles within the immunofluorescently stained cells were imaged with a 40x oil-immersion objective using the Leica TCS SP5 Scanning Confocal Microscope (Leica, Wetzlar, Germany).

4.3. Theory and Model

4.3.1. Single Particle Entry Model

Receptor-mediated particle entry in cells has gained much attention for application in target cancer therapeutics[22]–[24], [27], [33]. Notably, these studies explored the effects of particle size, ligand density, and receptor density on the cellular uptake of the particles [30], [31], [34]–[37].

Gao et al. [27] used thermodynamics and front tracking diffusion kinetics models to study the receptor-mediated uptake of ligand-coated nanoparticles into the cells. Specifically, they considered an initially flat cell membrane of finite size with mobile diffusive receptors and a partially engulfed spherical nanoparticle coated with corresponding ligands [Fig. 1(a)]. Also, the ligands on the nanoparticle surface were assumed to be immobile and uniformly distributed at a density of ε_LWhile the receptors on the cell membrane are mobile and can diffuse in the plane of the membrane until they bind specifically with the ligands on the nanoparticle. In addition, global conservation of the cell receptor density ε_o was assumed to ensure that the total number of receptors on the cell membrane remained constant during the entire nanoparticle wrapping process.

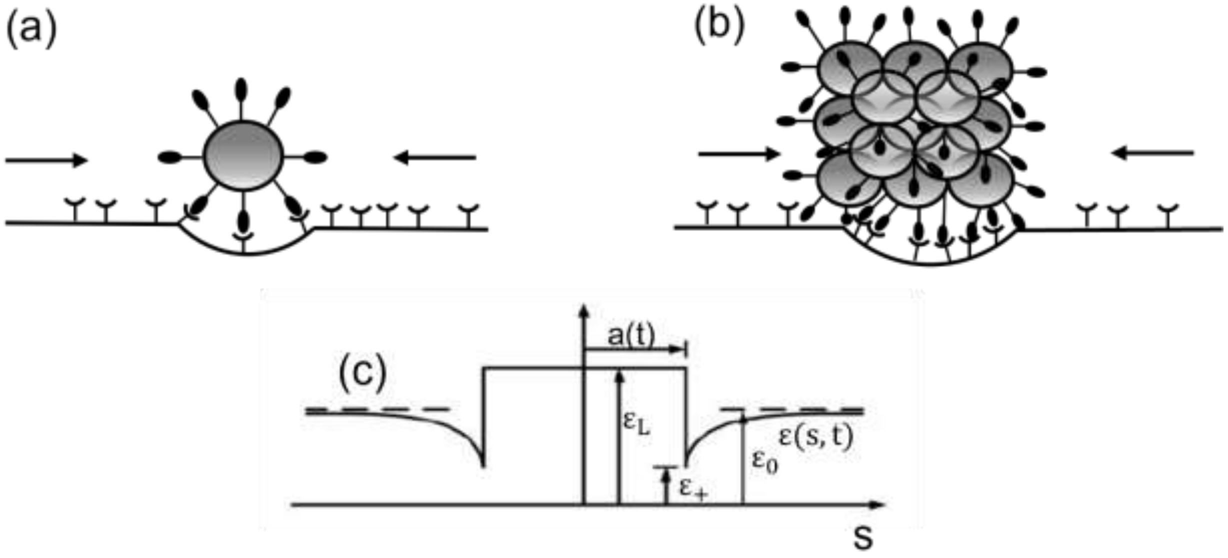

Fig. 4.1. Schematic illustration of (a) An initially flat membrane with diffusive receptors as it wraps around a corresponding ligand-coated nanoparticle. (b) An initially flat membrane with diffusive receptors as it wraps around a cluster of ligand-coated nanoparticles. (c) The receptor density distribution ε_o in the membrane becomes non-uniform upon ligand-receptor binding; the receptor density ε_+ is depleted in the near vicinity of the binding area and induces diffusion of receptors toward the binding site. Adapted from [27].

Before nanoparticle contact with the cell membrane, the receptors are assumed to have a uniform density ε_o. But, upon nanoparticle contact with the cell membrane, a receptor gradient occurs in the contact region [Fig.1 (c)] as the receptor density in the vicinity of contact is elevated to match the ligand density $\mathrm{\varepsilon_L}$within that region. Thus, a diffusive distribution function $\mathrm{\varepsilon}(s, \mathrm{t})$ describes the receptor contact zone diffusion and redistribution on other cell membrane parts.

Thermodynamically, receptor-ligand binding lowers the interaction free energy of the receptor-ligand pair. In contrast, elastic energy increases due to increased local cell membrane curvature and reduced configurational entropy of immobilized cell receptors.

The Free energy function for cell membrane wrapping of a single particle is given by Eq. (4.1.)

$$\mathrm{F(t)} = \mathrm{K_B T}\left\{\int_0^{\mathrm{a(t)}} \left(-\mathrm{\varepsilon_l e_{RL}} + \mathrm{\varepsilon_l} \ln\frac{\mathrm{\varepsilon_l}}{\mathrm{\varepsilon_o}} + \frac{1}{2}\mathrm{BK_p^2}\right)\mathrm{ds} + \int_{\mathrm{a(t)}}^{\mathrm{l}} \mathrm{\varepsilon} \ln\frac{\mathrm{\varepsilon}}{\mathrm{\varepsilon_o}}\,\mathrm{ds}\right\} \tag{4.1}$$

where $\mathrm{K_B}$ is the Boltzmann constant, T is the absolute temperature, a(t) is the radius of the contact region/ arc length of the engulfed area, L is the membrane radius, $\mathrm{\varepsilon_l}$ is the ligand density distribution, and ε_o is the receptor density distribution before ligand contact. Specifically, in Eq. (4.1) $\mathrm{K_B T e_{RL}}$ is the energy of a single receptor-ligand bond, $\mathrm{K_B T \ln\frac{\varepsilon_L}{\varepsilon_o}}$ is the free energy per receptor associated with the loss of configurational entropy of the bound receptors, and $\mathrm{K_B T} \ln\frac{\mathrm{\varepsilon}}{\mathrm{\varepsilon_o}}$ is the free energy per receptor associated with the free cell membrane receptors. Lastly, $\frac{1}{2}\mathrm{BK_B T K_p^2}$ is the elastic bending energy of the membrane associated with the wrapping of a spherical nanoparticle, and $\mathrm{BK_B T}$ is the bending modulus.

4.3.2. Nanoparticle Cluster Entry Model

Experimental evidence (J. Hu et al., 2018a; Meng et al., 2009) has shown that nanoparticle clusters can also be internalized by a biological cell membrane. However, the surface energy effects on the free energy associated with nanoparticle uptake have not been considered for various nanoparticles developed for therapeutic applications. Recently, Meng et al. [28] modified Gao et al.[27] free energy for a single nanoparticle cellular uptake [Eq. (4.1)]by introducing new surface energy terms due to the interactions between nanoparticles, cell culture media, and the cell membrane.

Using modifications in Ref. [28], we consider an initially flat finite-sized cell membrane wrapping of a cluster of ligand-coated spherical nanoparticles [Fig. 4.1b]. Similar to Refs. [28], [29],we assumed that the clusters form a close-packed face-centered cubic (FCC) structure with six nearest neighbors particles on the surface and twelve nearest neighbors particles in the center. In addition, we introduced surface energy terms proposed by Meng et al. [28] to account for the adjacent nanoparticle interactions in a fluid environment. Subsequently, we estimate the net surface energy $\mathrm{U}_{\mathrm{surface}}$ [Eq. 4.2] for an FCC cluster. Where γ_1 is the surface free energy due to nanoparticle/nanoparticle contact, γ_2 is the surface free energy due to nanoparticle/cell culture media contact, and γ_3 is the surface free energy due to nanoparticle/cell-membrane contact.

Now suppose that the contact area between two nanoparticles is denoted as A_c, nanoparticle radius denoted as r and cluster radius is R, the surface energy contribution is described by Eq. (4.2)

$$\mathrm{U}_{\mathrm{surface}} = \mathrm{U}_{\mathrm{nanoparticle-nanoparticle}} + \mathrm{U}_{\mathrm{particle-medium}} + \mathrm{U}_{\mathrm{nanoparticle-cell\ membrane}} \qquad (4.2)$$

$$\mathrm{U_{nanoparticle-nanoparticle}} = \gamma_1 \times 12\mathrm{A_c} \times \left(\frac{4\pi\mathrm{R}^3/3}{4\pi\mathrm{r}^3/3} - \frac{4\pi\mathrm{R}^2}{\pi\mathrm{R}^2}\right) + \gamma_1 \times 6\mathrm{A_c} \times \frac{4\pi\mathrm{R}^2}{\pi\mathrm{R}^2} \qquad (4.3)$$

$$\mathrm{U_{particle-medium}} = \gamma_2 \times (4\pi\mathrm{r}^2 - 12\mathrm{A_c}) \times \left(\frac{4\pi\mathrm{R}^3/3}{4\pi\mathrm{r}^3/3} - \frac{4\pi\mathrm{R}^2}{\pi\mathrm{R}^2}\right) + \gamma_2 \times \left(4\pi\mathrm{R}^2 - \int_0^{\mathrm{a(t)}} \mathrm{ds}\right) \qquad (4.4)$$

$$\mathrm{U_{nanoparticle-cell\ membrane}} = \gamma_3 \times \int_0^{\mathrm{a(t)}} \mathrm{ds} \qquad (4.5)$$

By incorporating this additional surface energy term in Eq. (4.2) into the free energy expression in Eq. (4.1), we obtain an expression for the free energy required to wrap a cluster of nanoparticles. Eq. (4.6).

$$\mathrm{F(t)} = \mathrm{K_B T}\left\{\int_0^{\mathrm{a(t)}} \left(-\varepsilon_\mathrm{l} \mathrm{e_{RL}} + \varepsilon_\mathrm{l} \ln\frac{\varepsilon_\mathrm{l}}{\varepsilon_\mathrm{o}} + \frac{1}{2}\mathrm{B K_p^2}\right)\mathrm{ds} + \int_{\mathrm{a(t)}}^{\mathrm{l}} \varepsilon \ln\frac{\varepsilon}{\varepsilon_\mathrm{o}} \mathrm{ds}\right\} + \mathrm{U_{surface}} \qquad (4.6)$$

The time-independent terms in Eq.4.3 to Eq.4.5 are denoted as constant terms and ignored in the wrapping dynamics[28]. Hence Eq. (4.6) becomes Eq. (4.7).

$$F(\mathrm{t}) = \mathrm{K_B T}\left\{\int_0^{\mathrm{a(t)}} \left(-\varepsilon_\mathrm{l}(\mathrm{e_{RL}} + (\gamma_2 - \gamma_3)/\varepsilon_\mathrm{l}) + \varepsilon_\mathrm{l} \ln\frac{\varepsilon_\mathrm{l}}{\varepsilon_\mathrm{o}} + \frac{1}{2}\mathrm{B K_p^2}\right)\mathrm{ds} + \int_{\mathrm{a(t)}}^{\mathrm{l}} \varepsilon \ln\frac{\varepsilon}{\varepsilon_\mathrm{o}} \mathrm{ds}\right\} + \text{constant terms} \qquad (4.7)$$

The inclusion of the surface energy terms leads to a change in the effective interaction energy between the ligand-receptor pairs and thus affects wrapping dynamics[28], [29]. It is important to note that the surface energy due to interacting nanoparticles ($\mathrm{U_{nanoparticle-nanoparticle}}$) only contributes constant terms to Eq. (4.7), which do not affect the kinetics of receptors and have thus been ignored and $\mathrm{K_p}$ is related to the total mean curvature of the whole cluster[28], [42].

Differentiating the generalized free energy expression Eq. (4.7) with respect to time yields Eq. (4.8)

$$\frac{\dot{F}(t)}{K_B T} = -(\varepsilon_l e_{RL} - \frac{1}{2} B K_p^2 + \varepsilon_l \ln\frac{\varepsilon_+}{\varepsilon_l} + \varepsilon_l - \varepsilon_+ + (\gamma_2 - \gamma_3))a(t) - \dot{\int}_{a(t)}^{\infty} D\varepsilon(\frac{\partial X}{\partial s})^2 \, ds \tag{4.8}$$

$\chi(s,t) = \ln\left(\frac{\varepsilon}{\varepsilon_o}\right) + 1$ is the local chemical potential of a receptor, and its integral is the rate of energy dissipation associated with receptor transport along the cell membrane.

The energy balance between the reduction in the free energy rate gained from the wrapping process and the rate of energy dissipation consumed during receptor simplifies Eq. (4.8) to Eq. (4.9)

$$\varepsilon_l e_{RL} - \frac{1}{2} B K_p^2 + \varepsilon_l \ln\frac{\varepsilon_+}{\varepsilon_l} + \varepsilon_l - \varepsilon_+ + (\gamma_2 - \gamma_3) = 0 \tag{4.9}$$

Assuming there is no free energy jump at the contact edge and solving Eq. (4.9), the receptor density at the boundary ε_+ can be found in Eq. (4.10)[51].

$$\frac{\varepsilon_+}{\varepsilon_l} - \ln\frac{\varepsilon_+}{\varepsilon_l} = e_{RL} - \frac{1}{2}\frac{BK_p^2}{\varepsilon_l} + \frac{(\gamma_2 - \gamma_3)}{\varepsilon_l} + 1 \tag{4.10}$$

The endocytosis of spherical clusters with effective area πL^2, requires that the receptors are conserved throughout the process as satisfied by Eq. (4.11)[52]

$$L^2 \varepsilon_o = 4R^2 \varepsilon_l + (L^2 - 4R^2)\varepsilon_+ \tag{4.11}$$

Re-arranging equation (4.11), we obtain that

$$\frac{\varepsilon_+}{\varepsilon_l} = \frac{(L^2\bar{\varepsilon} - 4R^2)}{(L^2 - 4R^2)} \tag{4.12}$$

Where $\bar{\varepsilon} = \frac{\varepsilon_o}{\varepsilon_l}$

Substituting Eq. (4.12) into Eq. (4.10) and rearranging results in Eq. (4.13).

$$e_{RL} - \frac{2B}{R^2 \varepsilon_l} + \ln\left(\frac{L^2\bar{\varepsilon} - 4R^2}{L^2 - 4R^2}\right) - \left(\frac{L^2\bar{\varepsilon} - 4R^2}{L^2 - 4R^2}\right) + \frac{(\gamma_2 - \gamma_3)}{\varepsilon_l} + 1 = 0 \tag{4.13}$$

Quadratically solving Eq. (4.13) yields the minimum ($\mathrm{R_{min}}$) and maximum ($\mathrm{R_{max}}$) cluster radii.

Also, the wrapping time is estimated by solving the receptor density diffusion function [$\varepsilon(s, t)$]using the diffusion continuity equation, which requires that the arc length of engulfed region $a(t) = 2\alpha\sqrt{Dt}$ where D is the diffusion constant of the free membrane receptors and α is a speed factor and determined from Eq. (4.9).

Hence, the estimated wrapping time $\mathrm{t_w}$ can be obtained as $\pi a(t_w)^2 = 4\pi R^2$ Or $t_w = (\frac{R}{\alpha\sqrt{D}})^2$ and is consistent with Gao et al.[27].

4.3.3. Theoretical Parameters for the Entry of Clusters into Tumorigenic and Non-Tumorigenic Breast Cells

The surface energy terms were estimated $(\gamma_2 - \gamma_3)/\varepsilon_l$ in Eq. (4.7) were estimated to be on the order of 487 K_BT at $\mathrm{T} = 300\mathrm{K}$ using contact angle measurements and Young’s equation similar to prior studies reported in Refs. [28], [29]. Briefly, the cell membrane/nanoparticle surface energy, γ_3 estimations are approximated as the surface energy interactions between glycerol and nanoparticles. As reports show that the cell membrane is mainly composed of a glycerol backbone [53], [54]. In addition, γ_2 was estimated as the surface energy between water and the nanoparticles [55]since the cell media and bodily fluids are mostly composed of water.

The lower bound (50 $\mu\mathrm{m}^{-2}$) and upper bound (500 $\mu\mathrm{m}^{-2}$) receptor densities ε_o were based on Refs. [27], [34], [40], [56] including results from Ref. [57] that show that number of Gonadotropin-Releasing Hormone Receptor (GnRH-R) binding sites in MCF-7 breast cancer cells is consistent with the 500 receptors per $\mu\mathrm{m}^2$ estimate.

Furthermore, the kinetics of nanoparticle cluster wrapping was estimated for an optimum ligand density(5×10^3 Ligands/μm^2) based on reports of the extensively studied semliki forest virus [22], [27], [32], [58], [59]. The ligand density was idealized as optimum to investigate only the surface energy and receptor density effects on the nanoparticle cluster wrapping time and radius. Lastly, values of Receptor-ligand binding energy, eRL ($15k_BT$ at T = 300K), bending rigidity of the cell membrane B($20k_BT$), the diffusion coefficient of receptors D (10^4 nm^2/s), and cell membrane length (10 μm) were adapted from Gao et al. [52]

4.4. Results

4.4.1. Gold Nanoparticle Synthesis and Characterization

After 24 hours, CFE reduced gold (III) chloride trihydrate to gold. This reduction process was observed via a color change from pale yellow to purple in the gold (III) chloride trihydrate mixture and cell-free extract (CFE) from Serratia marcescens [46], [60], [61].

Furthermore, UV-Vis spectrophotometry methods indicated the presence of gold via maximum absorption wavelengths [Fig. 4.2] in the absorption spectra of GNP(565 nm), GNP-TRP(571 nm), GNP-PEG(570 nm), and GNP-PEG-TRP(569.5 nm). In addition, the absorption spectra [Fig. 4.2 b] reveals TRP ligand signatures at 267 nm[26], [62] in GNP-TRP and GNP-PEG-TRP.

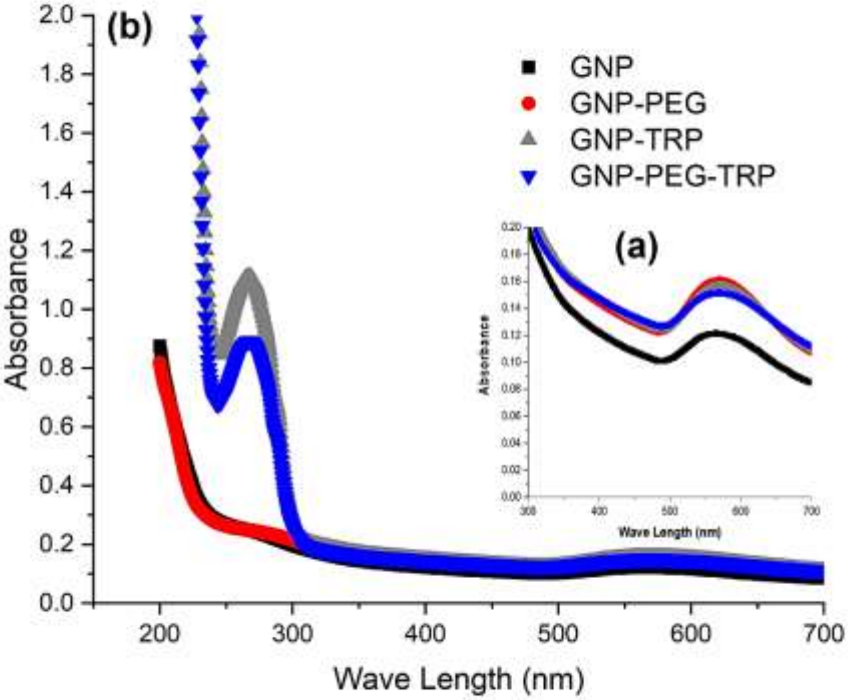

Fig. 4.2. UV-Vis absorption spectra of (a) biosynthesized gold nanoparticles (GNP, GNP-PEG, GNP-TRP, GNP-PEG-TRP with maximum absorption wavelengths at 565, 571, 570, and 569.5 nm respectively and TRP ligand signatures at 267 nm (b).

The measured increase in UV-Vis absorbance values (Fig.4.2.) is generally due to the spectral redshift of maximum absorption wavelength are due to the changes in the nanoparticle size[26], [46], [63]. The observed maximum absorption wavelength indicates the presence of gold nanoparticle sizes that range from 10 to 40 nm [26], [63], [64].

Further characterization with the TEM reveals micrographs in Fig. 4.3 with spherical GNP, GNP-PEG, GNP-TRP, and GNP-PEG-TRP nanoparticles. The core diameter distribution for the four nanoparticles in Fig. 4.4 reveals that the nanoparticles have a 10 – 30 nm size distribution. However, although the TEM micrographs show average diameter sizes of 16.7 ± 4.1 nm (GNP), 15.6 ± 5.6 nm (GNP-TRP), 14.6 ± 4.2 nm (GNP-PEG), and 15.8 ± 4.6 nm (GNP-PEG-TRP), the hydrodynamic diameter(D) for the GNP (64.7 ± 1.0 nm), GNP- TRP (139.7 ± 1.1 nm), GNP-PEG (55.2 ± 0.2 nm), and GNP-PEG-TRP (76.9 ± 0.1 nm)) were much larger.

Table 4.1 Summary of DLS and Zetasizer measurements showing polydispersity index (PDI) and Zeta potential (ξ) values for GNP, GNP-TRP, GNP-PEG, GNP-PEG-TRP in Distilled water (Di-water).

	PDI	**Zeta-potential ξ (mv)**
GNP	0.29 ± 0.05	-24.9 ± 1.6
GNP-PEG	0.23 ± 0.00	-30.2 ± 1.1
GNP-TRP	0.22 ± 0.01	-26.2 ± 2.9
GNP-PEG-TRP	0.23 ± 0.00	-29.6 ± 0.8

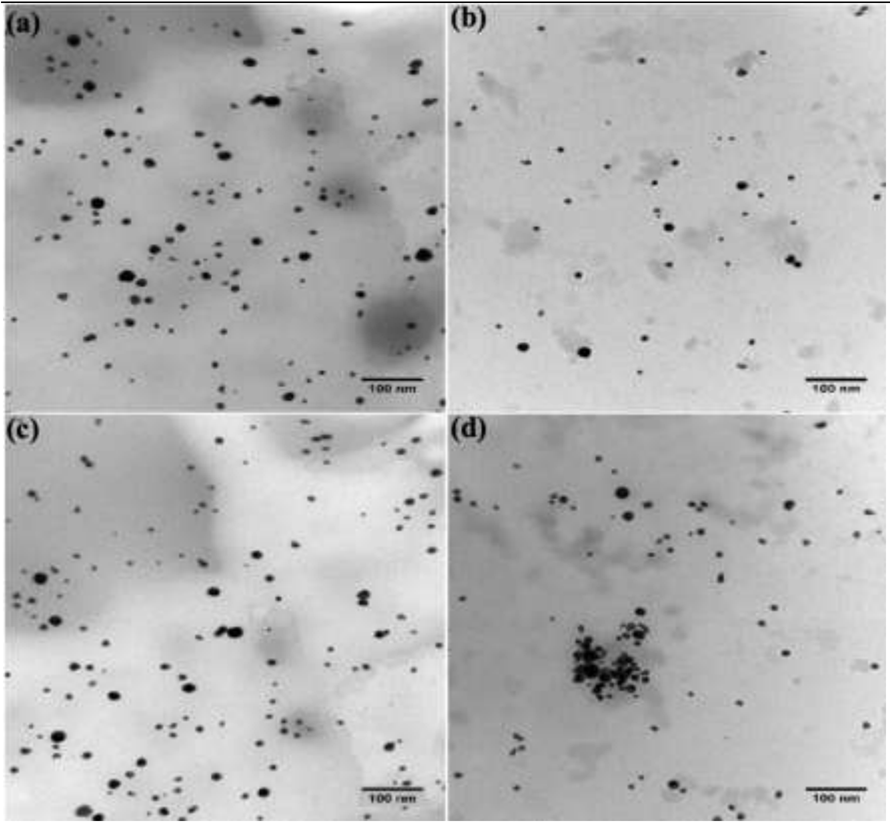

Fig. 4.3. TEM micrographs of (a) GNP; (b) GNP-TRP; (c) GNP-PEG; (d) GNP-PEG-TRP.

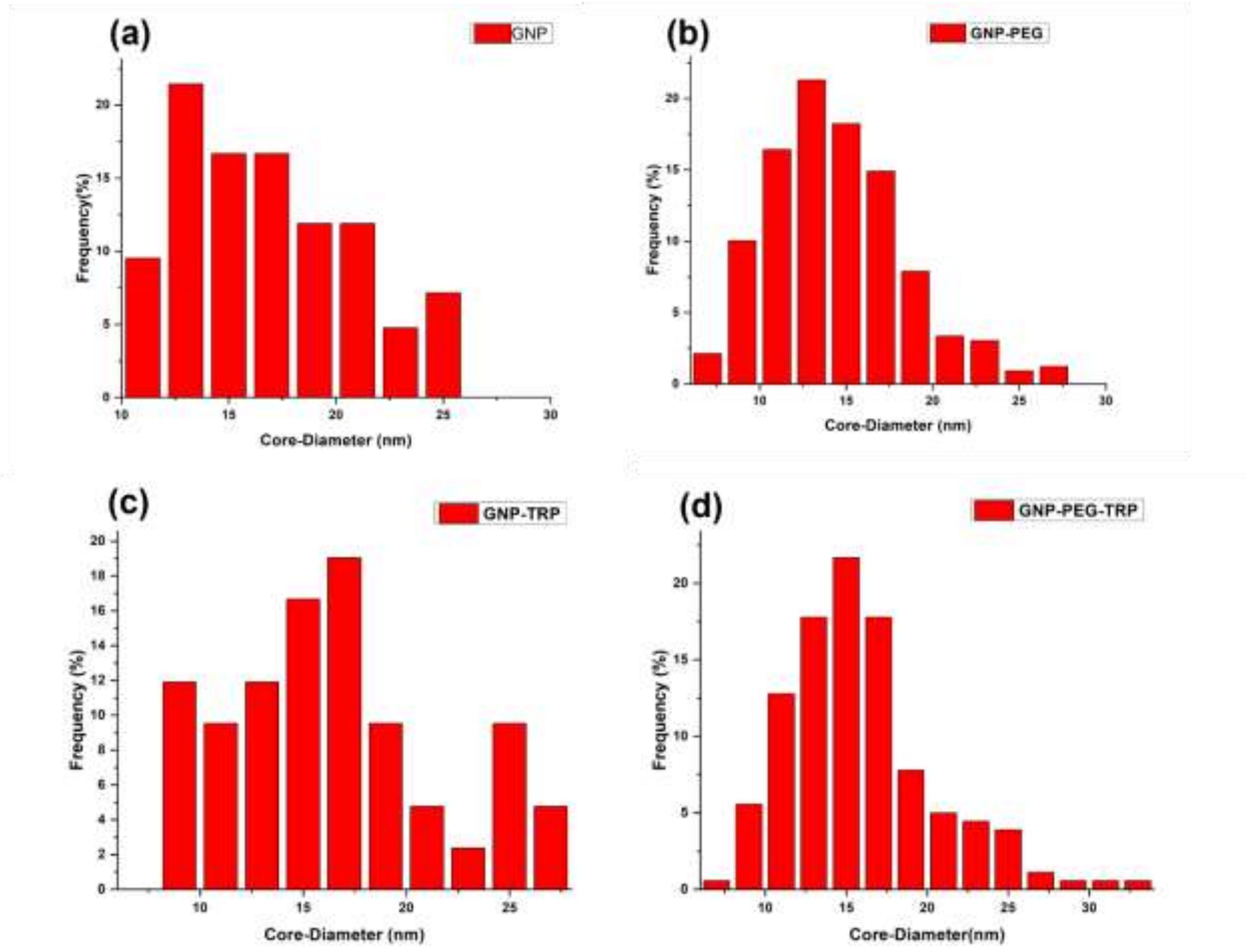

Fig. 4.4. (a) TEM core diameter distribution of GNP, (b) TEM core diameter distribution of GNP-PEG, (c) TEM core diameter distribution of GNP-TRP, and (d) TEM core diameter distribution of GNP-PEG-TRP.

Fig. 4.5 reveals the FTIR spectra for CFE, TRP ligand, GNP, GNP-PEG, GNP-TRP, and GNP-PEG-TRP nanoparticles from a wavelength of 400 - 4000 cm^{-1}. Notably, the FTIR bands for CFE confirm the presence of carbonyl (aldehyde groups) at 1741 and 1835 cm^{-1}. In addition, C-H groups commonly found in organic molecules are present at 2931 cm^{-1} [49], [65]. Interestingly, just like the CFE spectra, GNP analysis [Fig. 4.5] revealed peaks for carbonyl groups (1835, 1741, and 1692 cm^{-1}). The presence of carbonyl groups on GNP surfaces is associated with adsorbed proteins on the GNP surface due to the biosynthesis method used. A similar FTIR study on the biosynthesis of silver and zinc nanoparticles using a macro-algae extract (Gracilaria Edulis) also reported the presence of carbonyls in the CFE and on the surfaces of the biosynthesized nanoparticles [66].

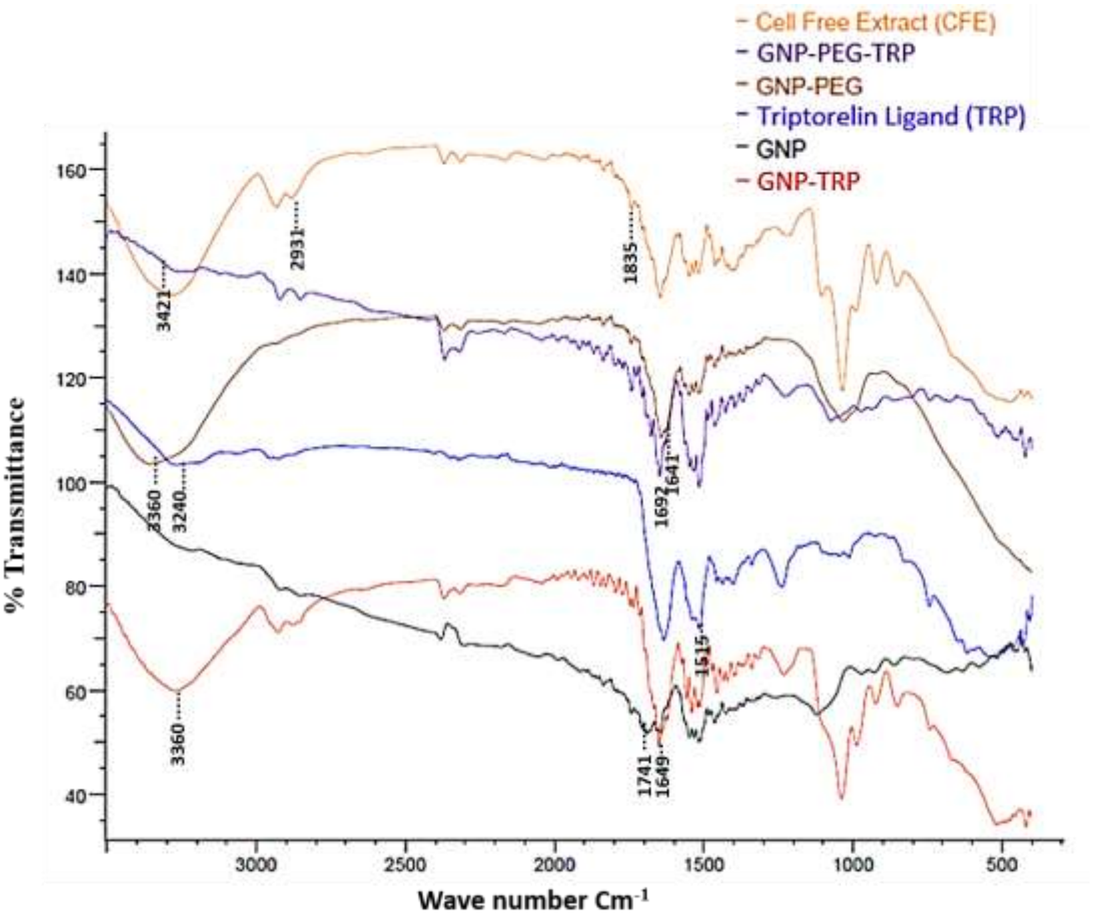

Fig. 4.5. FTIR spectra of the cell-free extract, GNP-PEG-TRP, GNP-PEG, TRP ligand, GNP-TRP, and GNP.

Next, the GNP-PEG spectra showed carboxylic group peaks at 3360 cm^{-1} for the OH group, while C=O peaks at 1710 and 1641 cm^{-1} confirmed the presence of a carboxyl terminated polyethylene glycol[67], [68]. Furthermore, GNP-TRP spectra revealed amine functional group peaks (N-H) that were present in the TRP ligand spectra at 1515, 1635, and 3200-3600 cm^{-1}. Markedly, the carbonyl group peaks (C=O) that were present in the GNP spectra were absent and thus confirmed the formation of the C=N bonds at 1649 cm^{-1} found within the 1640-1690 cm^{-1} range [19], [65], [69]. Although carbonyls are reactive to primary amines, these interactions do not produce strong, stable bonds and require other amination processes [49], [50].

Lastly, the primary amide bond formation in GNP-PEG-TRP spectra at C=O at 1692 cm^{-1} and N-H at 3421 and 3481 $\mathrm{cm}^{-1}$is significant and confirms that the carbodiimide (EDC/NHS catalyst) conjugation process between the carboxyl and primary amine groups occurred [17], [70].

4.4.2 Nanoparticle Cellular Uptake into TNBC and non-Tumorigenic Breast Cells

We examined the cellular uptake of GNP, GNP-PEG, GNP-TRP, and GNP-PEG-TRP nanoparticles into non-tumorigenic MCF-10A cells and TNBC cells (MDA-MB-231 and MDA-MB-468) using confocal fluorescence microscopy techniques.

Interestingly, MDA-MB-231 and MDA-MB-468 cells internalized all four nanoparticles within the 5 min to 3h incubation window. However, MCF-10A cells internalized only GNP-PEG and GNP-TRP nanoparticles after the 1h mark. Interactions between GNP-PEG-TRP and TNBC/MCF-10A cells are of particular significance because of their preferential accumulation [Fig. 4.6] in MDA-MB-231 and MDA-MB-468 cells than in MCF-10A cells. Fig. 4.6 shows the Z-axis maximum projection of 3D confocal fluorescence images which show GNP-PEG-TRP interactions with MCF-10A (Fig. 4.6 g), MDA-MB-231(Fig. 4.6 h), and MDA-MB-468 (Fig. 4.6 i) cells, as well as the control samples which includes cells without nanoparticles in Fig. 4.6, (a),(b), and(c) and GNP-PEG interactions with MCF-10A (Fig. 4.6 d), MDA-MB-231(Fig. 4.6 e), and MDA-MB-468 (Fig. 4.6 f) cells after the 3h incubation window had elapsed.

It is important to note that GNP-PEG-TRP [Fig. 4.6] was the only particle among the four nanoparticles selectively internalized by both TNBC cells and not in the non-tumorigenic MCF-10A cell throughout the 3h incubation window.

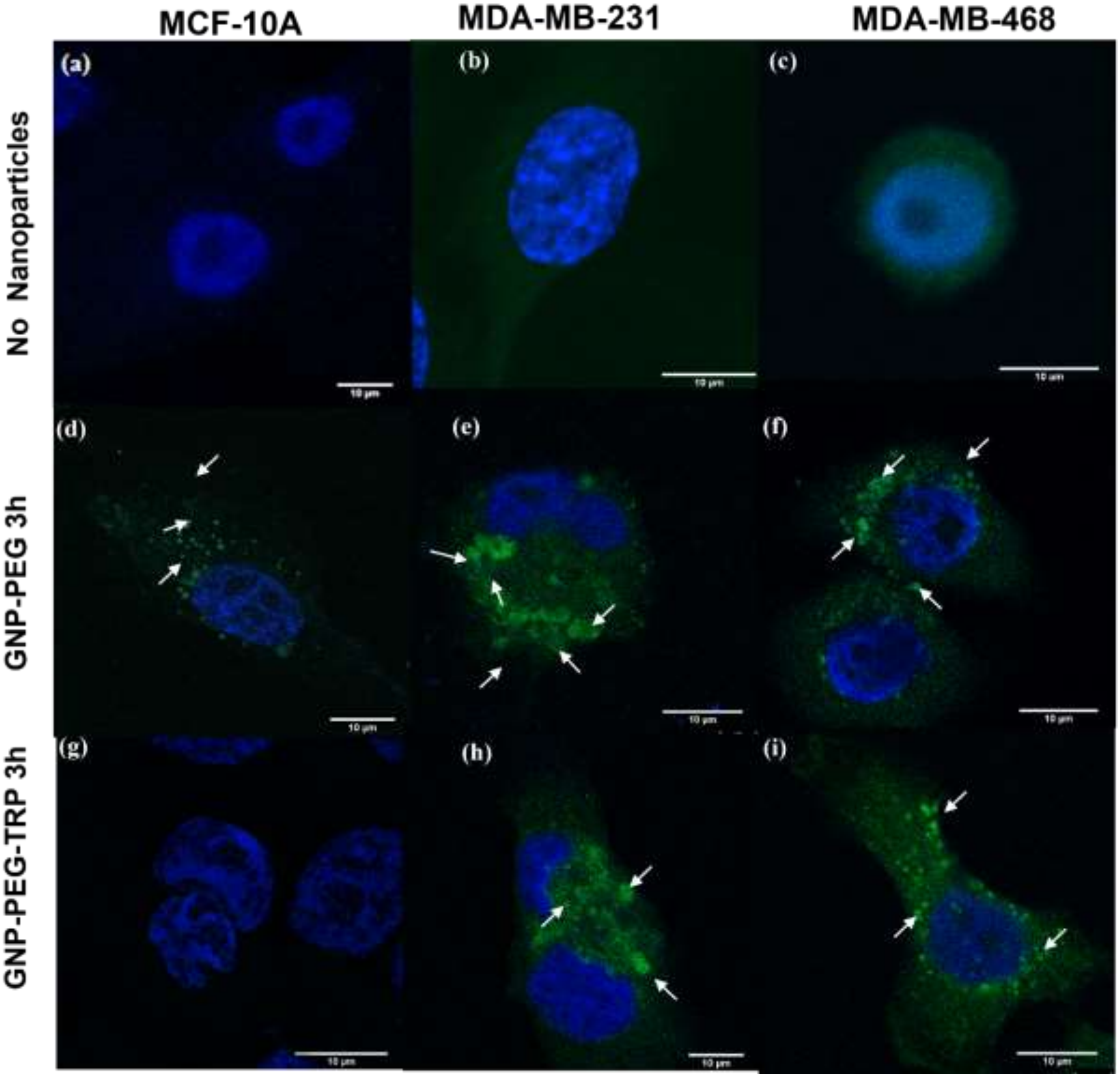

Fig.4.6. Z-axis maximum intensity projection of 3D fluorescence confocal images for (a) non-tumorigenic MCF-10A, (b) TNBC MDA-MB-231, and (c) TNBC MDA-MB-468 cells without nanoparticles; for (d) MCF-10A, (e) MDA-MB-231, and (f) MDA-MB-468 cells incubated with GNP-PEG nanoparticles for 3h; and for (g) MCF-10A, (h) MDA-MB-231, and (i) MDA-MB-468 cells incubated with GNP-PEG-TRP nanoparticles for 3h. the cell nucleus is stained blue with DAPI (4′, 6-diamidino-2-phenylindole), while the LHRH receptors are stained green with FITC (fluorescein isothiocyanate), with arrows pointing towards clusters.

Interestingly, at 3h, GNP-PEG-TRP clusters were observed within the nucleus of MDA-MB-468 cells[Fig. 4.7]. A montage of the 3D confocal fluorescence images showing the internalized GNP-PEG-TRP clusters in MDA-MB-468 is presented in Fig. 4.7. The positions of the internalized GNP-PEG-TRP clusters with respect to the cell-substrate are identified by white arrows, while nanoparticles within the nucleus are identified by red arrows in Fig. 4.7 (c) at 0.22 µm, (d) at 0.26 µm, (f) at 0.34 µm, (g) at 0.39 µm, and (h) at 0.43 µm. It is important to note that GNP-PEG-TRP clusters in Fig. 4.7(c) and (d) are not in Fig. 4.7 (a), (b), (e), and (f), indicating that these clusters were internalized by the MDA-MB-468 cells.

In general, the measured cluster size range in MDA-MB-231 cells [Fig. 4.8] was broader (0.5 to 4 µm) than the size range in MDA-MB-468(0.5 to 2.5 µm)[Fig. 4.9] and MCF-10A cells(0.2 to 1µm) [Fig. 4.10]. Furthermore, an increase in incubation time from 5min to 3h led to an increase in cluster sizes formed [Fig. 4.8, 4.9, 4.10].

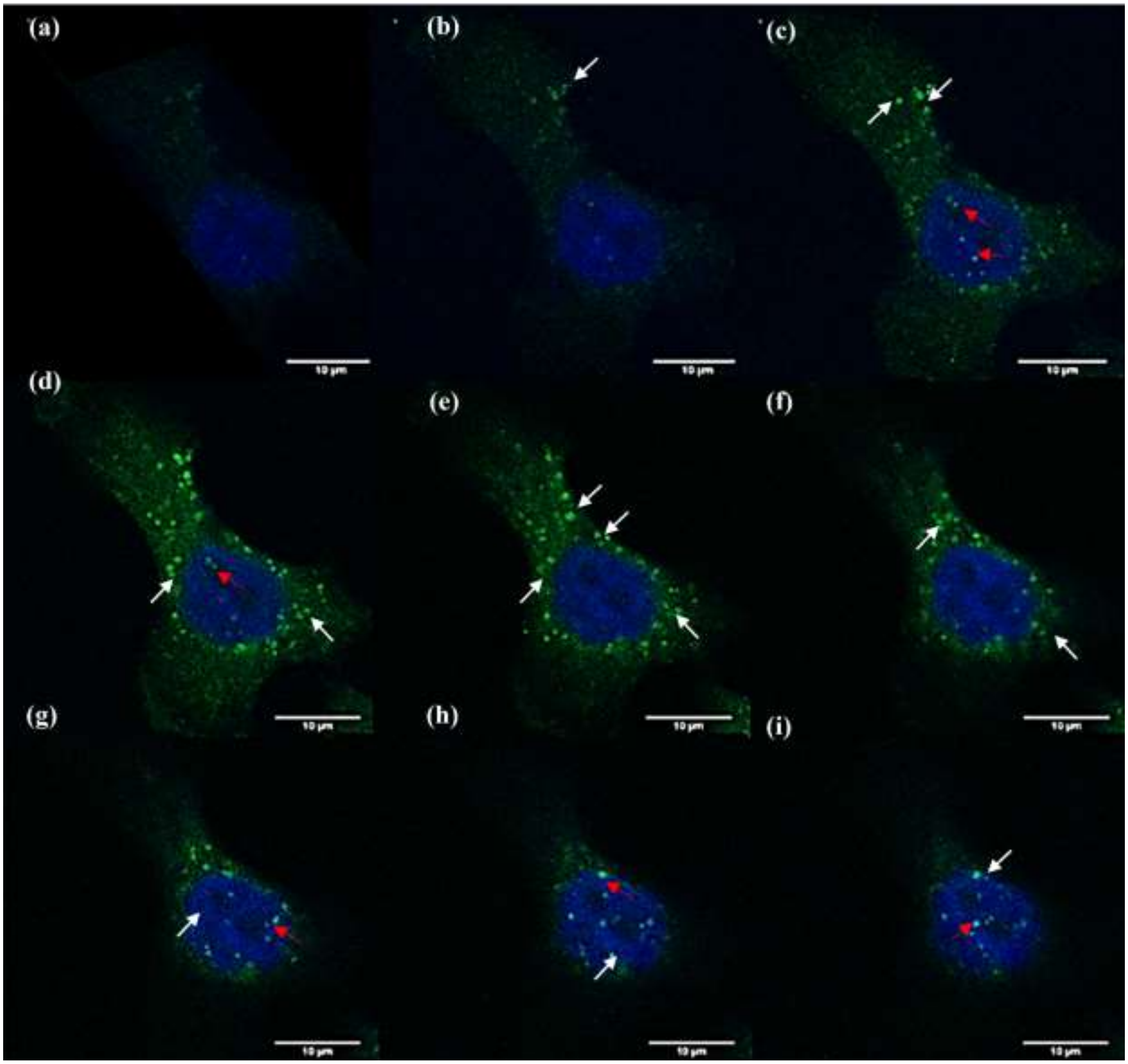

Fig.4.7. Z-stack confocal fluorescence images with white arrows showing the GNP-PEG-TRP nanoparticle cluster distribution in MDA-MB-468 breast cancer cells after 3h, at incremental distance of (a) 0.13 µm (b) 0.17 µm (c) 0.22 µm, (d) 0.26 µm, (e) 0.3 µm, (f) 0.34 µm (g) 0.39 µm (h) 0.43 µm (i) 0.47 µm from the substrate. Red arrows indicate locations of GNP-PEG-TRP particles within the nucleus.

4.4.3 Nanoparticle Cluster Size Distribution

The uptake and distribution of GNP, GNP-PEG, GNP-TRP, and GNP-PEG-TRP markedly differed for MDA-MB-231, MDA-MB-468, and MCF-10A cells. In particular, MCF-10A cells did not engulf any GNP clusters throughout the 3h incubation window. However, GNP formed a broad range of clusters (0.5 to 4 µm) in MDA-MB-231cells. Interestingly, at 3h, only GNP clusters ≥ 1.5 µm were distributed within MDA-MB-231 cells [Fig. 4.8 a]. Notably, GNP uptake into MDA-MB-468 cells only began after 30min[Fig. 4.9 a] and GNP clusters in MDA-MB-468 were sparse compared to MDA-MB-231 cells[Fig. 4.8 a]. Furthermore, 88% of the GNP clusters in MDA-MB-468 cells were between 0.5 and 1.5µm[Fig. 4.9 a].

Furthermore, the GNP-PEG particles presented quite differently from GNP in the cells. For example, in the MDA-MB-231 cells, the GNP-PEG cluster size distribution was ≤ 2.5 µm.

For GNP-PEG particles, MDA-MB-468 cells rapidly engulfed GNP-PEG particles within 5min, contrasting the 30min uptake delay observed in the uptake of GNP into MDA-MB-468 cells. In addition, 75 to 84% of the GNP-PEG cluster sizes were between 0.5 and 2µm. However, we observed a cluster of GNP-PEG particles that were ≥ 3.5 µm in size [Fig.4.]. Finally, it is pertinent to note that GNP-PEG entry into MCF-10A cells was only favorable after 1h at smaller cluster sizes ≤ 1µm, differing from the broader clusters found in MDA-MB-231 and MDA-MB-468 cells.

Clearly, the experiments show alternate cluster entry pathways for GNP/MDA-MD-231, GNP/MDA-MB-468, GNP-PEG/MDA-MB-231, GNP-PEG/MDA-MB-468, GNP-PEG/MCF-10A, and GNP-TRP/MCF10A pairs. However, these non-LHRH mediated entry routes are beyond the scope of this paper and require further investigation. Other important non-receptor mediated entry mechanism has been reported in the literature [71]–[75] and requires further investigation.

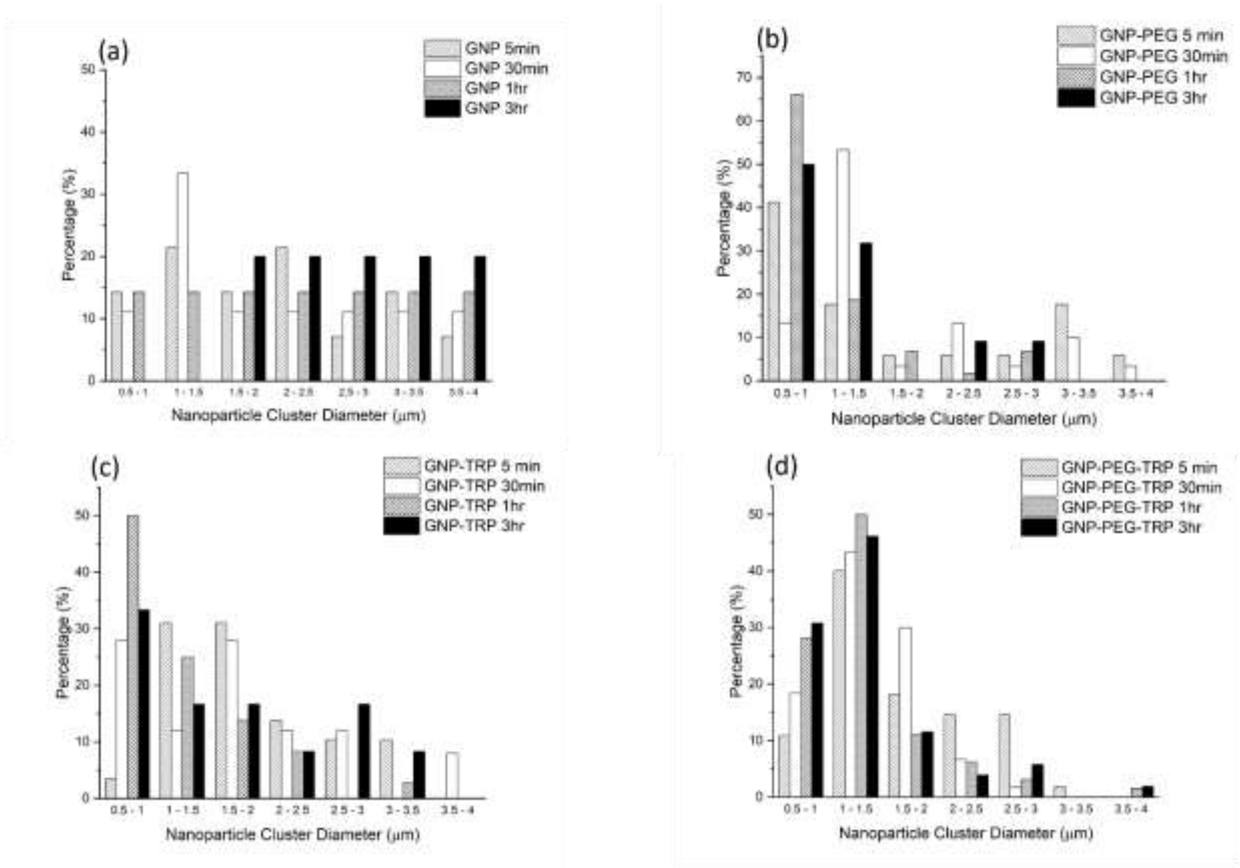

Fig.4.8. Nanoparticle cluster size distribution at 5 min, 30 min, 1 h, and 3 h for (a) GNP/MDA-MB231 breast cancer cells, (b) GNP-PEG/ MDA-MB-231 breast cancer cells, (c) GNP-TRP/ MDA-MB231 breast cancer cells, and (d) GNP-PEG-TRP/ MDA-MB-231 breast cancer cells.

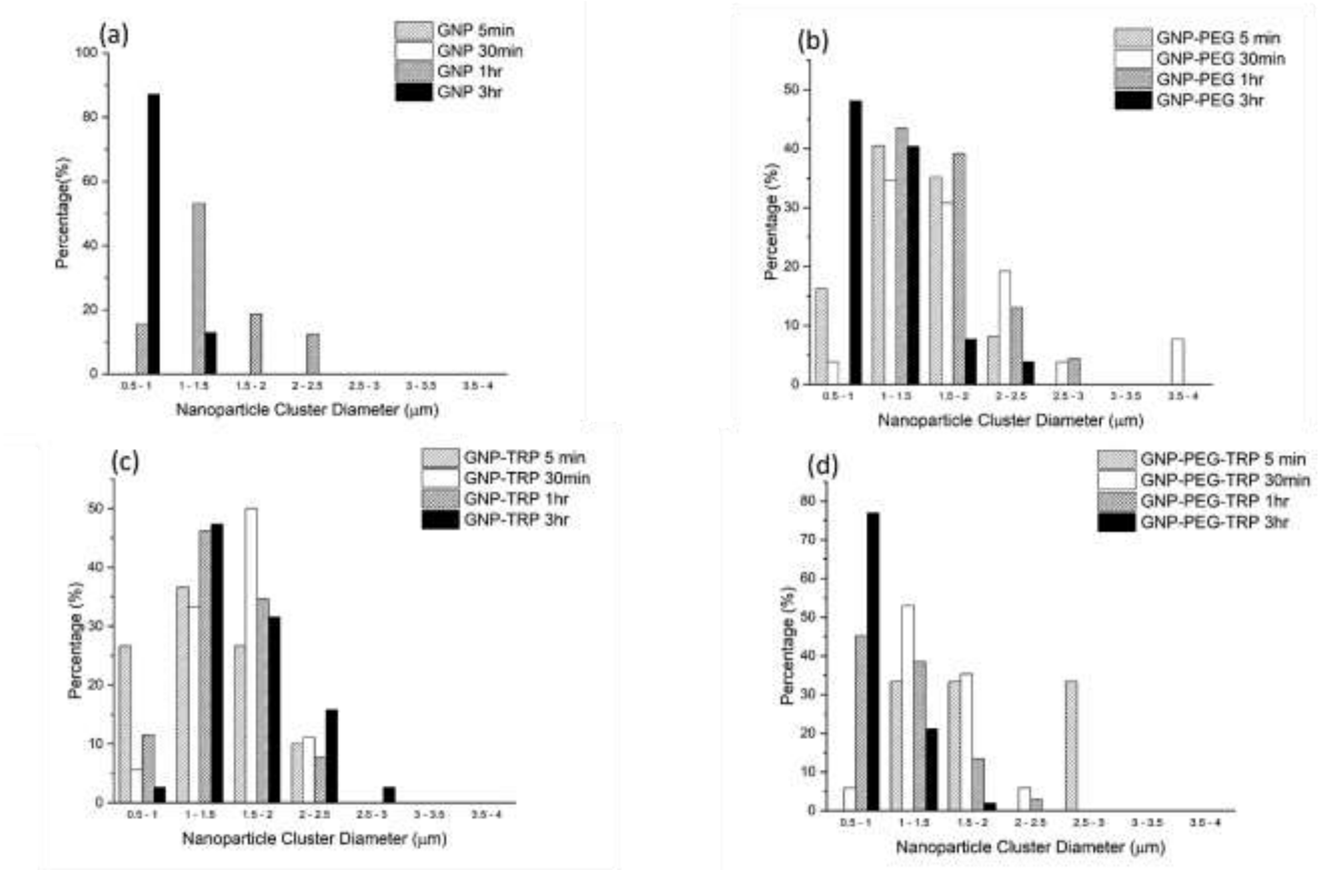

Fig.4.9. Nanoparticle cluster size distribution at 5 min, 30 min, 1 h, and 3 h for (a) GNP/MDA-MB-468 breast cancer cells, (b) GNP-PEG/ MDA-MB-468 breast cancer cells, (c) GNP-TRP/ MDA-MB-468 breast cancer cells (d) GNP-PEG-TRP/ MDA-MB-468 breast cancer cells.

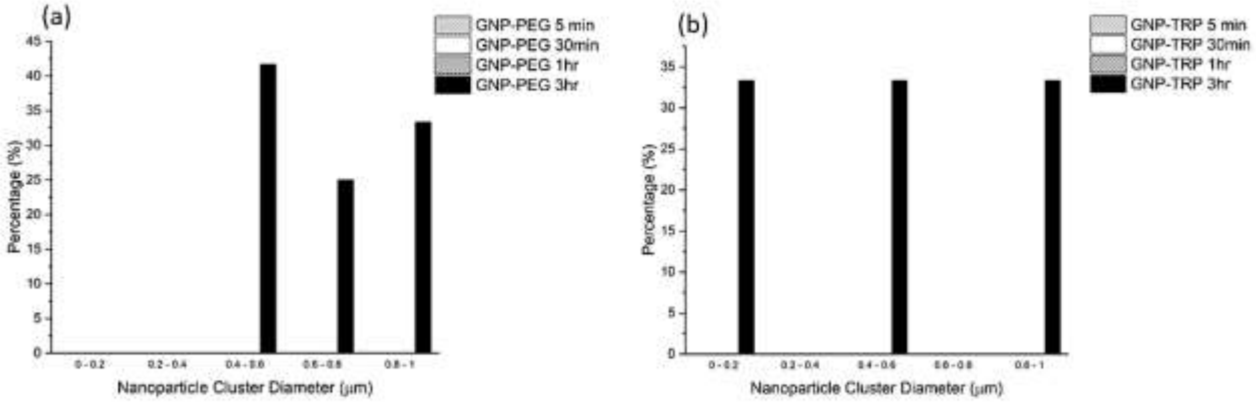

Fig.4.10. Nanoparticle cluster size distribution at 5 min, 30 min, 1 h, and 3 h for (a) GNP-PEG/MCF 10A Normal breast cells and (b) GNP-TRP/MCF 10A Normal breast cells.

4.4.4 Cluster Model for Nanoparticle Cluster Entry into Cells

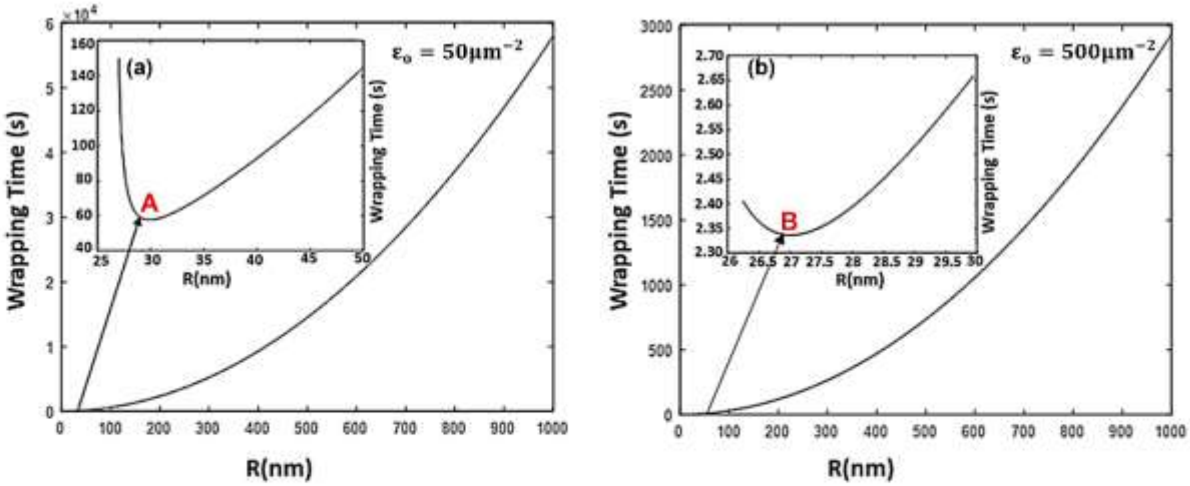

Fig.4.11. The nanoparticle cluster wrapping time tw, versus the radii R, for a 10 μm cell membrane with (a) receptor density of 50 per μm2 and (b) receptor density of 500 per μm2. The arrows point to the minimum wrapping time, tw, and the corresponding optimum particle radius for internalization, Ropt Given by A(30.0 nm, 61s) and B(26.9 nm, 2.33s).

Fig.4.11 (a) and (b) shows the plot of nanocluster wrapping time t_w versus cluster radius for a 10 μm with 50 (a)and 500 (b) receptors per μm^2. For a cell membrane with 50 receptors per μm^2 The predicted wrapping times for clusters radii of 30 nm to 1 μm in size were 61 s to 16 h. In contrast for cell membrane with 500 receptors per μm^{2}The predicted wrapping time for a 26.9 nm cluster is 2.33 s, while a 1 μm cluster is engulfed at 49mins.

The minima points are labeled A and B in Fig. 4.11 (a) (30.0 nm, 61 s) and Fig 4.2. (b) (26.9 nm, 2.33s). These minima point Fig. 4.11 (a) and (b) are the optimum wrapping times and cluster sizes at 50 and 500 cell membrane receptors per μm^2 respectively. Hence, Fig. 4.11 shows that the predicted wrapping times increase for nanoparticle clusters less than or greater than the optimal size.

Also important is the $\mathrm{R_{min}}$ (24.2 nm)and $\mathrm{R_{max}}$(1.6 μm) values estimated[Eq. (4.13)]for a 10μm cell membrane. Hence, the free energy for cluster uptake [Eq.4.] suggests that the wrapping process is only thermodynamically favorable between cluster sizes of 24.2 nm and 1.6 μm if the elastic energy of the cell membrane is much less than the energy associated with the receptor-ligand binding ($\frac{1}{2} BK_BTK_p^2) \ll \quad K_BTe_{RL}$).

It is important to note that the estimated surface energy term $(\gamma_2 - \gamma_3)/\varepsilon_l$ in Eq. 4.7 determined is on the order of 487 K_BT. For gold nanoparticles, this positive surface energy term slightly changes the kinetics of cluster entry from a single particle model, as observed in the increase in optimum wrapping times compared to the range reported in Ref. [27] for single particles. This observed increase in the predicted $\mathrm{t_w}$ differs from previous reports on cluster surface energy effects on $\mathrm{t_w}$ [28], [42]. Notably, J.Hu et al. [29] predicted longer wrapping times (4 to 81 s) for LHRH conjugated magnetite nanoparticle clusters of 16 to 18 nm.

Interestingly, results from the literature show that the surface energy of nanoparticle clusters varies based on the physical and chemical properties of the single particles. For instance, factors such as particle size, structure, and surface charge have been shown to influence surface energy [76]–[79]. Therefore, these variations in cluster surface energy and their influence on wrapping time/optimal radii require further investigation beyond the scope of this study.

4.5. Discussions

4.5.1. Nanoparticle Characterization

Notably, the DLS hydrodynamic diameter measurements were larger than the TEM core diameter sizes in Fig. 4.2, and 4.3. The stark differences in particle sizes are primarily due to the hydration shell around the nanoparticles in water and aggregation of GNP due to the slight increase in the measured zeta potential value ($\xi > -25$ mV). In addition, the DLS works by measuring the variations in scattered light intensity via the Stokes-Einstein equation and a correlation function [80]. However, from Rayleigh's theory, the intensity of scattered light is proportional to the sixth power of the diameter; thus, the analysis is skewed towards the measurement of larger particle sizes while smaller particles are obscured [80]. Furthermore, the TRP ligand and PEG coatings are low atomic number (Z) molecules that are transparent to transmission electron beams[81], [82]. Lastly, the polydispersity index (PDI) and the zeta potential (ξ) of the nanoparticles [Table 4.1] are within an acceptable dispersity (0.1 to 0.3) and stability ($\xi < -25$ mV) range for maximum ligand exchange, drug delivery, and in-vivo applications [83].

4.5.2. Nanoparticle Cellular Uptake

The size distribution of nanoparticle clusters in non-tumorigenic MCF-10A cells and TNBC (MDA-MB-231 and MDA-MB-468) cells were presented in Section 4.4.2. The detection of smaller cluster sizes is limited by the resolution (0.2μm laterally and 0.6 μm axially)of the confocal fluorescence microscope[84], [85]. However, the experiments demonstrate that the combination of PEG coatings and TRP ligands facilitates the selective accumulation of GNP-PEG-TRP clusters in both TNBC cells. Quite notably, Luteinizing Hormone Releasing

Hormone(LHRH) peptides such as TRP or its analogs have a high binding affinity to LHRH receptors (K_D in nM range) and possess the ability to recognize a broad variety of tumors including TNBC but not non-tumorigenic cells[86]–[92].

Besides LHRH receptor endocytosis pathways, nanoparticles can also be internalized via alternate routes[71]–[75]. Interestingly, LHRH receptor-independent uptake was observed in GNP/MDA-MD-231, GNP/MDA-MB-468, GNP-PEG/MDA-MB-231, GNP-PEG/MDA-MB-468, GNP-PEG/MCF-10A, and GNP-TRP/MCF10A pairs. The exact uptake mechanisms in these pairs are unknown and require further investigation. However, this is beyond the scope of this paper. Nevertheless, GNP-PEG-TRP nanoparticles were more selectively internalized by TNBC due to the combination of PEG coating and triptorelin ligand conjugation Fig. 4.6. However, it is unclear if the LHRH receptor-mediated cluster uptake is clathrin-dependent and requires further studies beyond the scope of this paper.

PEG coatings generally reduced large cluster formation[64] and enhanced uptake in TNBC and non-tumorigenic breast cells, while GNP nanoparticles were the least internalized by all cells except MDA-MB-231.

4.5.3. Comparison of Nanoparticle Cluster Models and Experiments

The thermodynamics-kinetics wrapping time model (Section 4.4.4) simulates the LHRH receptor interactions with TRP functionalized GNP for clusters sized 24 nm to 1µm. Interestingly, the in-vitro results in Sections 4.4.2 and 4.4.3 include details of LHRH receptor-mediated cluster entry and nanocluster uptake in cells based on alternate entry mechanisms for cluster diameters of 0.5 to 4 µm. However, we focus our discussion on the preferential accumulation of GNP-PEG-TRP in TNBC MDA-MB-231 and MDA-MB-468 in contrast to the non-tumorigenic MCF-10A cell.

Table 4.2 Estimated wrapping time $\mathrm{t_w}$ for selected nanoparticle cluster sizes (radii) with initial receptor density ε_o of 50 and 500 $\mu\mathrm{m}^{-2}$.

Cluster µm	$\mathbf{t_w}$ **for** $\boldsymbol{\varepsilon_o}$ **=50** $\boldsymbol{\mu}\mathbf{m}^{-2}$	$\mathbf{t_w}$ **for** $\boldsymbol{\varepsilon_o}$ **=500** $\boldsymbol{\mu}\mathbf{m}^{-2}$
0.1	11 min	56 s
0.2	41 min	2 min
0.3	90 min	5 min
0.4	3 h	8 min
0.5	4 h	13 min
0.6	6 h	18 min
0.7	8 h	25 min
0.8	10 h	32 min
0.9	13 h	41 min
1.0	16 h	49 min

Table 4.2 presents wrapping times for specific cluster sizes in Fig. 4.11(a) and Fig. 4.11(b). The model predicts that the wrapping time for a 1 µm particle into a 10 µm cell membrane with 50 receptors per $\mu\mathrm{m}^2$ is 16 h. In addition, at 50 receptors per $\mu\mathrm{m}^2$ Fig. 4.11 (a) predicts that it takes 41min to 4h to wrap cluster sizes of 0.2 to 0.5 µm. In contrast, for a 10 µm cell membrane with 500 receptors per $\mu\mathrm{m}^2$ the model predicts that the wrapping time for a 1 µm cluster is 49 min. At 500 receptors per $\mu\mathrm{m}^2$ the model estimates that it takes about 1 to 13 min to internalize clusters of 0.2 to 0.5 µm.

In general, the theoretical predictions of wrapping time predictions Table 4.2 are consistent with the invitro entry and distribution of GNP-PEG-TRP clusters into both TNBC cells [Fig. 4.8 (d) and 4.9 (d)]. Specifically, the MDA-MB-231 cells in Fig. 4.8 (d) accumulated clusters radii of 0.25 to 1.5 µm within 5 min, and by 1h, cluster radii observed ranged from 0.25 to 2 µm. Similarly, the clusters in MDA-MB-468 cells in Fig. 4.9 d ranged from 0.25 to 1.45 µm within 30 mins and 0.25 to 1.5 µm by 1hr. Additionally, it is important to note that GNP-TRP entry into MCF-10A cells only occurred between 1 to 3 h for cluster sizes of 0.1 to 0.5 μm [Fig.4.10. (a)]. GNP-TRP/MCF-10A interaction [Fig.4.10 (b)] is consistent with the model prediction for the lower bound receptor density (50 receptors per μm^2).

However, further investigation is needed to determine if GNP-TRP/MCF-10A interactions are LHRH receptor-mediated or non-LHRH receptor-dependent because Refs. [71], [72] report that small scale (0.1 to 1 μm) non-receptor dependent entry mechanisms. Such small-scale non-LHRH receptor-related GNP-PEG uptake was observed in MCF-10A cells between 1 and 3h. However, these alternate uptake mechanisms are beyond the scope of this work.

Nevertheless, the clear preferential wrapping of TRP functionalized PEG-coated gold nanoparticles (GNP-PEG-TRP) in TNBC cells and not in the non-tumorigenic cell is enhanced by the expression of more LHRH receptors on the surfaces of the cells and the combination of TRP and PEG modifications to the GNP surface. Notably, the expression of Luteinizing Hormone Releasing Hormone (LHRH) receptors[88] in pancreatic, ovarian, endometrial, and breast cancer has received much attention [87]–[92] due to the minimal to non-expression of LHRH receptors in non-tumorigenic cells/tissues and the potential use of LHRH receptors for targeted various cancer therapeutics[87]–[92].

Furthermore, the quantitative expression of the LHRH receptors has been reported in MDA-MB-231, MDA-MB-468, and MCF-10A cells using either RT-PCR or western blot methods[87], [89], [98], [90]–[97]. These results have revealed that very minimal LHRH receptors were detected in the non-tumorigenic cell line (MCF-10A) compared to MDA-MB-231 [87], [90], [91], [96] and MDA-MB-468 [97], [98]. These findings support that the preferential nanoparticle accumulation of GNP-PEG-TRP particles in TNBC cells and not in MCF-10A is due to the overexpression of

LHRH receptors and the increase in free energy associated with uptake of clusters[28]. Hence, the wrapping process is quicker for TNBC cells than non-tumorigenic cells.

4.6. Implications

The implications of the above results are significant for the design of gold nanoparticles with favorable uptake characteristics for the specific targeting and treatment of TNBC. First, the accumulation of GNP-PEG-TRP in TNBC cells (MDA-MB-468, MDA-MB-231) is associated with the interactions between TRP and the LHRH receptors on the TNBC cells, suggests that such nanoparticles can be used to enable selective attachment to TNBC cells/tissues.

Furthermore, the thermodynamics-kinetics model for a finite cell membrane with 50 receptors per μm^2 simulate conditions of cells with less expression of LHRH receptors as observed in MCF-10A/GNP-TRP interactions. Hence, in non-tumorigenic breast cells, nanoparticle cluster wrapping time is much longer Fig.4.9. as wrapping time is limited by long-range diffusion of receptors[27], [99].

In any case, this study suggests that the unique properties of GNP-PEG-TRP can be used for the specific targeting of TNBC cells/tumors. The study also provides a fundamental basis for the design of Triptorelin functionalized PEG-coated gold nanoparticles for specific targeting of TNBC cells, with potential for the photothermal treatment of near-surface tumors. However, further work is needed to demonstrate the effectiveness of GNP-PEG-TRP for the specific targeting and the photothermal treatment of TNBC. These are some of the challenges for future work.

4.7. Conclusions

This paper presents the results of a combined theoretical and experimental study of the interaction between TNBC/non-tumorigenic breast cells and biosynthesized gold nanoparticles in (GNP), PEG-coated gold nanoparticles (GNP-PEG), and its Triptorelin functionalized forms (GNP-TRP, GNP-PEG-TRP). These were studied using confocal fluorescence microscopy and thermodynamic-kinetics models that include the surface energy effects of nanoparticle cluster uptake. The salient conclusions arising from this study are summarized below.

1. GNP-PEG-TRP preferentially enters the TNBC cells than the non-tumorigenic cells. Furthermore, the selective accumulation of GNP-PEG-TRP in TNBC is also associated with the over-expression of LHRH receptors on the surfaces of TNBC cells and the combination of PEG and TRP coatings. These enhance the selective uptake of GNP-PEG-TRP to TNBC cells.
2. The thermodynamics-kinetics model shows a critical nanoparticle cluster size for minimum wrapping time. For a finite cell membrane with conserved receptor density, cluster uptake is the number of receptors available for ligand binding and the diffusivity of such receptors. Hence, below a critical size, nanoparticle endocytosis is thermodynamically unfavorable and slow due to the rapid increase in the elastic bending energy. Alternately, when particles sizes are far above the critical size, wrapping is slow due to the diffusive nature of the receptor transport.
3. Thermodynamics-kinetics models also show that the surface energy effects of TRP functionalized gold nanoparticle clusters increase the free energy for wrapping such nanoparticle clusters.

4. The PEG coating of biosynthesized gold nanoparticles enhances uptake processes independent of the LHRH receptors. Furthermore, when PEG is used with the TRP ligand, it promotes the specificity of the GNP-PEG-TRP/ LHRH receptors interactions in TNBC. Therefore, the current results suggest that GNP-PEG-TRP nanoparticles could be suitable candidates for the specific targeting of TNBC cells that have over-expressed LHRH receptors on their surfaces.

4.8. References

[1] O. Gluz, C. Liedtke, N. Gottschalk, L. Pusztai, U. Nitz, and N. Harbeck, "Triple-negative breast cancer - Current status and future directions," Ann. Oncol., vol. 20, no. 12, pp. 1913–1927, 2009.

[2] W. J. Irvin and L. A. Carey, "What is triple-negative breast cancer ?," Eur. J. Cancer, vol. 44, no. 18, pp. 2799–2805, 2008.

[3] J. Qiu et al., "Comparison of clinicopathological features and prognosis in triple-negative and non-triple negative breast cancer," J. Cancer, vol. 7, no. 2, pp. 167-173.pdf, 2016.

[4] S. Y. Bae et al., "Poor prognosis of single hormone receptor- positive breast cancer: Similar outcome as triple-negative breast cancer," BMC Cancer, vol. 15, no. 1, pp. 1–9, 2015.

[5] Y. Pan, Y. Yuan, G. Liu, and Y. Wei, "P53 and Ki-67 as prognostic markers in triplenegative breast cancer patients," PLoS One, vol. 12, no. 2, 2017.

[6] X. Zhu et al., "The prognostic and predictive potential of Ki-67 in triple-negative breast cancer," Sci. Rep., vol. 10, no. 1, 2020.

[7] A. R. T. Bergin and S. Loi, "Triple-negative breast cancer: Recent treatment advances [version 1; peer review: 2 approved]," F1000Research, vol. 8, 2019.

[8] L. Yin, J. J. Duan, X. W. Bian, and S. C. Yu, "Triple-negative breast cancer molecular subtyping and treatment progress," Breast Cancer Res., vol. 22, no. 1, pp. 1–13, 2020.

[9] L. Y. Xia, Q. L. Hu, J. Zhang, W. Y. Xu, and X. S. Li, "Survival outcomes of neoadjuvant versus adjuvant chemotherapy in triple-negative breast cancer: A meta-analysis of 36,480 cases," World J. Surg. Oncol., vol. 18, no. 1, pp. 1–8, 2020.

[10] M. Núñez Abad et al., “Update on systemic treatment in early triple negative breast cancer,” Ther. Adv. Med. Oncol., vol. 13, 2021.

[11] W. D. Foulkes, I. E. Smith, and J. S. Reis-Filho, “Triple-Negative Breast Cancer,” 2010.

[12] S. Zhao, W.-J. Zuo, Z.-M. Shao, Y.-Z. Jiang, and Y.-Z. Jiang Fudan, “Molecular subtypes and precision treatment of triple-negative breast cancer,” Ann Transl Med, vol. 8, no. 7, p. 499, 2020.

[13] J. Collignon, L. Lousberg, H. Schroeder, and G. Jerusalem, “Triple-negative breast cancer: Treatment challenges and solutions,” Breast Cancer Targets Ther., vol. 8, pp. 93–107, 2016.

[14] S. Al-Mahmood, J. Sapiezynski, O. B. Garbuzenko, and T. Minko, “Metastatic and triple-negative breast cancer: challenges and treatment options,” Drug Deliv. Transl. Res., vol. 8, no. 5, pp. 1483–1507, 2018.

[15] M. Kalimutho, K. Parsons, D. Mittal, J. A. López, S. Srihari, and K. K. Khanna, “Targeted Therapies for Triple-Negative Breast Cancer: Combating a Stubborn Disease,” Trends in Pharmacological Sciences, vol. 36, no. 12. Elsevier Current Trends, pp. 822–846, 01-Dec-2015.

[16] J. Zhou, C. Leuschner, C. Kumar, J. Hormes, and W. O. Soboyejo, “A TEM study of functionalized magnetic nanoparticles targeting breast cancer cells,” Mater. Sci. Eng. C, vol. 26, no. 8, pp. 1451–1455, 2006.

[17] J. D. Obayemi et al., “Adhesion of ligand-conjugated biosynthesized magnetite nanoparticles to triple negative breast cancer cells,” J. Mech. Behav. Biomed. Mater., vol. 68, no. January, pp. 276–286, Apr. 2017.

[18] J. Meng, E. Paetzell, a. Bogorad, and W. O. Soboyejo, “Adhesion between peptides/antibodies and breast cancer cells,” J. Appl. Phys., vol. 107, no. 11, p. 114301, 2010.

[19] J. Hu, S. Youssefian, J. Obayemi, K. Malatesta, N. Rahbar, and W. Soboyejo, “Investigation of adhesive interactions in the specific targeting of Triptorelin-conjugated PEG-coated magnetite nanoparticles to breast cancer cells,” Acta Biomater., vol. 71, no. February, pp. 363–378, 2018.

[20] Y. Oni et al., “Gold nanoparticles for cancer detection and treatment: The role of adhesion,” J. Appl. Phisics, vol. 115, no. 084305, pp. 1–9, 2014.

[21] V. G. Abramson and I. A. Mayer, “Molecular heterogeneity of triple-negative breast cancer,” Curr. Breast Cancer Rep., vol. 6, no. 3, pp. 154–158, 2014.

[22] S. Zhang, H. Gao, and G. Bao, “Physical Principles of Nanoparticle Cellular Endocytosis,” ACS Nano, vol. 9, no. 9, pp. 8655–8671, 2015.

[23] F. Osaki, T. Kanamori, S. Sando, T. Sera, and Y. Aoyama, “A Quantum Dot Conjugated Sugar Ball and Its Cellular Uptake. On the Size Effects of Endocytosis in the Subviral Region Scheme 2. Formation of GNP and Glycovirus from 1a,” J. AM. CHEM. SOC, vol. 126, pp. 6520–6521, 2004.

[24] S. Xu, B. Z. Olenyuk, C. T. Okamoto, and S. F. Hamm-Alvarez, “Targeting receptor-mediated endocytotic pathways with nanoparticles: Rationale and advances,” Adv. Drug Deliv. Rev., vol. 65, no. 1, pp. 121–138, Jan. 2013.

[25] J. D. Obayemi et al., “Adhesion of ligand-conjugated biosynthesized magnetite nanoparticles to triple negative breast cancer cells,” J. Mech. Behav. Biomed. Mater., vol. 68, no. January, pp. 276–286, 2017.

[26] E. Hampp, R. Botah, O. Odusanya, N. Anuku, K. Malatesta, and W. Soboyejo, “Biosynthesis and adhesion of gold nanoparticles for breast cancer detection and treatment,” J. Mater. Res., vol. 27, no. 22, pp. 2891–2901, 2012.

[27] H. Gao, W. Shi, and L. B. Freund, “Mechanics of receptor-mediated endocytosis,” Proc. Natl. Acad. Sci., vol. 102, no. 27, pp. 3–8, 2005.

[28] J. Meng et al., “LHRH-functionalized superparamagnetic iron oxide nanoparticles for breast cancer targeting and contrast enhancement in MRI,” Mater. Sci. Eng. C, vol. 29, no. 4, pp. 1467–1479, 2009.

[29] J. Hu, J. D. Obayemi, K. Malatesta, A. Košmrlj, and W. O. Soboyejo, “Enhanced cellular uptake of LHRH-conjugated PEG-coated magnetite nanoparticles for specific targeting of triple negative breast cancer cells,” Mater. Sci. Eng. C, 2018.

[30] M. Deserno, “Elastic deformation of a fluid membrane upon colloid binding,” Phys. Rev. E - Stat. Nonlinear, Soft Matter Phys., vol. 69, no. 3 1, pp. 1–14, 2004.

[31] P. Decuzzi and M. Ferrari, “The role of specific and non-specific interactions in receptor-mediated endocytosis of nanoparticles,” Biomaterials, vol. 28, no. 18, pp. 2915–2922, Jan. 2007.

[32] H. Yuan, C. Huang, and S. Zhang, “Virus-Inspired Design Principles of Nanoparticle-Based Bioagents,” PLoS One, vol. 5, no. 10, p. 13495, 2010.

[33] Z. Farfel, “Receptor-mediated endocytosis,” Harefuah, vol. 116, no. 6, p. 340, 1989.

[34] S. Tzlil, M. Deserno, W. M. Gelbart, and A. Ben-Shaul, “A Statistical-Thermodynamic Model of Viral Budding,” Biophys. J., vol. 86, no. 4, pp. 2037–2048, 2004.

[35] X. Yi and H. Gao, “Kinetics of receptor-mediated endocytosis of elastic nanoparticles,” Nanoscale, vol. 9, no. 1, pp. 454–463, 2017.

[36] H. R. Kim et al., “Low-density lipoprotein receptor-mediated endocytosis of PEGylated nanoparticles in rat brain endothelial cells,” Cell. Mol. Life Sci., vol. 64, no. 3, pp. 356–364, 2007.

[37] L. B. Freund and Y. Lin, “The role of binder mobility in spontaneous adhesive contact and implications for cell adhesion,” J. Mech. Phys. Solids, vol. 52, no. 11, pp. 2455–2472, Nov. 2004.

[38] H. Yuan and S. Zhang, “Effects of particle size and ligand density on the kinetics of receptor-mediated endocytosis of nanoparticles,” Appl. Phys. Lett., vol. 96, no. 3, p. 33704, 2010.

[39] R. V Acha, F. J. Martinez-Veracoechea, and D. Frenkel, “Receptor-Mediated Endocytosis of Nanoparticles of Various Shapes,” Nano Lett, vol. 11, p. 55, 2011.

[40] P. Quinn, G. Griffiths, and G. Warren, “Density of newly synthesized plasma membrane proteins in intracellular membranes II. Biochemical studies,” J. Cell Biol., vol. 98, no. 6, pp. 2142–2147, 1984.

[41] H. Garoff and K. Simons, “Location of the spike glycoproteins in the Semliki Forest virus membrane,” Proc. Natl. Acad. Sci. U. S. A., vol. 71, no. 10, pp. 3988–3992, 1974.

[42] J. Hu, J. D. Obayemi, K. Malatesta, A. Košmrlj, and W. O. Soboyejo, “Enhanced cellular uptake of LHRH-conjugated PEG-coated magnetite nanoparticles for specific targeting of triple negative breast cancer cells,” Mater. Sci. Eng. C, vol. 88, no. March, pp. 32–45, 2018.

[43] J. Hu, J. Obayemi, K. Malatesta, E. Yurkow, D. Adler, and W. Soboyejo, “Luteinizing hormone-releasing hormone (LHRH) conjugated magnetite nanoparticles as MRI contrast agents for breast cancer imaging,” Appl. Sci., 2020.

[44] K. Kan-Dapaah, N. Rahbar, A. Tahlil, D. Crosson, N. Yao, and W. Soboyejo, “Mechanical and hyperthermic properties of magnetic nanocomposites for biomedical applications,” J. Mech. Behav. Biomed. Mater., vol. 49, no. April, pp. 118–128, 2015.

[45] K. Kan-Dapaah, N. Rahbar, and W. Soboyejo, “Implantable magnetic nanocomposites for the localized treatment of breast cancer,” J. Appl. Phys., 2014.

[46] S. . Dozie-Nwachukwu et al., “Biosynthesis of Gold Nanoparticles with Serratia marcescens Bacteria,” Adv. Mater. Res., vol. 1132, no. 19, pp. 19–35, 2016.

[47] E. L. Bentzen et al., “Surface modification to reduce nonspecific binding of quantum dots in live cell assays,” Bioconjug. Chem., vol. 16, no. 6, pp. 1488–1494, 2005.

[48] M. Zheng, F. Davidson, and X. Huang, “Ethylene glycol monolayer protected nanoparticles for eliminating nonspecific binding with biological molecules,” J. Am. Chem. Soc., vol. 125, no. 26, pp. 7790–7791, 2003.

[49] G. T. Hermanson, Bioconjugate Techniques: Third Edition. 2013.

[50] Thermo, “Thermo Scientific Pierce Crosslinking Technical Handbook,” Ebooks, 2009.

[51] D. M. Richards and R. G. Endres, “The Mechanism of Phagocytosis : Two Stages of Engulfment,” Biophysj, vol. 107, no. 7, pp. 1542–1553, 2014.

[52] H. Gao, W. Shi, and L. B. Freund, “Mechanics of receptor-mediated endocytosis,” 2005.

[53] K. Siram, S. M. Habibur Rahman, K. Balakumar, N. Duganath, R. Chandrasekar, and R. Hariprasad, Pharmaceutical nanotechnology: Brief perspective on lipid drug delivery and its current scenario. Elsevier Inc., 2019.

[54] J. S. Negi, Nanolipid Materials for Drug Delivery Systems: A Comprehensive Review. A Comprehensive Review. Elsevier Inc., 2018.

[55] F. Aqra and A. Ayyad, “Surface free energy of alkali and transition metal nanoparticles,” Appl. Surf. Sci., vol. 314, pp. 308–313, 2014.

[56] J. A. G. Briggs, T. Wilk, and S. D. Fuller, “Do lipid rafts mediate virus assembly and pseudotyping?,” Journal of General Virology, vol. 84, no. 4. pp. 757–768, 2003.

[57] A. R. Finch, L. Green, J. N. Hislop, E. Kelly, and C. A. McArdle, “Signaling and antiproliferative effects of type I and II gonadotropin-releasing hormone receptors in breast cancer cells,” J. Clin. Endocrinol. Metab., vol. 89, no. 4, pp. 1823–1832, Apr. 2004.

[58] H. Garoff, K. Simons, and L. B. Freund, “Location of the spike glycoproteins in the Semliki Forest virus membrane.,” Proc. Natl. Acad. Sci. U. S. A., vol. 71, no. 10, pp. 3988–92, Oct. 1974.

[59] S. Tzlil, M. Deserno, W. M. Gelbart, and A. Ben-Shaul, “A Statistical-Thermodynamic Model of Viral Budding,” Biophys. J., vol. 86, no. 4, pp. 2037–2048, Apr. 2004.

[60] M. Noruzi, D. Zare, and D. Davoodi, “A rapid biosynthesis route for the preparation of gold nanoparticles by aqueous extract of cypress leaves at room temperature,” Spectrochim. Acta - Part A Mol. Biomol. Spectrosc., vol. 94, pp. 84–88, 2012.

[61] C. Malarkodi, S. Rajeshkumar, M. Vanaja, K. Paulkumar, G. Gnanajobitha, and G. Annadurai, “Eco-friendly synthesis and characterization of gold nanoparticles using Klebsiella pneumoniae,” J. Nanostructure Chem., vol. 3, no. 1, pp. 1–7, 2013.

[62] N. V. Nukolova, H. S. Oberoi, Y. Zhao, V. P. Chekhonin, A. V. Kabanov, and T. K. Bronich, “LHRH-targeted nanogels as a delivery system for cisplatin to ovarian cancer,” Mol. Pharm., vol. 10, no. 10, pp. 3913–3921, 2013.

[63] P. N. Njoki et al., “Size correlation of optical and spectroscopic properties for gold nanoparticles,” J. Phys. Chem. C, vol. 111, no. 40, pp. 14664–14669, 2007.

[64] J. Gao, X. Huang, H. Liu, F. Zan, and J. Ren, “Colloidal stability of gold nanoparticles modified with thiol compounds: bioconjugation and application in cancer cell imaging.,” Langmuir, vol. 28, no. 9, pp. 4464–71, 2012.

[65] J. L. G. Wade, Organic chemistry, 7th ed., vol. 250, no. 4. 2010.

[66] R. I. Priyadharshini, G. Prasannaraj, N. Geetha, and P. Venkatachalam, “Microwave-Mediated Extracellular Synthesis of Metallic Silver and Zinc Oxide Nanoparticles Using Macro-Algae (Gracilaria edulis) Extracts and Its Anticancer Activity Against Human PC3 Cell Lines,” Appl. Biochem. Biotechnol., vol. 174, no. 8, pp. 2777–2790, 2014.

[67] L. F. Leopold et al., “Assessment of PEG and BSA-PEG gold nanoparticles cellular interaction,” Colloids Surfaces A Physicochem. Eng. Asp., vol. 532, no. July, pp. 70–76, 2017.

[68] B. Bahmani, S. Gupta, S. Upadhyayula, V. I. Vullev, and B. Anvari, “Effect of polyethylene glycol coatings on uptake of indocyanine green loaded nanocapsules by human spleen macrophages in vitro,” J. Biomed. Opt., vol. 16, no. 5, p. 051303, 2011.

[69] C. LibreTexts, “Infrared Spectroscopy Absorption Table,” 2019. [Online]. Available: https://chem.libretexts.org/Bookshelves/Ancillary_Materials/Reference/Reference_Tables/Spectroscopic_Parameters/Infrared_Spectroscopy_Absorption_Table.

[70] J. D. Obayemi et al., “Biosynthesis and the conjugation of magnetite nanoparticles with luteinizing hormone releasing hormone (LHRH).,” Mater. Sci. Eng. C. Mater. Biol. Appl., vol. 46C, pp. 482–496, 2015.

[71] S. Sigismund et al., “Clathrin-independent endocytosis of ubiquitinated cargos,” Proc. Natl. Acad. Sci. U. S. A., vol. 102, no. 8, pp. 2760–2765, 2005.

[72] S. Mayor, R. G. Parton, and J. G. Donaldson, “Clathrin-independent pathways of endocytosis,” Cold Spring Harb. Perspect. Biol., vol. 6, no. 6, 2014.

[73] J. J. Rennick, A. P. R. Johnston, and R. G. Parton, “Key principles and methods for studying the endocytosis of biological and nanoparticle therapeutics,” Nature Nanotechnology, vol. 16, no. 3. pp. 266–276, 2021.

[74] T. G. Iversen, T. Skotland, and K. Sandvig, “Endocytosis and intracellular transport of nanoparticles: Present knowledge and need for future studies,” Nano Today, vol. 6, no. 2, pp. 176–185, Apr. 2011.

[75] L. M. Bareford and P. W. Swaan, “Endocytic mechanisms for targeted drug delivery,” Adv. Drug Deliv. Rev., vol. 59, no. 8, pp. 748–758, 2007.

[76] D. Holec, P. Dumitraschkewitz, D. Vollath, and F. D. Fischer, “Surface energy of au nanoparticles depending on their size and shape,” Nanomaterials, vol. 10, no. 3, 2020.

[77] D. Vollath, F. D. Fischer, and D. Holec, “Surface energy of nanoparticles-influence of particle size and structure,” Beilstein J. Nanotechnol, vol. 9, pp. 2265–2276, 2018.

[78] H. H. Chen et al., “Quantitative analysis of nanoparticle internalization in mammalian cells by high resolution X-ray microscopy,” J Nanobiotechnology, vol. 9, p. 14, 2011.

[79] L. Shang et al., “Nanoparticle interactions with live cells: Quantitative fluorescence microscopy of nanoparticle size effects,” Beilstein J. Nanotechnol., vol. 5, no. 1, pp. 2388–2397, 2014.

[80] C. M. Maguire, M. Rösslein, P. Wick, and A. Prina-Mello, “Characterisation of particles in solution–a perspective on light scattering and comparative technologies,” Science and Technology of Advanced Materials. 2018.

[81] B. J. Inkson, “Scanning electron microscopy (SEM) and transmission electron microscopy (TEM) for materials characterization,” Mater. Charact. Using Nondestruct. Eval. Methods, pp. 17–43, Jan. 2016.

[82] V. V. Nemoshkalenko and V. G. Aleshin, Physical Principles of Electron Spectroscopy. 1979.

[83] M. Danaei et al., “Impact of particle size and polydispersity index on the clinical applications of lipidic nanocarrier systems,” Pharmaceutics, vol. 10, no. 2, pp. 1–17, 2018.

[84] J. B. Pawley, “Fundamental limits in confocal microscopy,” Handb. Biol. Confocal Microsc. Third Ed., pp. 20–42, 2006.

[85] A. D. Elliott, “Confocal Microscopy: Principles and Modern Practices,” Curr. Protoc. Cytom., vol. 92, no. 1, 2020.

[86] E. V YoungLai and E. C. Todoroff, “The pituitary gonadotropin-releasing hormone (GnRH) receptor of the female rabbit: characterization and developmental aspects.,” Can. J. Physiol. Pharmacol., vol. 70, no. 12, pp. 1639–1646, Dec. 1992.

[87] K. Xiao et al., “LHRH-Targeted Redox-Responsive Crosslinked Micelles Impart Selective Drug Delivery and Effective Chemotherapy in Triple-Negative Breast Cancer,” Adv. Healthc. Mater., vol. 10, no. 3, 2021.

[88] S. S. Kakar, H. Jin, B. Hong, J. W. Eaton, and K. A. Kang, “LHRH receptor targeted therapy for breast cancer,” Adv. Exp. Med. Biol., vol. 614, pp. 285–296, 2008.

[89] J. B. Engel and A. V. Schally, “Drug insight: Clinical use of agonists and antagonists of luteinizing-hormone-releasing hormone,” Nat. Clin. Pract. Endocrinol. Metab., vol. 3, no. 2, pp. 157–167, 2007.

[90] C. W. Kwok, O. Treeck, S. Buchholz, S. Seitz, O. Ortmann, and J. B. Engel, “Receptors for luteinizing hormone-releasing hormone (GnRH) as therapeutic targets in triple negative breast cancers (TNBC),” Target. Oncol., vol. 10, no. 3, pp. 365–373, 2015.

[91] S. Seitz et al., “Triple negative breast cancers express receptors for LHRH and are potential therapeutic targets for cytotoxic LHRH-analogs, AEZS 108 and AEZS 125,” 2014.

[92] S. Buchholz et al., “Triple-negative breast cancers express receptors for luteinizing hormone-releasing hormone (LHRH) and respond to LHRH antagonist Cetrorelix with growth inhibition,” Int. J. Oncol., vol. 35, pp. 789–796, 2009.

[93] A. M. Bajo, A. V Schally, and G. Halmos, “Targeted Doxorubicin-containing Luteinizing Hormone-releasing Hormone Analogue AN-152 Inhibits the Growth of Doxorubicin-resistant MX-1 Human Breast Cancers Targeted Doxorubicin-containing Luteinizing Hormone-releasing Hormone Analogue AN-152 Inhibits the,” Clin. Cancer Res., vol. 9, pp. 3742–3748, 2003.

[94] C. Gründker, C. Föst, S. Fister, N. Nolte, A. R. Günthert, and G. Emons, “Gonadotropin-releasing hormone type II antagonist induces apoptosis in MCF-7 and triple-negative MDA-MB-231 human breast cancer cells in vitro and in vivo,” Breast Cancer Res., vol. 12, no. 4, 2010.

[95] C. Föst, F. Duwe, M. Hellriegel, S. Schweyer, G. Emons, and C. Gründker, “Targeted chemotherapy for triple-negative breast cancers via LHRH receptor,” Oncol. Rep., vol. 25, no. 5, pp. 1481–1487, 2011.

[96] A. Chen, S. Rahimipour, N. Ben-Aroya, Y. Koch, E. Kaganovsky, and E. Okon, “Two forms of gonadotropin-releasing hormone (GnRH) are expressed in human breast tissue and overexpressed in breast cancer: A putative mechanism for the antiproliferative effect of GnRH by down-regulation of acidic ribosomal phosphoproteins P1 and P2,” Cancer Res., vol. 62, no. 4, pp. 1036–1044, 2002.

[97] N. Barabutis and A. V. Schally, “Knocking down gene expression for growth hormone-releasing hormone inhibits proliferation of human cancer cell lines,” Br. J. Cancer, vol. 98, no. 11, pp. 1790–1796, 2008.

[98] S. Bellyei, A. V. Schally, M. Zarandi, J. L. Varga, I. Vidaurre, and E. Pozsgai, “GHRH antagonists reduce the invasive and metastatic potential of human cancer cell lines in vitro,” Cancer Lett., vol. 293, no. 1, pp. 31–40, 2010.

[99] S. Zhang, H. Gao, and G. Bao, “Physical Principles of Nanoparticle Cellular Endocytosis,” ACS Nano, vol. 9, no. 9, pp. 8655–8671, 2015.

Chapter 5.0. Biosynthesized Gold Nanoparticles for Photothermal Treatment of Triple Negative Breast Cancer: Effects of Nanoparticle Functionalization on Phothothermal Efficiency

5.1. Introduction

Although there has been an increase in treatment response rates among breast cancer patients, various clinical and pathological studies report that over 50% of triple negative breast cancer TNBC patients do not benefit from the available endocrine chemotherapy treatments because TNBC does not overexpress any of the three primary breast tumor markers: progesterone, estrogen, and human epidermal growth factor 2 (HER2) [1]–[11]. Hence, TNBC progression is aggressive with a poor prognosis.

The clinical use of heat for cancer therapeutics, including breast cancer, has received significant attention due to its minimal side effects, flexible treatment regime, and potential to enhance the therapeutic efficacy of conventional cancer therapies even at sublethal temperatures[12]–[18].

The thermal doses can be classified into High-temperature ablation doses (50 to 100ºC) that cause necrosis in tumor cells or mid-range hyperthermia doses of 40 to 45 ºC that induce apoptosis in tumor cells[12], [15], [17]–[22]

Although the current clinical hyperthermia-assisted cancer therapeutics have their merits, many of the thermometry processes involved are invasive[12], [13]. Secondly, these devices are often plagued by biocompatibility and corrosion issues that detract from long-term use[13], [23], [24].

Also, clinical hyperthermia processes are often limited by non-uniform heat distribution within tumor tissues and the difficulty of localizing heating[13], [25]–[27]. These limitations to clinical hyperthermia necessitate the need for novel photothermal strategies.

Interestingly, the use of nanoparticles in cancer therapeutics has emerged as a possible solution to the current clinical hyperthermia shortcomings. Specifically, their ability to serve as photothermal agents and localize heat within a tumor region is of great interest for cancer treatment. Additionally, the ability to actively target cancer tumors with ligand functionalized nanoparticles proves advantageous for the localization of nanoparticles within malignant tumors.

Some examples of nanoparticles explored for their heating properties include small photoactive molecules (SPM) such as cyanines and porphyrins, carbon-based nanomaterials such as graphene and carbon nanotubes, quantum dots, polymeric, and metallic nanoparticles[28], [29]. These particles can be tuned to achieve high light to heat conversion efficiency and high surface to volume ratio or enhance imaging contrast. Still, low aqueous solubility, poor stability, photobleaching, toxicity, and biocompatibility hinder their long-term use.

Gold nanoparticles are among the most studied metallic nanoparticles. Gold nanoparticles have received much attention because of their plasmonic properties. Mainly, gold nanoparticles are able to convert the energy from an incident of NIR light into heat and induce hyperthermia [28], [30]–[33]. This property is particularly significant because laser light in the NIR region (700–1100 nm) enhances higher penetration depth and lower absorption in biological tissues. In addition, NIR laser wavelength limits the non-specific heating of healthy tissues[18], [34]. However, chemically synthesized gold nanoparticles are often associated with toxicities from the synthesis, which may persist even after the polymer coating of these nanoparticles[34], [35].

Our group has studied the photothermal effects of magnetite and gold nanocomposites to mitigate biocompatibility and corrosion issues common with metallic implants. This study was done by fabricating nanocomposites using plasmonic nanomaterials with polymer matrices[13], [27], [36]. In these studies, we unraveled new insights into the decline in MDA-MB-231 cell viability due to the photothermal effects of these polymeric composite devices in TNBC MDA-MB-231 cells.

In this article, we present the photothermal effects of biosynthesized gold nanoparticles modified with PEG coatings and Triptorelin (TRP) ligand that targets LHRH receptors overexpressed on the surfaces of TNBC.

We provide insights into the hyperthermia (41ºC - 45ºC) NIR laser interactions with biosynthesized gold nanoparticles in the in invitro and tissue model. In addition, we examine the effects of various robotics for medical laser-nanoparticle hyperthermia applications. Subsequently, results from the laser-nanoparticle interactions were validated using finite element analysis (FEA).

Finally, the implications of the results are discussed for the design of triptorelin-conjugated, PEG-coated biosynthesized gold nanoparticles for specific targeting of triple-negative breast cancer cells and localized laser-assisted photothermal treatment.

5.2. Materials and Experimental Methods

5.2.1. Gold Nanoparticles Synthesis and Characterization

The gold nanoparticles (GNP) were biosynthesized from processes adapted from a prior study done by our group[37]. Gold (III) Chloride Trihydrate (ACS reagent with ≥49.0% Au basis Sigma-Aldrich, St. Louis, USA) was reduced intracellularly and extracellularly using a cell-free extract of Serratia Marcescens bacteria [37]. Briefly, 5g of Proteose peptone (Sigma-Aldrich, St. Louis, USA) and 10 mL of glycerol (Sigma-Aldrich, St. Louis, USA) was dissolved in 1L of water. The resulting solution was autoclaved for 55 minutes before inoculation with Serratia Marcescens. Subsequently, the autoclaved and inoculated solution was kept in an incubator shaker that was vibrated at 90 rpm at a temperature of 32^oC for 48 hrs. The resulting bacteria culture was centrifuged at 4000 rpm for 15 minutes, and the bacteria cell-free extract was collected into flasks and stored in a refrigerator at 4^oC. Next, 20 mL of the cell-free extract and 20 mL of a 2.5 mM Tetra-chloroauric solution were added to a 50 mL Falcon centrifuge tube and incubated in a water bath at 30^oC for 1 day.

The Biosynthesized Gold Nanoparticles (GNP) obtained were treated in 1% sodium dodecyl sulfate (SDS) (ACS reagent with ≥99.0% Sigma-Aldrich, St. Louis, USA) [38] to denature the surface-bound proteins and heated at 95^{o}C for 30 mins in a vacuum oven. They were then washed three times in Dulbecco Phosphate Buffer Saline (DPBS) (Life technologies cooperation, Carlsbad, CA) buffer for 15 mins in a centrifuge at 4000 rpm and twice in deionized water.

Following this, BGNPs were concentrated using a centrifugal filter (Amicon Ultra-15, Millipore Billerica, MA) and then re-dissolved in 1 mL of Deionized, Distilled water.

Subsequently, GNP was PEG-coated using methyl-PEG$_4$-thiol (MT(PEG)$_4$) and carboxy-PEG$_{12}$-thiol (CT(PEG)$_{12}$) (Thermo Fisher Scientific, Inc. Waltham, MA, USA). Notably, (MT(PEG)$_4$) and (CT(PEG)$_{12}$) were used in combination to reduce non-specific protein binding to the nanoparticle surface [39], [40]. A solution of MT(PEG)$_4$ (0.5 mM, 4 mL) and CT(PEG)$_{12}$ (0.5 mM, 4 mL) were added to 10 mL of GNP (0.2 mM) and stirred for 2 h at room temperature. Next, the mixture was washed with Dulbecco Phosphate Buffer Saline (DPBS) (Life technologies cooperation, Carlsbad, CA) buffer and centrifuged in a spin column with a molecular weight cut-off of 50 kDa. Lastly, the PEG-coated GNPs were resuspended in deionized water.

The bare GNP and PEG-coated GNP (GNP-PEG) were modified by the ligand conjugation with triptorelin (D-Trp LHRH)(BACHEM, Torrance, CA, USA) using a carbodiimide activation process with ethyl (dimethyl aminopropyl) carbodiimide (EDC) (Sigma-Aldrich, St. Louis, MO, USA) and N-hydroxysuccinimide (NHS) (Thermo Fisher Scientific, Inc., Waltham, MA, USA)[41][42]. Specifically, a solution of EDC (13.5 mM, 74µL) and NHS (15.3 mM, 65 µL) was added to GNP and GNP-PEG (0.2 mM, 5 mL) and stirred continuously for 2 hours at room temperature before triptorelin ligand (TRP) (5 mM, 192 µL) was added and stirred overnight. After TRP conjugation of GNP (GNP-TRP) and PEG-coated GNP(GNP-PEG-TRP), the mixture was washed with DPBS, then centrifuged in a spin column with a molecular weight cut-off of 50 kDa. Lastly, GNP-TRP and GNP-PEG-TRP were resuspended in deionized water.

Finally, the hydrodynamic diameter and zeta potentials of GNP, GNP-TRP, GNP-PEG, and GNP-PEG-TRP in distilled water were measured using the Malvern Zetasizer (Westborough, MA, USA).

5.2.2. Photothermal Effects of Laser /Gold Nanoparticle Interactions

The photothermal interactions between each gold nanoparticle (GNP, GNP-TRP, GNP-PEG, and GNP-PEG-TRP) and a continuous near-infrared (808nm) laser (Photon Soft Tissue Diode Laser, Zolar Technology & MFG, Canada) was conducted as shown in Fig.5.2. The gold nanoparticle/laser interactions in fluidic environments were idealized using water as a reference fluid, while chicken tissue approximated the photothermal interactions in human breast tissue. Hyperthermia treatments, cell viability studies, and heat shock protein expression were also done on MDA-MB-231 TNBC cells.

5.2.2.1. Laser Interactions with Gold Nanoparticles Dispersed in Water

The experimental setup for the laser/gold nanoparticle interactions in water is shown in Fig.5.1. Specifically, 1mL (1.19 mg/mL) of each nanoparticle sample (GNP, GNP-PEG, GNP-TRP, and GNP-PEG-TRP) was placed in a polystyrene cuvette and positioned as shown in Fig.5.1. These samples were exposed to a near-infrared continuous laser of 0.9, 2, and 3W, with a spot size of 1cm for 20 mins. The temperature variations with time were recorded at one-minute intervals with a Forward-Looking Infrared (FLIR) camera (InfraTec InfraRed LLC Plano Tx, USA). Each experiment was performed in triplicate on both experimental and control samples (distilled water) using the same conditions.

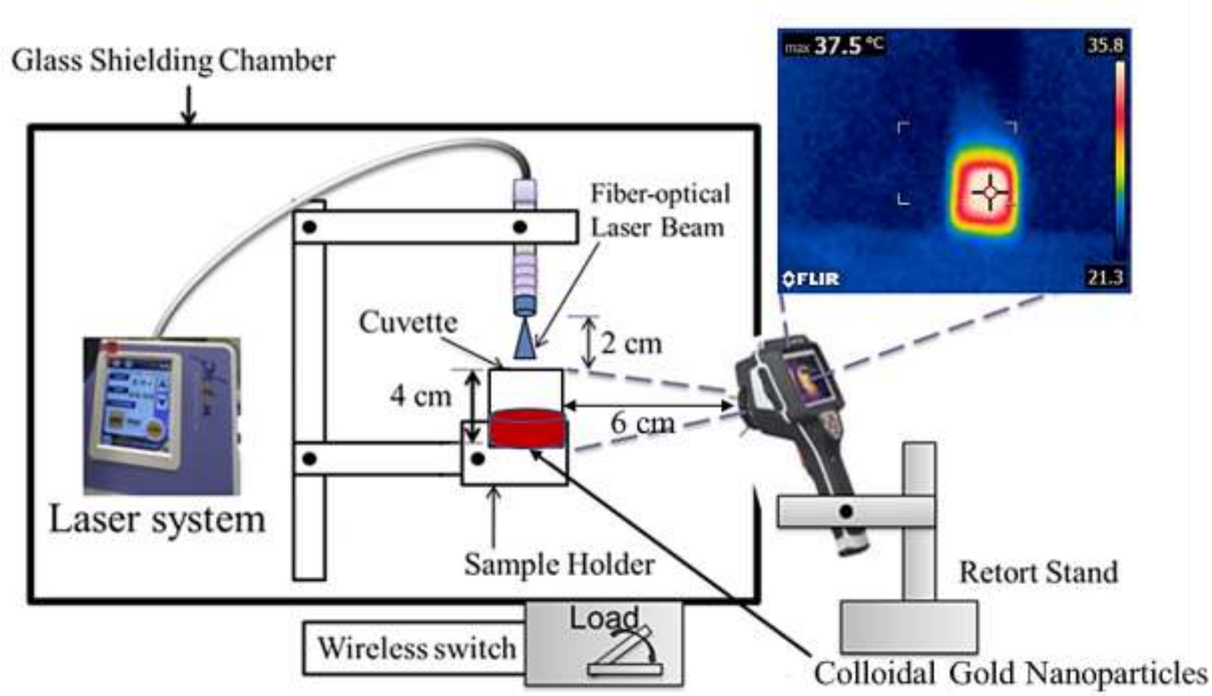

Fig.5.1. A schematic showing the heating setup for an 808 nm NIR laser interacting with colloidal gold nanoparticles. It depicts typical temperature distribution profiles captured by Forward-looking Infrared (FLIR) camera.

5.2.2.2. In vitro Hyperthermia Treatment of TNBC Cells

The effects of laser-induced hyperthermic heating treatment (41º - 45º C) on MDA-MB-231 cells were studied using GNP (cells$_{@\ 41\text{-}45^{\circ}\ \mathrm{C\ with\ GNP}}$), GNP-PEG (cells$_{@\ 41\text{-}45^{\circ}\ \mathrm{C\ with\ GNP\text{-}PEG}}$), GNP-TRP (cells$_{@\ 41\text{-}45^{\circ}\ \mathrm{C\ with\ GNP\text{-}TRP}}$), and GNP-PEG-TRP (cells$_{@\ 41\text{-}45^{\circ}\ \mathrm{C\ with\ GNP\text{-}PEG\text{-}TRP}}$) nanoparticles as photothermal agents. Control samples of untreated MDA-MB-231 cells, which were not exposed laser light or nanoparticles (cells$_{@\ 37^{\circ}\ \mathrm{C\ untreated}}$), MDA-MB-231 cells which were exposed to laser light but no nanoparticles (cells$_{@\ 37^{\circ}\ \mathrm{C\ with\ laser\ only}}$) and cells exposed to only nanoparticles without laser interactions (cells$_{@\ 37^{\circ}\ \mathrm{C\ with\ GNP\ only}}$, cells$_{@\ 37^{\circ}\ \mathrm{C\ with\ GNP\text{-}TRP\ only}}$, cells$_{@\ 37^{\circ}\ \mathrm{C\ with\ GNP\text{-}TRP\ only}}$, cells$_{@\ 37^{\circ}\ \mathrm{C\ with\ GNP\text{-}PEG\text{-}TRP\ only}}$) were monitored under the same conditions. Laser-induced heating of the cells was carried out in a class II biosafety cabinet to prevent external contamination of MDA-MB-231 cells. 1mL of MDA-MB-231 cells containing 1×10^5 cells/mL and 1.8 mg/mL of each nanoparticle (GNP, GNP-PEG, GNP-TRP, and GNP-PEG-TRP) suspended in Leibnitz cell culture media was placed in a cuvette positioned as shown in Fig. 5.1 These samples were exposed to a near-infrared continuous laser of 808 nm wavelength (Photon Soft Tissue Diode Laser, Zolar Technology & MFG, Canada), a laser spot size of 1cm at 0.7 W power for 20 mins. After hyperthermic heating, experimental samples were placed in an incubator for 12hrs at 37ºC under normal atmospheric conditions to allow stress relaxation from treatment before carrying out cell viability and human heat shock protein 70 (HSP70) expression studies. The temperature variations with time were recorded every minute with an FLIR camera. All hyperthermia treatment studies were performed in triplicate on experimental and control samples.

5.2.2.3. Cell Viability Study of Heat Treated TNBC Cells Using Alamar Blue Assay

The cell viability of experimental (cells$_{\text{@ 41-45º C with GNP}}$, cells$_{\text{@ 41-45º C with GNP-PEG}}$, cells$_{\text{@ 41-45º C with GNP-TRP}}$, and cells$_{\text{@ 41-45º C with GNP-PEG-TRP}}$) and control samples (cells$_{\text{@ 37º C untreated}}$, cells$_{\text{@ 37º C with laser only}}$, cells$_{\text{@ 37º C with GNP only}}$, cells$_{\text{@ 37º C with GNP-TRP only}}$,cells$_{\text{@ 37º C with GNP-TRP only}}$, and cells$_{\text{@ 37º C with GNP-PEG-TRP only}}$) were studied using Alamar blue assay, to measure metabolic activity of the cells. After the 12h incubation/rest period, 1mL of experimental and control samples were seeded in 24-well plates. The seeded cells were allowed a 3h attachment window. Subsequently, the original cell media/nanoparticle mixture was replaced with 1 mL of 10% Alamar Blue reagent (Thermo Fisher Scientific, Waltham, MA, USA) prepared in Leibnitz cell culture media. The 24-well plates were incubated at 37 °C under normal atmospheric conditions for 3 h.

After 3h, 100 µL aliquots were transferred from the 24-well plates into a black opaque 96-well plate (Thermo Fisher Scientific, Waltham, MA, USA) in triplicate. The fluorescence intensities of all Alamar blue samples were measured at 544 nm excitation and 590 nm emission using a 1420 Victor3 multilabel plate reader (Perkin Elmer, Waltham, MA, USA). In addition, the percentage of Alamar blue reduction (normalized) was determined using Alamar blue assay and cell viability study protocols [43].

5.2.2.4. Expression of Heat Shock Protein 70 (HSP70) in Heat Treated TNBC

The expression of HSP70 in experimental ($\text{cells}_{@\ 41\text{-}45^{\circ}\text{ C with GNP}}$, $\text{cells}_{@\ 41\text{-}45^{\circ}\text{ C with GNP-PEG}}$, $\text{cells}_{@\ 41\text{-}45^{\circ}\text{ C with GNP-TRP}}$, and $\text{cells}_{@\ 41\text{-}45^{\circ}\text{ C with GNP-PEG-TRP}}$) and control samples ($\text{cells}_{@\ 37^{\circ}\text{ C untreated}}$, $\text{cells}_{@\ 37^{\circ}\text{ C with laser only}}$) were studied using enzyme-linked immunosorbent sandwich assays (ELISA) (Thermo Fisher Scientific, Waltham, MA, USA). After the 12h stress relaxation period, Leibnitz cell culture media/nanoparticle supernatant was collected from all MDA-MB-231 cell samples and analyzed according to the ELISA kit manufacturer's instructions. HSP70 concentrations were determined in relation to the HSP70 standard curve plotted according to the manufacturer's instructions. All ELISA studies were analyzed in triplicates, and the absorbance was measured at 490nm using a 1420 Victor3 multilabel plate reader.

5.2.3.5. Live/Dead Cell Double Fluorescence Staining of Heat-treated TNBC Cells

After the 12h stress relaxation period, a Live/Dead double staining kit (Sigma-Aldrich) containing Calcein-AM and Propidium Iodide (PI) solutions were used in the simultaneous fluorescence staining of viable and dead cells, respectively.

The assay solution was prepared by adding 10 µL of solution A and 5 µL of solution B to 5 mL of DPBS. The experimental and control samples were centrifuged at 900 rpm for 5 mins, excess media aspirated, and washed in DPBS several times to remove residual esterase activity. Next, 100 µl of the assay solution was added to a 1x10^5 cells/mL suspension from all samples and incubated at 37 ºC under normal atmospheric conditions for 15 min. Finally, samples were placed on glass slides and imaged with an Eclipse Nikon Ts2R-FL inverted fluorescence microscope coupled to a Nikon DS-Fi3 camera (Nikon Instrument, Inc., Melville, NY) with 10 and 20 X objectives at 490 nm excitation for monitoring of viable and dead cells (545 nm excitation).

5.2.3. Laser Interactions with Gold Nanoparticles in Chicken Tissue

The gold nanoparticle/laser interactions in chicken tissue and the ensuing temperature distribution profile within the chicken tissue were investigated using stationary laser support as shown in Fig.4.2, a modified fusion deposition modeling (FDM) 3D printer nozzle (Ender 3 pro, Creality3D Technology Co. Ltd, Shenzhen, China) performing raster motion along the XY axis and height modulation along the Z-axis also a universal robot UR5 (Universal Robots Odense, Denmark) positioning arm with a six (6) degrees of freedom was used to introduce angular variations in the laser interactions with the nanoparticles.

5.2.3.1. Stationary Laser Source Interaction with Gold Nanoparticles in Chicken Tissue

For the stationary laser source interaction with gold nanoparticles in chicken tissue, a 10mm x 10mm x 6mm incision was made in chicken tissue. 40 µL (11.4 mg/mL) of each gold nanoparticle sample (GNP, GNP-PEG, GNP-TRP, and GNP-PEG-TRP) was placed in the groove made in the chicken as the bottom layer and covered with the excavated chicken tissue (middle layer). The incised groove was then covered with a 2 mm top layer of chicken skin, as shown in the depth profile of the groove in Fig. 5.2b. The entire chicken/nanoparticle setup was maintained at 37º C and then heated with a perpendicular stationary laser source for 20 mins at 3W using the same design in Fig. 5.1. The temperature variations with time and temperature and heat distribution across the chicken tissue were recorded with an FLIR camera. Each experiment was performed in triplicate and on a control sample (chicken groove without nanoparticles) using the same experimental conditions.

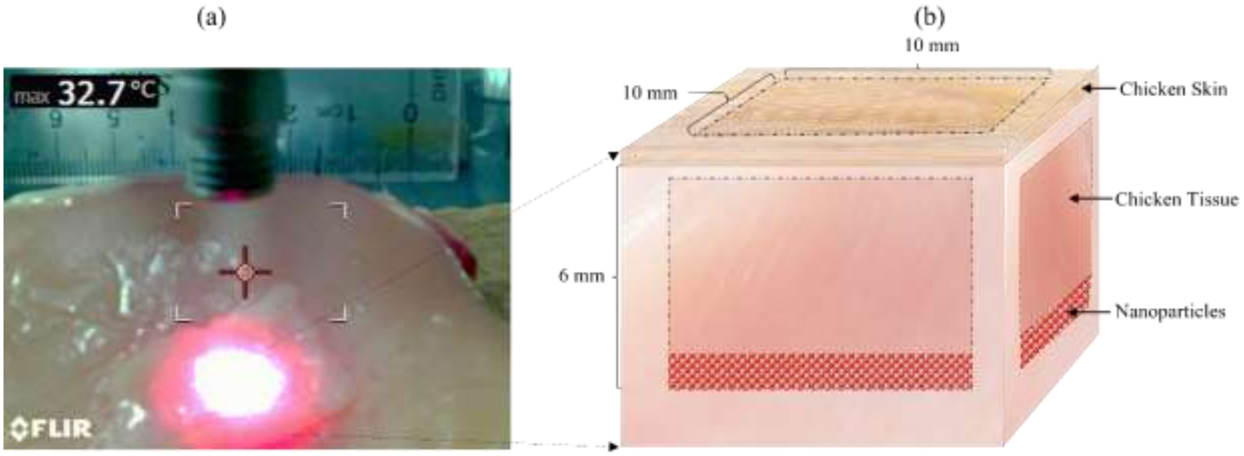

Fig.5.2. (a) A Forward-looking Infrared (FLIR) image of a 3W laser interaction with gold nanoparticles placed within a groove in the chicken tissue (b)showing the depth profile of the incised 10mm x 10 mm x 6mm groove with a bottom layer of gold nanoparticles, mid-layer of excavated chicken flesh, and a top layer of chicken skin with a thickness of 2mm.

5.2.3.2. 3D Printer Controlled Laser Source Interaction with Gold Nanoparticles in Chicken Tissue

The laser source was controlled by a repurposed FDM 3D printer with the nozzle replaced with the laser handpiece. A 3D CAD design of a cylindrical sample (10 mm diameter x 5 mm thickness) was made using Autodesk Fusion 360 to generate a movement pattern for the laser handpiece around the area of interest. The CAD design was then imported into Ultimaker Cura software and the desired printer settings (nozzle head direction x, y, z, print speed of 5mm/s, and build shape were set. In this study we designed a cylindrical sample (diameter 5mm, thickness 5mm), layer height of 0.05mm and 20% infill). Subsequently, a G-code was generated from the slicing of the cylindrical object. The sliced G-code was then used to simulate a printing pattern for the cylindrical sample around the groove. The printer bed was maintained at 37ºC and laser positioned 2 cm above the chicken. The dimensions of the incised groove, nanoparticle concentration, heating time, and laser power were maintained as described in the stationary laser source design in section 5.2.3.1. The temperature variations with time and temperature distribution across the chicken tissue were recorded with an FLIR camera as the modified 3D printer head scanned in a raster pattern. Each experiment was performed in triplicate and on a control sample (chicken groove without nanoparticles) using the same experimental conditions.

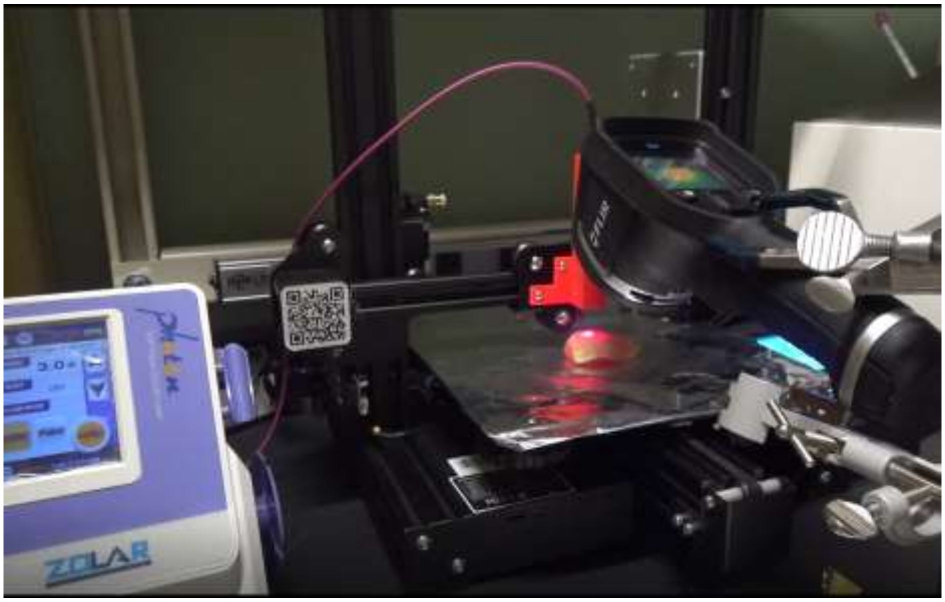

Fig.5.3. Laser heating design showings the modified 3D printer nozzle positioning of the NIR laser. It depicts a typical capture of the temperature distribution profiles captured by an FLIR camera.

5.2.3.3. Robotic-Arm Controlled Laser Source Interaction with Gold Nanoparticles in Chicken Tissue

Next, the laser source was positioned by a UR5 universal robot arm with an adaptive gripper. The path of motion for the arm was programmed using the accompanying polyscope graphical user interface. The robotic arm was programmed to perform a 20 min loop of one angular (45º) rotation along the 6-way paths followed by an orthogonal raster pattern on the chicken surface at a speed of 0.47 m/s. The dimensions of the incised groove, nanoparticle concentration, heating time, and laser power were maintained as described in the stationary laser source section 5.2.3.1. The temperature variations with time and temperature distribution across the chicken tissue were recorded with an FLIR camera. Each experiment was performed in triplicate and on a control sample (chicken groove without nanoparticles) using the same experimental conditions.

5.2.4. Statistical Analysis

The results are presented as mean ± standard deviation for n =3 (unless otherwise stated). One-way ANOVA with post hoc Tukey HSD multiple comparisons tests was used to analyze the differences between the MDA-MB-231 cell viabilities via % Alamar blue reduction (normalized) and HSP70 concentrations under different gold nanoparticle/ laser treatments. The statistical analyses were done using IBM SPSS Statistics 28 software with the statistical differences between means considered significant at $p < 0.05$.

5.3. Modeling Photothermal Effects of Laser /Gold Nanoparticle Interactions

Finite element analyses (FEA) on the laser/media interactions were performed using the commercial software Abaqus for different laser powers and the different nanoparticles to numerically study the photothermal behavior of gold nanoparticles (GNP, GNP-PEG, GNP-TRP, GNP-PEG-TRP) in a fluid media. If the scattering process dominates absorption, then the optical diffusion approximation can be used to obtain the light fluence rate $\varphi(\vec{\mathrm{r}})(\frac{\mathrm{W}}{\mathrm{m}^2})$ within the media for a continuous wave Gaussian laser beam incident [44].

$$\varphi(\vec{\mathrm{r}}) = \frac{\mathrm{P}_0 \exp{(-\mu_{\mathrm{eff}} \vec{\mathrm{r}}.\hat{\mathrm{n}})}}{4\pi \mathrm{Dr}} \tag{5.1}$$

where $\vec{r}$ is the position vector, P_0 is the laser power, and $\hat{n}$ is the normal vector showing the direction in which the laser beam travels, μ_{eff} and D are the effective attenuation coefficient and the diffusion coefficient of the medium, respectively, which are defined as:

$$\mu\_(\mathrm{eff}\ ) = \surd(3\mu\_\mathrm{a}\ (\mu\_\mathrm{a} + \mu\_\mathrm{s}\text{^}')) \tag{5.2}$$

$$\mathrm{D} = \frac{1}{3(\mu_\mathrm{s}' + \mu_\mathrm{a})} \tag{5.3}$$

in which μ_a is the absorption coefficient and μ_s' is the reduced scattering coefficient which can be defined as:

$$\mu_\mathrm{s}' = (1 - \mathrm{g})\ \mu_\mathrm{s} \tag{5.4}$$

where μ_s is the scattering coefficient and g is the anisotropy factor. Table 5.1 shows the parameters used in this study.

Table 5.1 Absorption coefficient μ_a of GNP, GNP-PEG, GNP-TRP, and GNP-PEG-TRP in water.

Nanoparticles	**GNP**	**GNP-PEG**	**GNP-TRP**	**GNP-PEG-TRP**
$\boldsymbol{\mu_{\mathrm{a}_{\mathrm{water}}}}$	0.275	0.262	0.259	0.251

The heat diffusion equation is used to obtain the heat distribution within the device and surrounding media:

$$\rho C \frac{\partial T(\vec{r},t)}{\partial t} = \nabla . [\kappa \nabla T(\vec{r},t)] + Q, \tag{5.5}$$

where ρ ($\frac{kg}{m^3}$) is the density, κ ($\frac{W}{mK}$) is the thermal conductivity, C ($\frac{J}{kg\,K}$) is the specific heat. Q ($\frac{W}{m^3}$) is the heat source which is obtained as:

$$Q(\vec{r},t) = \mu_{a_{media}} \varphi(\vec{r},t) \tag{5.6}$$

At the boundary between the surface of the media and air, Robin boundary condition is considered to solve the equation (5) as follows:

$$-\kappa \frac{\partial T(\vec{r},t)}{\partial t} = h(T_s - T_\infty) \tag{5.7}$$

where h $\left(\frac{W}{m^2K}\right)$ is the heat convection coefficient, and T_s and T_∞ are temperature at the surface exposed to air and the ambient temperature, respectively.

Subsequently, 3D models of the media with the dimension of 1 cm were created in Abaqus. Standard 8 node linear heat transfer elements were used to mesh the geometry. Additionally, heat convection is modeled by considering surface film condition (with temperature-dependent film coefficient), and uniform sink temperature equal to $25^\circ C$ in the boundaries of the media. The values of the film coefficient were chosen to ensure the best agreement between the numerical and experimental results. The film coefficient for the top surface is considered 2.1 times the side surfaces to model the higher heat convection from the open surface. Heat convection is considered to linearly vary as a function of the power based on experimental observations. (i.e., film coefficients for the side surfaces are considered $14\ \left(\frac{W}{m^2K}\right)$ for P = 0.9 W and $28\ \left(\frac{W}{m^2K}\right)$ for P = 3 W). The initial temperature of the media is $37^{\circ}C$. The transient heat transfer step is applied to solve the problem for 20 minutes. The model is run for laser powers of 0.9 W, 2 W, and 3 W for media with the different gold nanoparticles in water with C = 4180 J/kgK, κ = 0.606 W/mK, and ρ = 997 Kg/$m^{3,}$ and the average temperature of all nodes within the media is calculated.

5.4. Photothermal Efficiencies of Biosynthesized Gold Nanoparticles

To calculate the photothermal conversion efficiency, Eq. (5.8) describes the nanoparticle heat generation and heat dissipation in a polystyrene (PS)cuvette ($1.2 \times 1.2 \times 4.5$ cm^3). Under NIR (808nm) illumination, the change in temperature T is described by the energy balance equation[45].

$$\sum_i m_i C_i \frac{dT}{dt} = E_{abs} - E_{loss} \tag{5.8}$$

where E_{abs} is the heat-induced by the absorption of the nanoparticles, E_{loss} is the heat dissipated through the surrounding media, t is the time, m_i and C_i are the mass and specific heat capacities of each element i in the system (i.e., nanoparticles, deionized water, and PS cuvette). For the four gold nanoparticle dispersions investigated, the mass of GNP, GNP-PEG, GNP-TRP, and GNP-PEG-TRP was negligible compared to the mass of deionized water (1 g) and the PS cuvette (2.2 g). Also, the heat capacity of gold (0.126 J/gK) is much smaller than that of water (4.18 J/gK) and PS (1.3 J/gK). Thus, the mass and heat capacity of the entire gold nanoparticle dispersion can be assumed to be that of water and the PS cuvette. The absorption and dissipation energy in Eq. (5.8) can be expressed as follows:

$$\mathrm{E_{abs}} = \mathrm{P}(1 - 10^{-\mathrm{A}\lambda})\eta, \tag{5.9}$$

$$\mathrm{E_{loss}} = hS[T(t) - T_0] \tag{5.10}$$

where P is the incident 808 nm NIR continuous-wave laser power, Aλ is the absorbance value of the nanoparticles at the excitation wavelength of the laser, η is the photothermal efficiency, h is the heat transfer coefficient, S is the surface covered by the gold nanoparticle dispersions, and T_0 is the ambient temperature. Table 5.2 shows the Aλ values used in this estimation.

Eq. (5.8) can be rewritten as follows:

$$\frac{\mathrm{dT}}{\mathrm{dt}} = \frac{\mathrm{P}(1-10^{-\mathrm{A}\lambda})\eta}{\sum_{\mathrm{i}} \mathrm{m_i C_i}} - \frac{\mathrm{hS[T(t)-T_0]}}{\sum_{\mathrm{i}} \mathrm{m_i C_i}} \tag{5.11}$$

Table 5.2 Absorbance (Aλ) of GNP, GNP-PEG, GNP-TRP, and GNP-PEG-TRP in water.

Nanoparticles	**GNP**	**GNP-PEG**	**GNP-TRP**	**GNP-PEG-TRP**
Aλ	0.0916	0.0873	0.0863	0.0836

From Eq. (5.11), the constants A and B are defined as

$$A = \frac{\mathrm{P}(1-10^{-\mathrm{A}\lambda})\eta}{\sum_{\mathrm{i}} \mathrm{m_i C_i}} \tag{5.12}$$

$$B = \frac{\mathrm{hS}}{\sum_{\mathrm{i}} \mathrm{m_i C_i}} \tag{5.13}$$

where A is the rate of energy absorption, and B is the rate of heat dissipation, which simplifies Eq. (5.11) to Eq. (5.14)

$$\frac{dT}{dt} = A - B[T(t) - T_0] \tag{5.14}$$

By integrating Eq. (5.14) from 0 to t, the transient temperature for an arbitrary initial temperature value $\mathrm{T_{initial}}$ results as

$$\mathrm{T(t)} = T_0 + \frac{\mathrm{A}}{B}(1 - \mathrm{e}^{-Bt}) + (\mathrm{T_{initial}} - T_0)\mathrm{e}^{-Bt} \tag{5.15}$$

To obtain the photothermal conversion efficiency η, the experimental temperature variations for the different gold nanoparticle dispersions as a function of time during photothermal heating (when $\mathrm{A} \neq 0$ and $\mathrm{T_{initial}} = T_0$) and cooling (when $\mathrm{A} = 0$ and $\mathrm{T_{initial}} > T_0$) are fit to Eq. (5.15). Subsequently, the values of A and B can be extracted from the temperature-time curve fit and used to calculate the photothermal efficiency η of the nanoparticles.

$$\eta = \frac{\mathrm{A}\sum_{\mathrm{i}} \mathrm{m_i C_i}}{\mathrm{P}(1 - 10^{-\mathrm{A}\lambda})} \tag{5.16}$$

5.5. Results

5.5.1. Gold Nanoparticle Biosynthesis and Characterization

After 24 hours, the cell-free extract (CFE) reduced gold (III) chloride trihydrate to gold. This reduction process was observed via a color change from pale yellow to dark purple in the gold (III) chloride trihydrate mixture and cell-free extract (CFE) from Serratia marcescens [37], [46]–[48]. The formation of gold nanoparticles was also verified using TEM and UV–Vis scanning spectrophotometry.

Interestingly, the UV-Vis spectrum in Fig. 5.4 Shows two absorption peaks. The first absorbance peak is in the visible regime for GNP (565 nm), GNP-TRP (571 nm), GNP-PEG (570 nm), and GNP-PEG-TRP (569.5 nm). This visible spectrum absorbance peak is indicative of the presence of gold in the dispersion[37], [38], [48]–[50]. The second absorbance is a weaker absorbance in the NIR regime for GNP (741 nm), GNP-PEG (739 nm), GNP-TRP (737.5 nm), and GNP-PEG-TRP (738.7 nm). Similar reports of dual absorption peaks have been detailed in other biosynthesized gold nanoparticle studies using plant extracts[49], [51].

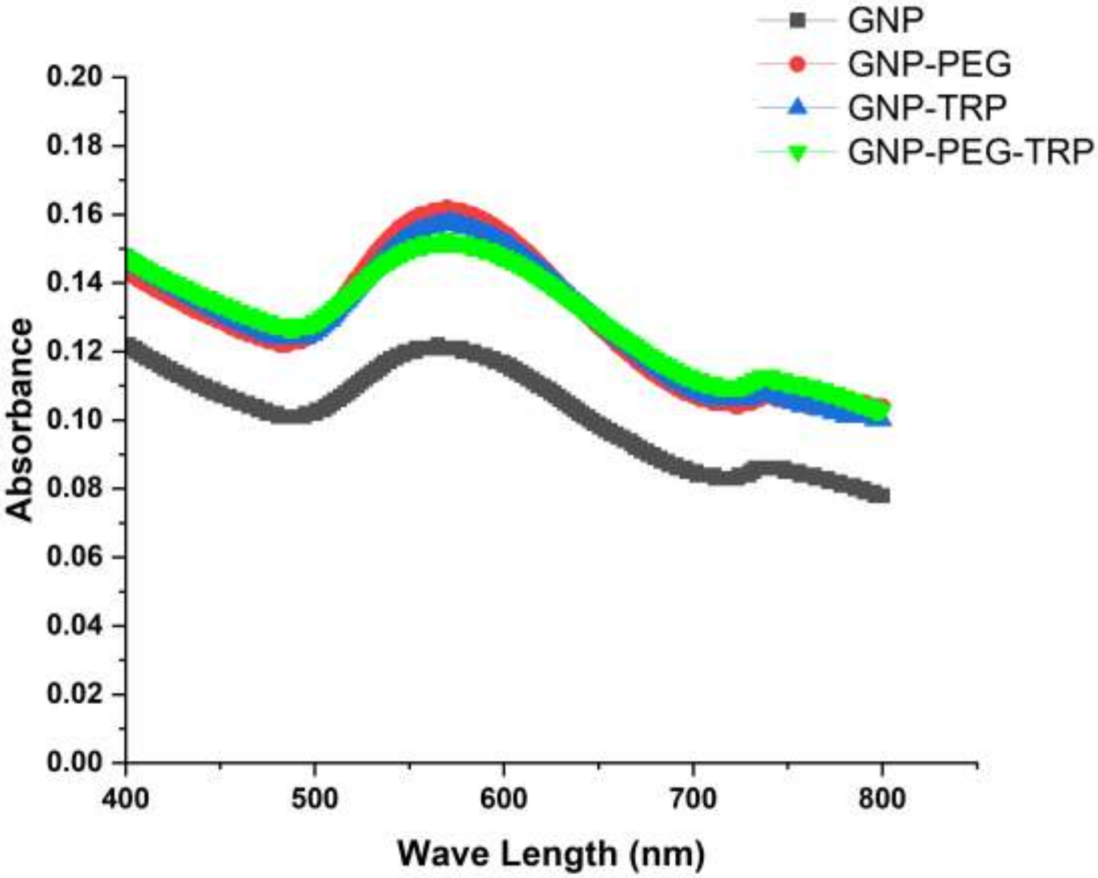

Fig.5.4. UV-Vis absorption spectra of biosynthesized gold nanoparticles show absorption peaks in the visible light regime for GNP (565 nm), GNP-PEG (571 nm), GNP-TRP (570 nm), and GNP-PEG-TRP (569.5 nm). Also, absorption peaks in the near-infrared light region are observed for GNP (741 nm), GNP-PEG (739 nm), GNP-TRP (737.5 nm), and GNP-PEG-TRP (738.7 nm).

Further characterization of the nanoparticles with the TEM reveals micrographs in Fig. 5.5 with nearly spherical GNP, GNP-PEG, GNP-TRP, and GNP-PEG-TRP nanoparticles. The core diameter distribution for the four nanoparticles in Fig. 5.6 reveals that the nanoparticles have a 10 – 30 nm size distribution. However, although the TEM micrographs show average diameter sizes of 16.7 ± 4.1 nm (GNP), 15.6 ± 5.6 nm (GNP-TRP), 14.6 ± 4.2 nm (GNP-PEG), and 15.8 ± 4.6 nm (GNP-PEG-TRP), the hydrodynamic diameter(D) for the GNP (64.7 ± 1.0 nm), GNP-TRP (139.7 ± 1.1 nm), GNP-PEG (55.2 ± 0.2 nm), and GNP-PEG-TRP (76.9 ± 0.1 nm)) were much larger.

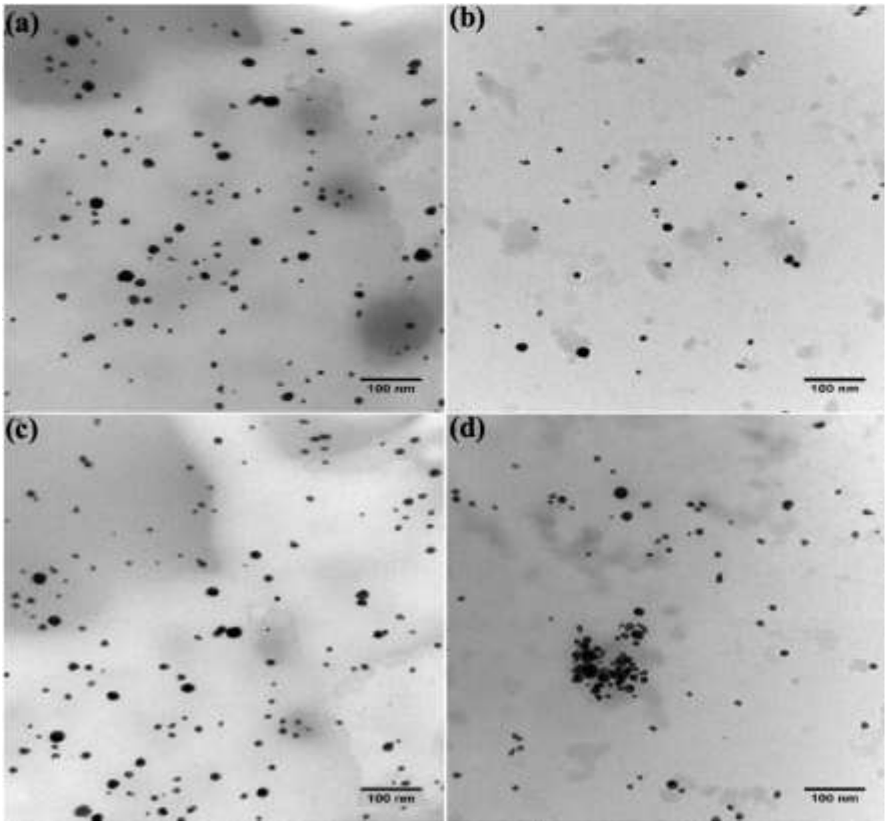

Fig. 5.5. TEM micrographs of (a) GNP, (b) GNP-TRP, (c) GNP-PEG, (d) GNP-PEG-TRP.

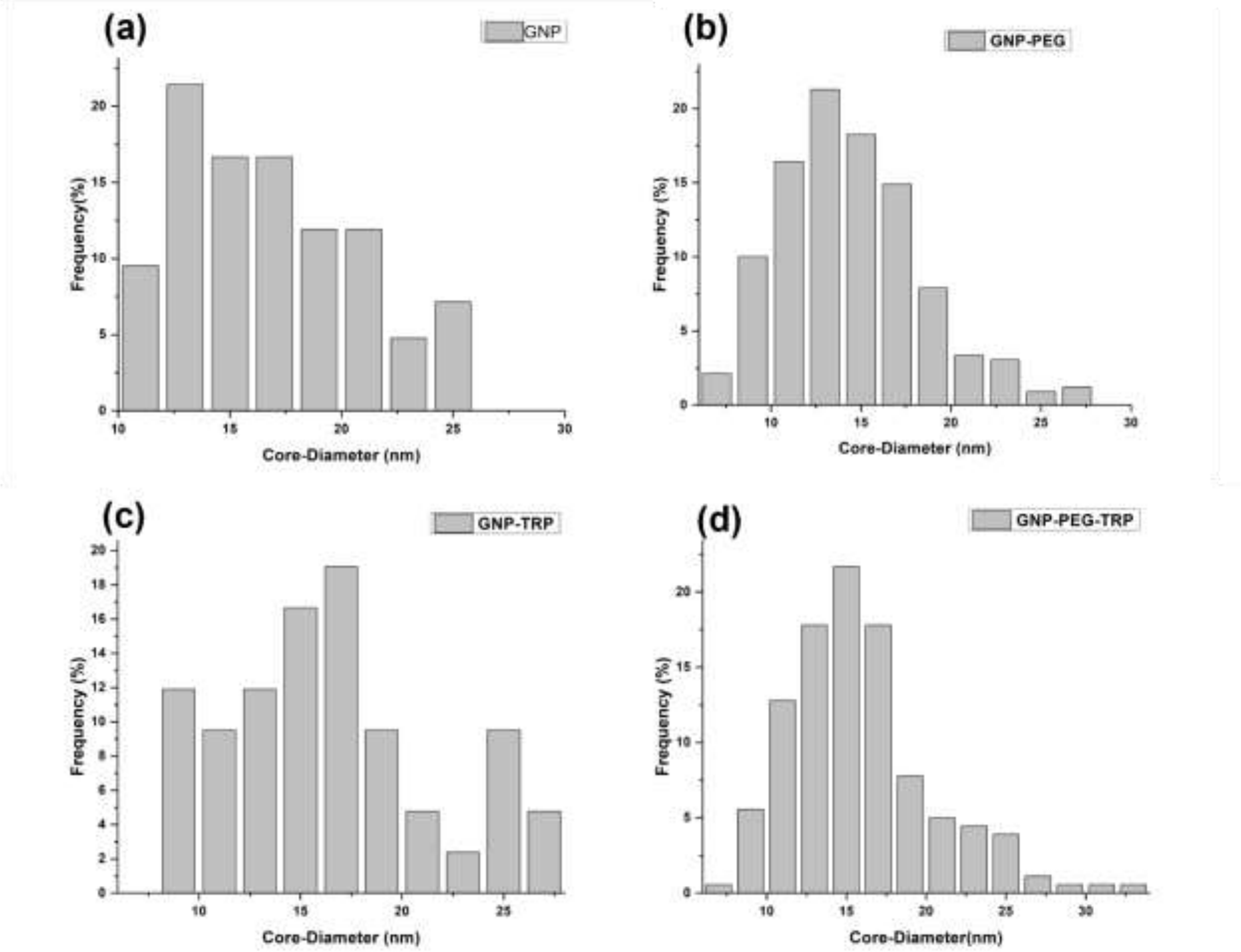

Fig.5.6. (a) TEM core diameter distribution of GNP, (b) TEM core diameter distribution of GNP-PEG, (c) TEM core diameter distribution of GNP-TRP, and (d) TEM core diameter distribution of GNP-PEG-TRP.

Fourier-transform infrared spectroscopy (FTIR) was carried out to identify the functional groups involved in biosynthesis and to confirm the conjugation of TRP ligand. Fig. 5.7 shows the FTIR spectra for CFE, TRP ligand, GNP, GNP-PEG, GNP-TRP, and GNP-PEG-TRP nanoparticles from 400 - 4000 cm^{-1}. Interestingly, the FTIR bands for CFE confirm the presence of carbonyl (aldehyde groups) at 1741 and 1835 cm^{-1}. In addition, C-H groups commonly found in organic molecules are present at 2931 cm^{-1} [41], [50], [52]. The FTIR spectra of CFE reveal several functional groups, including proteins and organic compounds, which many reports of biosynthesis have demonstrated to reduce and stabilize metallic salts to nanoparticles[37], [38], [48]–[51], [53], [54].

Interestingly, just like the CFE spectra, GNP analysis [Fig. 4.5] revealed peaks for carbonyl groups (1835, 1741, and 1692 cm^{-1}). The presence of carbonyl groups on GNP surfaces is associated with adsorbed proteins on the GNP surface due to the biosynthesis method used. A similar FTIR study on the biosynthesis of silver and zinc nanoparticles using a macro-algae extract (Gracilaria Edulis) also reported the presence of carbonyls in the CFE and on the surfaces of the biosynthesized nanoparticles [53].

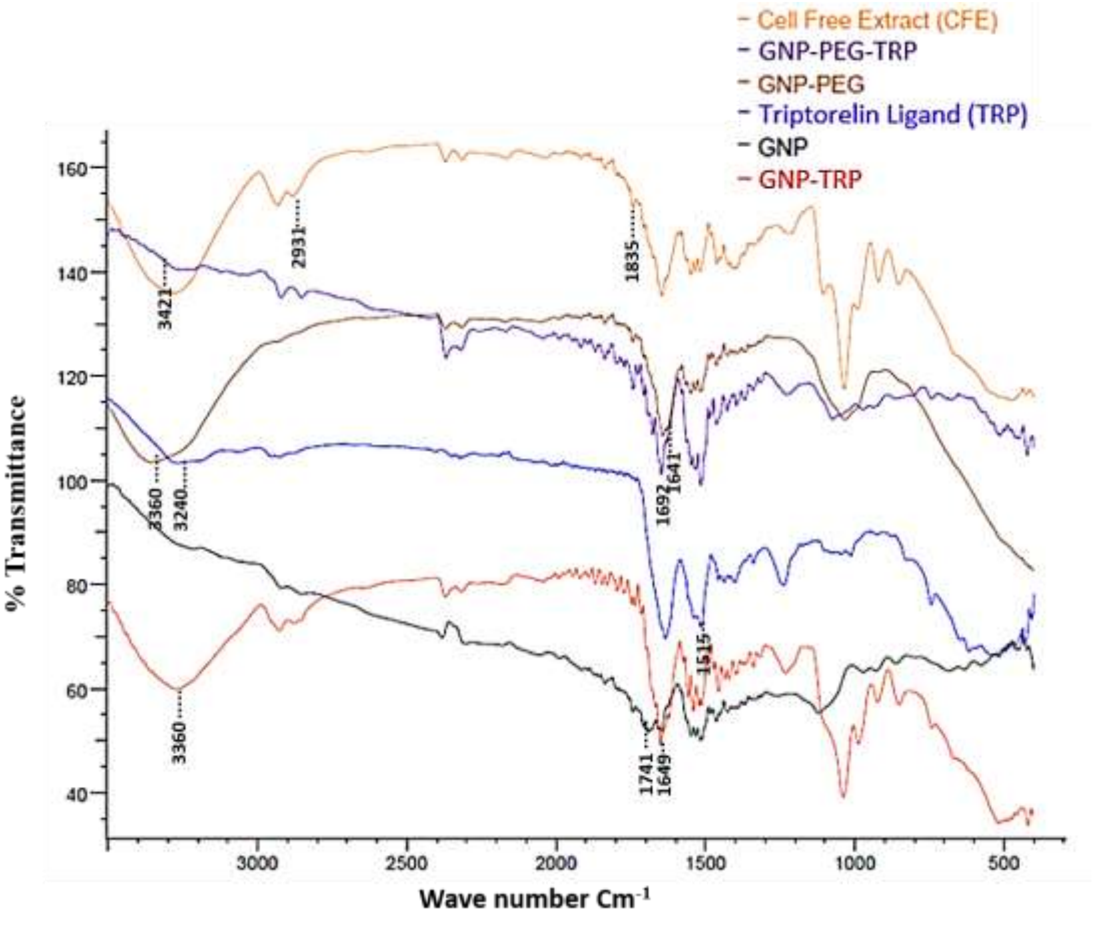

Fig. 5.7. FTIR spectra of the cell-free extract, GNP-PEG-TRP, GNP-PEG, TRP ligand, GNP-TRP, and GNP.

Next, the GNP-PEG spectra show carboxylic group peaks at 3360 cm^{-1} for the OH group, while C=O peaks at 1710 and 1641 cm^{-1} confirmed the presence of a carboxyl terminated polyethylene glycol[55], [56]. Furthermore, GNP-TRP spectra revealed amine functional group peaks (N-H) that were present in the TRP ligand spectra at 1515, 1635, and 3200-3600 cm^{-1}. In addition, the carbonyl group peaks (C=O) that were present in the GNP spectra were absent in GNP-TRP spectra and thus confirmed the formation of the C=N bonds at 1649 cm^{-1} found within the 1640-1690 cm^{-1} range [52], [57], [58]. Although carbonyls are reactive to primary amines, these interactions do not produce strong, stable bonds and require other amination processes [41], [42].

Lastly, the primary amide bond formation in GNP-PEG-TRP spectra at C=O at 1692 cm^{-1} and N-H at 3421 and 3481 $\text{cm}^{-1}$is quite significant and confirms that the carbodiimide (EDC/NHS catalyst) conjugation process between the carboxyl and the TRP ligand primary amine groups occurred [59], [60].

5.5.2. Photothermal Effects of Laser /Gold Nanoparticle Interactions

5.5.2.1. Laser Interactions with Gold Nanoparticles Dispersed in Water

Experimentally, we examined the NIR laser (808 nm) interactions with GNP, GNP-PEG, GNP-TRP, and GNP-PEG-TRP nanoparticles in water for 20 min using a FLIR camera. Generally, except for the control samples[Fig. 5.9], the temperature-time plots [Fig. 5.8 (a)] increased linearly from time 0 to 300 s, reached a steady state at 600 to 1200 s, and spontaneously cooled when the laser source was removed at 1200 s. Notably, at 20 min, GNP maximum temperature GNP T_{max} (47.1 ° C) > GNP-PEG T_{max} (46.3 ° C) > GNP-PEG-TRP T_{max} (45.1 ° C) > GNP-TRP T_{max} (44.7 ° C) [Fig. 5.8 (a)]. All four nanoparticles exhibited cell hyperthermia temperature ranges from 41 to 45 ° C at 0.9 W [Fig. 5.8] and cell ablation temperature ranges (> 50° C) at 2 and 3W [Fig. 5.10]. Specifically, hyperthermia temperatures were observed in GNP at 2 min, GNP-PEG at 3 min, GNP-TRP at 4 min, and GNP-PEG-TRP at 4 min. However, GNP and GNP-PEG temperatures exceeded hyperthermia ranges after 8 min.

Non-uniform temperature distributions within the cuvette are depicted in Fig. 5.1, with the maximum temperatures occurring at the center and lesser temperatures at the liquid/cuvette interface. This non-uniform temperature distribution is because heat dissipates outwards into the surrounding environment via the boundaries.

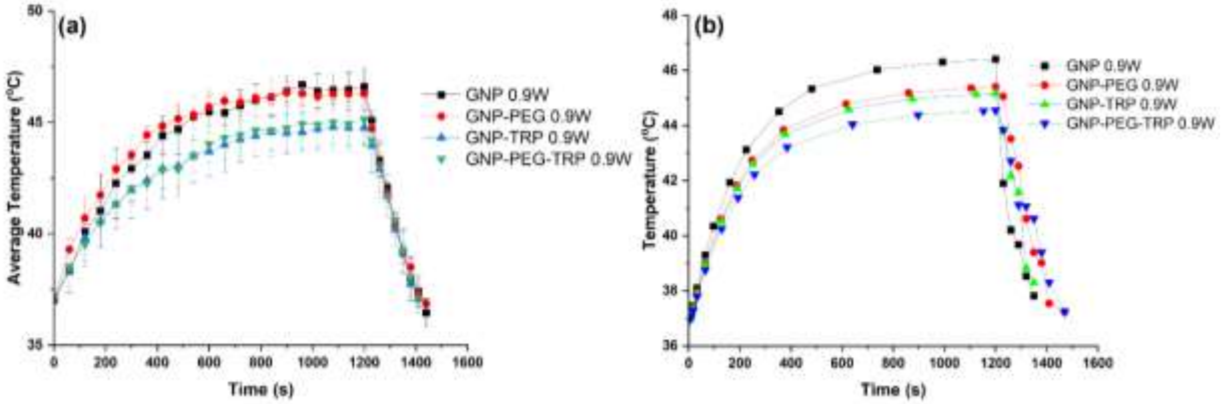

Fig.5.8. Heating and cooling temperature-time plots for the (a) experimental NIR laser (808nm) interactions with GNP, GNP-PEG, GNP-TRP, GNP-PEG-TRP in water at 0.9 W (1.14 W/cm^2), and (b) Finite element model of the NIR laser (808 nm) interactions with GNP, GNP-PEG, GNP-TRP, GNP-PEG-TRP in water at 0.9 W.

The finite element analysis (FEA) [Fig. 5.8 (b)] predicts hyperthermia temperature-time variations for laser/gold nanoparticle interactions that are consistent with the experimental data [Fig. 5.8 (a)]. However, it differs slightly in GNP-TRP T_{max} (45 °C) > GNP-PEG-TRP T_{max} (44 °C) [Fig.]. Also, FEA hyperthermia temperatures were observed in all gold nanoparticles from ~3 min. However, only GNP temperatures exceeded hyperthermia ranges after 12 min.

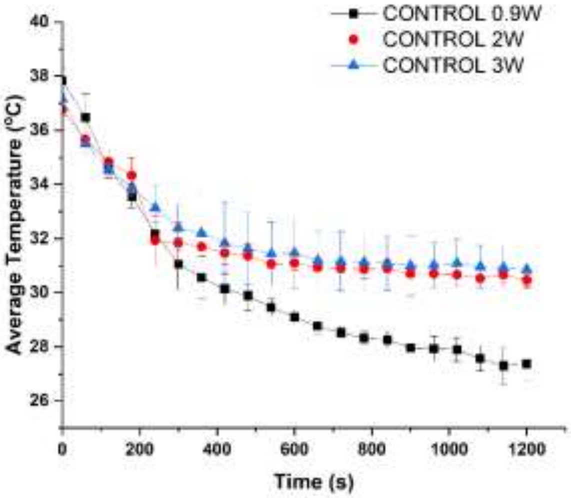

Fig.5.9. Cooling temperature-time plots for the NIR laser (808nm) interactions with water (control) at 0.9, 2, and 3W.

Interestingly, Fig. 5.10 shows experimental and FEA thermal ablation temperature-time plots at 2 and 3W laser interactions with GNP, GNP-PEG, GNP-TRP, and GNP-PEG-TRP. Mainly, GNP, GNP-PEG, GNP-TRP, and GNP-PEG-TRP achieved temperatures T > 50 ºC after 2 min of laser illumination. Similar to the hyperthermia temperature curves at 0.9W [Fig. 5.8], Fig. 5.10(a-d) have a linear, steady-state, and cooling regime. In contrast to the 15 ºC T_{max} jump from gold nanoparticle interactions at 0.9 W to 2W, we observed only a 4 ºC increase in the maximum temperature T_{max} for all nanoparticles from 2 and 3W laser illumination. This similarity in 2W T_{max} and 3W T_{max} signifies a diminishing photothermal effect beyond 2W (2.5 W/cm^2) for GNP, GNP-PEG, GNP-TRP, and GNP-PEG-TRP.

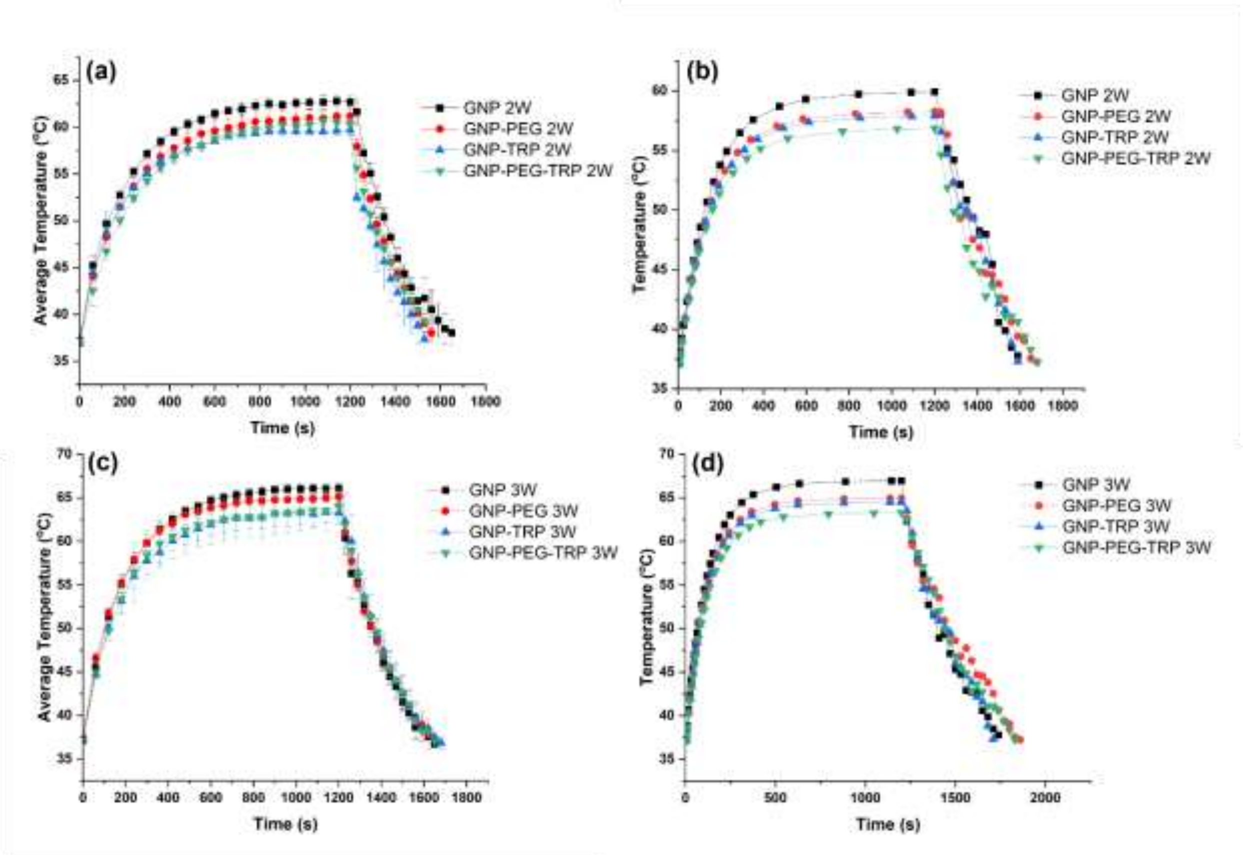

Fig.5.10. Heating and cooling temperature-time plots for the (a) experimental NIR laser (808nm) interactions with GNP, GNP-PEG, GNP-TRP, GNP-PEG-TRP in water at 2 W (2.5 W/cm^2), (b) Finite element model of the NIR laser (808 nm) interactions with GNP, GNP-PEG, GNP-TRP, GNP-PEG-TRP in water at 2 W, (c) experimental NIR laser (808nm) interactions with GNP, GNP-PEG, GNP-TRP, GNP-PEG-TRP in water at 3 W (3.8 W/cm^2), and (d) Finite element model of the NIR laser (808 nm) interactions with GNP, GNP-PEG, GNP-TRP, GNP-PEG-TRP in water at 3W.

Similar to the hyperthermia FEA predictions, thermal ablation FEA [Fig. 5.10 b and d], estimates temperature-time variations for laser/gold nanoparticle interactions consistent with the experimental data [Fig. 5.10 a and c]. Specifically, GNP, GNP-PEG, GNP-TRP, and GNP-PEG-TRP achieved temperatures T > 50 ºC after 2 min of laser illumination. However, it was observed that the FEA predicts that GNP-PEG-TRP has the least T_{max} at 2W (56.8 °C) and 3 W (63.2 °C), which is in contrast to the experimental data, that shows that GNP-TRP had the least T_{max} at 2W (56.8 °C) and 3W (63.2 °C).

5.5.2.2. Photothermal Efficiencies of the Biosynthesized Gold Nanoparticles

To calculate the photothermal efficiencies η due to NIR laser interactions with GNP, GNP-PEG, GNP-TRP, and GNP-PEG-TRP dispersions. The transient temperatures measured for the heating and cooling curves [Fig. 5.8 and 5.10] were fit to Eq. (5.15) at 95% confidence intervals. Table 5.3 shows the rate of energy absorbance (A), rate of heat dissipation (B), and the photothermal efficiencies of all gold nanoparticles at 0.9W(1.1 W/cm^2), 2W (2.6 W/cm^2), and 3W (3.8 W/cm^2). A and B values increased with increasing laser power for GNP, GNP-PEG, GNP-TRP, and GNP-PEG-TRP dispersions. Interestingly, $\eta_{2\,\mathrm{W}} > \eta_{3\,\mathrm{W}} > \eta_{0.9\,\mathrm{W}}$ for all gold nanoparticles and is consistent with the hyperthermia and thermal ablation temperature-time plots presented in [Fig. 5.8] and [Fig. 5.10] respectively.

Overall, the absorbance and photothermal efficiencies for GNP (A, η_{GNP}) were higher than the absorbance and photothermal efficiencies measured in GNP-PEG and GNP-TRP for 0.9, 2, and 3 W. However, it is essential to note that $\eta_{\mathrm{GNP}}(27.8\%) > \eta_{\mathrm{GNP-PEG-TRP}}(26.1\%)$ at only 0.9 W. Interestingly, at 2W, $\eta_{\mathrm{GNP-PEG-TRP}}$ was 68%, while η_{GNP} was 66%. Similarly, at 3W, $\eta_{\mathrm{GNP-PEG-TRP}}$ was 50.7%, while η_{GNP} was 45.7%. The decrease in the photothermal conversion efficiency from 2 W to 3W for GNP, GNP-PEG, GNP-TRP, and GNP-PEG-TRP accounts for the observed 4^o C increase in T$_{max}$ from 2 to 3 W, in contrast to the 15 ^{o} C change from 0.9 to 2 W.

Table 5.3 shows the rate of energy absorption A, rate of heat dissipation B, Absorbance at laser excitation Aλ, and photothermal efficiencies from the NIR laser interaction with GNP, GNP-PEG, GNP-TRP, and GNP-PEG-TRP in water. A and B were fit at 95% confidence interval, *R^2 > 0.95: **R^2 > 0.99.

Sample/Laser Power	**A** $^o\mathrm{C}s^{-1}$	**B** s^{-1}	η **%**
GNP 0.9W	$6.62 \times 10^{-3}*$	$4.39 \times 10^{-2}*$	27.8

GNP 2W	$3.50 \times 10^{-2}*$	$6.67 \times 10^{-2}*$	66.0
GNP 3W	$3.64 \times 10^{-2}**$	$5.54 \times 10^{-2}*$	45.7
GNP-PEG 0.9W	$6.00 \times 10^{-3}*$	$4.00 \times 10^{-2}*$	26.3
GNP-PEG 2W	$3.33 \times 10^{-2}*$	$5.88 \times 10^{-2}**$	65.6
GNP-PEG 3 W	$3.34 \times 10^{-2}*$	$5.67 \times 10^{-2}*$	44.7
GNP-TRP 0.9W	$5.44 \times 10^{-3}*$	$3.87 \times 10^{-2}*$	24.1
GNP-TRP 2W	$3.10 \times 10^{-2}*$	$5.14 \times 10^{-2}**$	61.3
GNP-TRP 3W	$3.33 \times 10^{-2}*$	$5.61 \times 10^{-2}*$	43.5
GNP-PEG-TRP 0.9W	$5.75 \times 10^{-3}*$	$3.63 \times 10^{-2}*$	26.1
GNP-PEG-TRP 2W	$3.33 \times 10^{-2}*$	$5.32 \times 10^{-2}**$	68.0
GNP-PEG-TRP 3W	$3.71 \times 10^{-2}*$	$5.85 \times 10^{-2}*$	50.7

5.5.2.3. In Vitro Cell Viability and Heat Shock Protein 70 (HSP70) Expression in Heat-Treated TNBC Cells

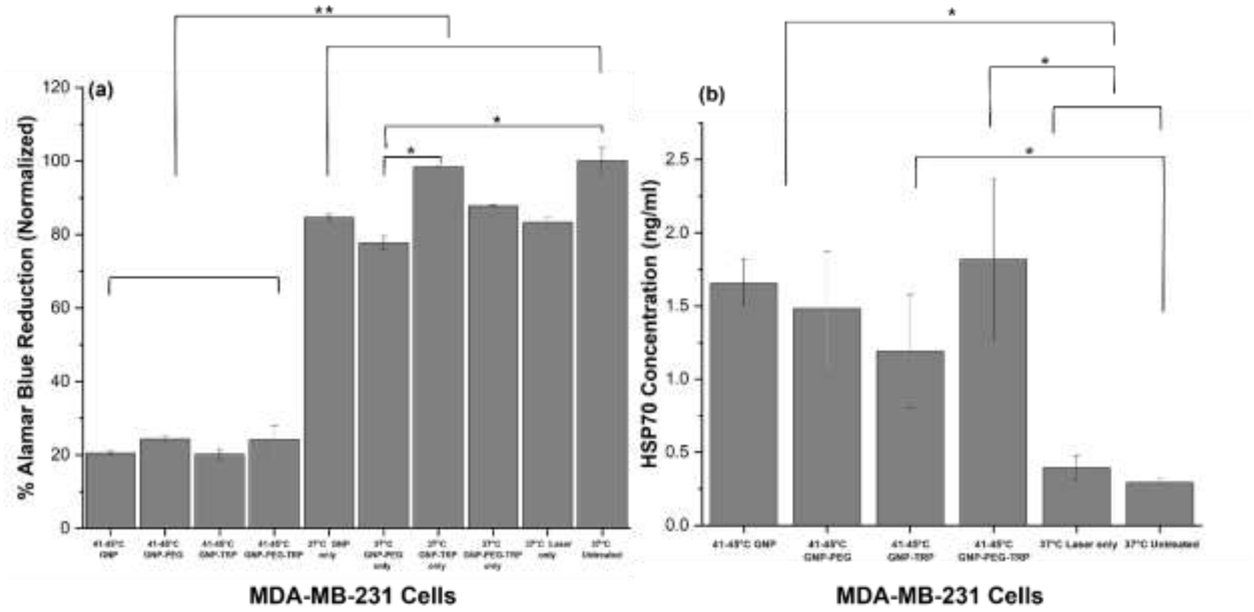

Fig.5.11. (a) Alamar blue cell viability measurements for laser-nanoparticle hyperthermia treated MDA-MD-231 triple-negative breast cancer cells, and (b) Heat shock protein 70 (HSP70) expression for hyperthermia treated MDA-MD-231 triple-negative breast cancer cells.The error bars represent the standard deviations for n = 3 measurements. * $p < 0.05$; ** $p < 0.001$.

Alamar blue assay was used to study the rate of metabolic activity (viability) of the cells treated at hyperthermic temperatures under the NIR laser illumination of GNP, GNP-PEG, GNP-TRP, and GNP-PEG-TRP particles. Briefly, a higher % Alamar blue reduction signifies that that there is more cell metabolic activity and hence, more viable cells. Fig. 5.11 (a) shows results of the % Alamar blue reduction that were normalized with respect to the untreated MDA-MB-231 cell control (cells$_{@\ 37^{o}\ \text{C untreated}}$). Remarkably, for all the control samples, the % Alamar blue reduction values were significantly greater ($p < 0.001$) than the % Alamar blue reduction values of cells exposed to hyperthermic temperatures via laser/ nanoparticle interactions (cells$_{@\ 37^{o}\ \text{C untreated}}$ (100%), cells$_{@\ 37^{o}\ \text{C with laser only}}$ (83.2 %), cells$_{@\ 37^{o}\ \text{C with GNP only}}$ (84.6 %), cells$_{@\ 37^{o}\ \text{C with GNP-PEG only}}$ (77 %), cells$_{@\ 37^{o}\ \text{C with GNP-TRP only}}$ (98.3%), and cells$_{@\ 37^{o}\ \text{C with GNP-PEG-TRP only}}$ (87.8%)cells$_{@\ 41\text{-}45^{o}\ \text{C with GNP}}$ (20.4 %), cells$_{@\ 41\text{-}45^{o}\ \text{C with GNP-PEG}}$ (24.3 %), cells$_{@\ 41\text{-}45^{o}\ \text{C with GNP-TRP}}$ (20.1 %), and cells$_{@\ 41\text{-}45^{o}\ \text{C with GNP-PEG-TRP}}$ (24.1 %).

Furthermore, no significant variations ($p > 0.05 \leq 1.00$) in % Alamar blue reduction values were observed in cells subjected to hyperthermia temperatures via laser interactions with different gold nanoparticles (GNP, GNP-PEG, GNP-TRP, and GNP-PEG-TRP).

Also, there were no significant differences ($p > 0.05 \leq 1.00$) in % Alamar blue reduction among control samples, except for cells$_{@\ 37^{\circ}\text{ C with GNP-PEG only}}$ samples, which were significantly different from cells$_{@\ 37^{\circ}\text{ C untreated}}$ ($p = 0.005$) and cells$_{@\ 37^{\circ}\text{ C with GNP-TRP only}}$ ($p = 0.01$).

Heat shock protein expression in biological cells is typically associated with their exposure to temperatures above 41ºC. Fig.5.11 (b) elucidates the HSP70 concentrations (ng/mL) for both the control and hyperthermia treated cells. In contrast to HSP70 concentrations in the controls, cells$_{@\ 37^{\circ}\text{ C untreated}}$ (0.28 ± 0.02 ng/mL) and cells$_{@\ 37^{\circ}\text{ C with only laser}}$ (0.39 ± 0.08 ng/mL), a significant increase ($p < 0.05$) in HSP70 concentration was recorded for all cells exposed to hyperthermia temperatures (cells$_{@\ 41\text{-}45^{\circ}\text{ C with GNP laser}}$ (1.65 ± 0.17 ng/mL), cells$_{@\ 41\text{-}45^{\circ}\text{ C with GNP-PEG}}$ (1.48 ± 0.39 ng/mL), cells$_{@\ 41\text{-}45^{\circ}\text{ C with GNP-TRP}}$ (1.19 ± 0.38), and cells$_{@\ 41\text{-}45^{\circ}\text{ C with GNP-PEG-TRP}}$ (1.82 ± 0.55 ng/mL) except cells$_{@\ 41\text{-}45^{\circ}\text{ C with GNP-TRP}}$, which were not significantly different ($p = 0.095$) from cells$_{@\ 37^{\circ}\text{ C with only laser}}$.

Finally, there was no significant ($p = 0.998$) variation in HSP70 concentration among cells$_{@\ 37^{\circ}\text{ C untreated}}$ and cells$_{@\ 37^{\circ}\text{ C with laser only}}$ control samples.

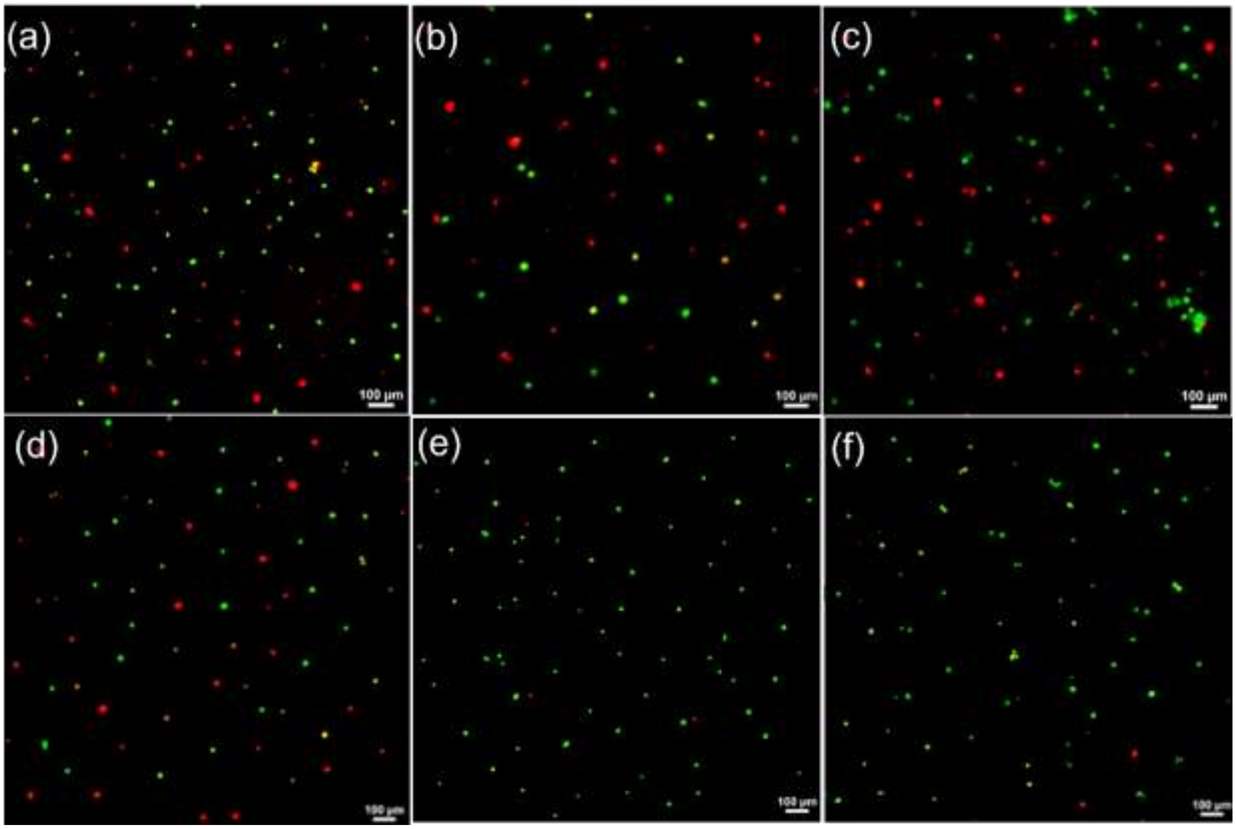

Fig.5.12. Fluorescence images of live and dead cells in MDA-MB-231 cells treated with (a) GNP, (b) GNP-PEG, (c) GNP-TRP, (d) GNP-PEG-TRP. It also shows the controls' live/dead fluorescence images (e) untreated cells and (f) cells exposed to laser illumination without nanoparticles (laser only). Calcein-AM emits green fluorescence excitation at 490 nm from live cells, while Propidium Iodide PI emits red fluorescence excitation at 535 nm from dead cells.

Additionally, the cell viability of the hyperthermia-treated cells was also observed using a double stain live/dead fluorescence assay that determines cell viability via the intracellular esterase activity and the cell plasma membrane integrity. The green Calcein-AM fluorescence dye is permeable to the cell membrane and only stains viable cells. In contrast, the red Propidium iodide fluorescence is a DNA-binding agent which is only permeable to the damaged cell membrane and is an indicator for dead cells.

The fluorescent cell viability data presented in Fig. 5.12 a-f is consistent with the % Alamar blue reduction data in Fig. 5.11 (a). These cell viability studies show that cells exposed to hyperthermia temperatures via laser/ GNP, GNP-PEG, GNP-TRP, and GNP-PEG-TRP interactions had more dead cells with red fluorescence than control samples in Fig. 5.12 e and f.

5.5.3. Laser Interactions with Gold Nanoparticles in Chicken Tissue

5.5.3.1. Stationary Laser Source Interaction with Gold Nanoparticles in Chicken Tissue

To study the photothermal effects of GNP, GNP-PEG, GNP-TRP, and GNP-PEG-TRP in tissue, we examined the nanoparticle-NIR laser interactions in chicken tissue under stationary laser irradiation. The chicken model mimics the tissue laser interactions that can occur during potential in vivo applications of gold nanoparticles in targeted hyperthermia for TNBC treatment. Specifically, we explored the maximum laser power (3W) and incision depth (6 mm) beneath the chicken for which hyperthermia temperatures can be achieved for a given concentration of biosynthesized gold nanoparticles [Fig. 5.13]. In general, Fig. 5.13 (a) shows non-uniform temperature distributions across the chicken tissue surface. The heat radiates outwards into the surrounding tissue, with the maximum temperature recorded at the center of the tissue incision where the nanoparticles are located.

Notably, cell ablation temperature ranges (> 50º C) were observed for GNP-laser interactions [Fig. 5.13 (a)] while GNP-PEG, GNP-TRP, and GNP-PEG-TRP achieved hyperthermia temperatures within 20min. However, the maximum recorded temperature Tmax trends are consistent with the hyperthermia interactions in water Fig. 5.8 and 5.10.

Interestingly, there is a two to threefold decrease in the photothermal efficiency from GNP (22.6%) with surface modification with PEG-Coatings and the TRP ligand of the biosynthesized GNP. This decrease is attributed to the reduced rate of absorbance estimated for these nanoparticles, as shown in Table 5.4

Also notable is the two-fold increase in the heat dissipated from the tissue treated with GNP [Table] compared to the PEG-coated and TRP functionalized nanoparticles. It is important to note that maximum photothermal efficiencies in the chicken tissue in Table 5.4 were less than that reported in the water table's laser-nanoparticle interactions. Additionally, GNP had the highest conversion efficiency in chicken tissue. Nevertheless, the chicken tissue model showed that GNP-PEG, GNP-TRP, and GNP-PEG-TRP could achieve sustained hyperthermia ranges even with low photothermal conversion efficiencies.

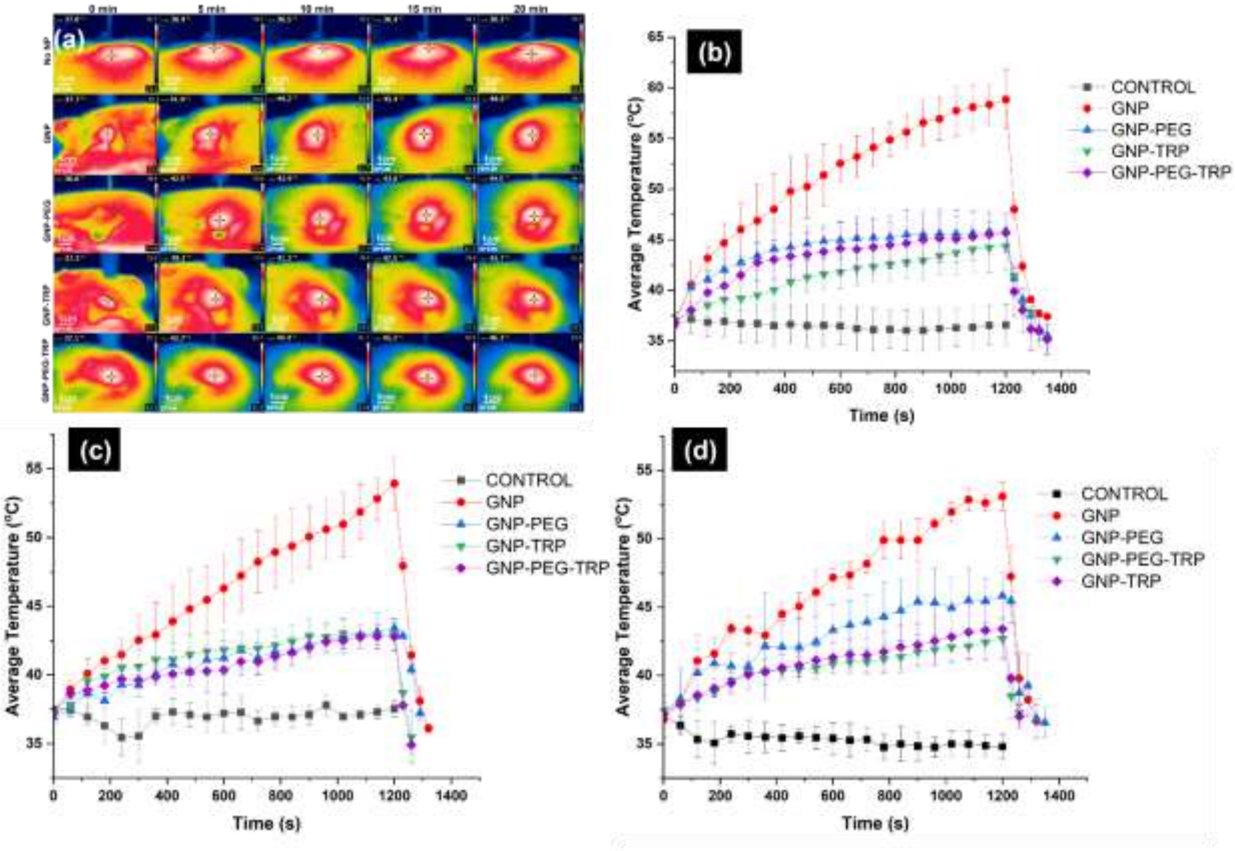

Fig.5.13. a) Spatial temperature distributions across chicken tissue for a 3W stationary laser source interaction with GNP, GNP-PEG, GNP-TRP, and GNP-PEG-TRP at 0, 5, 10, 15, and 20 mins. The Measured temperature profiles for the various gold nanoparticles in chicken tissue at 6 mm depth and 3W are shown

in (b) for a stationary laser position, (c) modified 3D printer positioning, and (d) laser positioning with a UR5 robotic arm with six degrees of freedom.

5.5.3.2. 3D Printer Controlled Laser Source Interaction with Gold Nanoparticles in Chicken Tissue

To study the effects of a moving laser source on the illumination of GNP, GNP-PEG, GNP-TRP, and GNP-PEG-TRP in tissue, we examined the nanoparticle-NIR laser interactions in chicken tissue under a modified fusion deposition modeling (FDM) 3D printer nozzle that performs raster motion along the XY axis and height modulation along the Z axis. The laser control mimics gantry type robots for laser applications in potential in vivo or medical applications of gold nanoparticles for TNBC treatment. The temperature-time plots are similar for a stationary laser source and a moving laser source, however local variations in temperature are observed over time as the laser source moves in relation to the nanoparticle position. These local temperature variations are attributed to the increase in the dissipation rate for 3D controlled laser source in contrast to the stationary laser control. Nevertheless, all nanoparticles achieved hyperthermia temperatures while GNP laser interactions were at thermal ablation ranges.

5.5.3.3. Robotic-Arm Controlled Laser Source Interaction with Gold Nanoparticles in Chicken Tissue

The effects of angular interactions introduced by a moving laser source on the interactions on GNP, GNP-PEG, GNP-TRP, and GNP-PEG-TRP in tissue, were examined using a universal robot UR5 positioning arm with six degrees of freedom was used to introduce angular variations in the laser interactions with the nanoparticles.

This laser control mimics applications where angular laser applications are required for in vivo or medical applications of gold nanoparticles for TNBC treatment. It is important to note the increased visible temperature variations due to the alternate raster and angular motion of the laser source. Similar to the 3D-controlled laser source, these temperature variations are attributed to the increase in the dissipation rate for the robotic arm-controlled laser source in contrast to the stationary laser control.

Irrespective of the laser control, GNP had the highest photothermal efficiency. This efficiency decreased from 22.6 % in the stationary laser source to 16.2 % in the 3D-controlled laser source and 16% when the laser was moved with a robotic arm.

Table 5.4 shows the rate of energy absorption A, heat dissipation B, Absorbance at laser excitation Aλ , and photothermal efficiencies from the NIR laser interaction with GNP, GNP-PEG GNP-TRP, and GNP-PEG-TRP in chicken tissue at 3W. A and B were fit at 95% confidence interval, *$R^2 > 0.95$: **$R^2 > 0.99$.

Sample/ 3 W	**A** **°Cs^{-1}**	**B** **s^{-1}**	**η** **%**
GNP **stationary**	$1.81 \times 10^{-2}*$	$9.7 \times 10^{-2}*$	22.6
GNP-PEG **stationary**	$5.13 \times 10^{-3}*$	$4.76 \times 10^{-2}*$	6.7
GNP-TRP **stationary**	$5.79 \times 10^{-3}*$	$4.98 \times 10^{-2}*$	7.6
GNP-PEG-TRP **stationary**	$5.99 \times 10^{-3}*$	$3.84 \times 10^{-2}*$	8.1
GNP **3D Printer**	$1.29 \times 10^{-2}*$	$1.60 \times 10^{-1}*$	16.2
GNP-PEG **3D Printer**	$4.94 \times 10^{-3}*$	$9.42 \times 10^{-2}*$	6.4
GNP-TRP **3D Printer**	$4.04 \times 10^{-3}*$	$1.10 \times 10^{-1}*$	5.4
GNP-PEG-TRP **3D Printer**	$4.08 \times 10^{-3}*$	$9.00 \times 10^{-2}*$	5.6

GNP $_{\text{UR5 Robot}}$	$1.27 \times 10^{-2}*$	$1.50 \times 10^{-1}*$	16.0
GNP-PEG $_{\text{UR5 Robot}}$	$6.35 \times 10^{-3}*$	$6.57 \times 10^{-2}*$	8.3
GNP-TRP $_{\text{UR5 Robot}}$	$3.79 \times 10^{-3}*$	$4.17 \times 10^{-2}*$	5.0
GNP-PEG-TRP $_{\text{UR5 Robot}}$	$4.67 \times 10^{-}*$	$9.30 \times 10^{-2}*$	6.4

5.6. Discussion

5.6.1. Gold Nanoparticle Biosynthesis and Characterization

The biosynthesis of gold nanoparticles from gold chloride salts is attributed to cytochrome complex reduction of $HAuCl_4$. The process of cytochrome reduction has been well documented in prior studies done by our group [37]. Briefly, the cytochrome transmembrane protein complex found in bacteria is responsible for the cell membrane electron transports and balancing the proton potential across the bacteria cell membrane. In the presence of gold chloride salts, the ionized gold salt in the solution receives electrons from the cytochrome reactions, which results in the formation of gold nanoparticles within the bacterial cell membrane and walls[37].

Interestingly, the UV-VIS absorption wavelength for the biosynthesized gold nanoparticles reveals absorption peaks in the NIR region. It has been observed in prior studies that with an increase in the concentration of the organic synthesis broth such as leaf extract, the peak in the NIR region blue shifts to the visible region and disappears beyond a specific concentration, and expresses optical properties characteristic of spherical gold nanoparticle particles [49][51]. Hence tuning the synthesis parameters could lead to single visible light absorbance peaks or Visible and NIR peaks. Generally higher concentration of the reducing agents leads to very strong visible absorption spectra [49][51]. However, lower concentrations of the synthesis broth lead to longer synthesis times[50]. But the presence of NIR peaks enables the biosynthesized nanoparticles to be used as photothermal agents in NIR laser hyperthermia applications. Also, TEM images show nearly spherical nanoparticles. However, NIR absorbance bands indicate nanoparticle anisometric that requires further investigation beyond the paper's scope.

5.6.2. Photothermal Effects of Laser /Gold Nanoparticle Interactions

The photothermal properties of the GNP, GNP-PEG, GNP-TRP and GNP-PEG-TRP dispersed in water at different laser powers in Fig. 5.8 show that the temperature increases with the increasing duration of laser/nanoparticle interaction and is consistent with earlier reported studies in Refs.[36], [61]**.** However, the experiments and FEA model demonstrate a decrease in the photothermal efficiency because of TRP ligand functionalization and PEG-coating. This decrease in the photothermal efficiency due TRP and PEG coatings is more prominent at lower laser powers, as observed at 0.9 W. In general, we observe that TRP conjugation and PEG coating the biosynthesized gold nanoparticles reduce the absorbance rate of incident laser beams. However, the dissipation rate is also reduced due to surface modification of the bare GNP. These reduced dissipation rates indicate that TRP ligand and PEG coatings exhibit insulator properties on GNP.

Alamar blue assay was used to study the rate of metabolic activity (viability) of the cells treated at hyperthermic temperatures under the NIR laser illumination of GNP, GNP-PEG, GNP-TRP, and GNP-PEG-TRP particles.

The results show that TNBC cells treated at hyperthermic temperatures via gold nanoparticle laser interaction had significantly lower live cell metabolic activity and hence were less viable due to the hyperthermia treatment. This reduction in cell viability indicates that the 20min GNP, GNP-PEG, GNP-TRP, and GNP-PEG-TRP interactions with the NIR laser were sufficient to trigger cell death processes in TNBC in vitro. It is also important to note that the control samples exposed to laser only or only nanoparticles posed minimal toxicity as indicated by the % Alamar blue reduction compared to the control sample, except GNP-PEG with sig ($p< 0.05$) reduced cell viability (77%) a little more than untreated cells. Nevertheless, they were still significantly higher live-cell activity in that sample ($p < 0.001$) than in all the samples exposed to hyperthermia temperature levels. The issue of gold nanoparticle toxicity to cells is particularly important because our findings differ from reports that have shown that chemically synthesized gold nanoparticles have chemical residues that introduce additional toxicity in vivo [34], [35].

The heat associated with hyperthermia induces heat stress on tumor cells, which causes the HSP70 to significantly higher expression in cells exposed to laser interactions with various gold nanoparticles. This increased HSP70 expression suggests that the decrease in cell viability observed above after hyperthermia cell interactions can be attributed to programmed cell death due to a decrease in cell viability.

5.6.3. Laser Interactions with Gold Nanoparticles in Chicken Tissue

In chicken tissue at a depth of 6mm, the attenuating effects of PEG and TRP functionalization are more apparent due to the interplay between absorbed laser power and the rate of heat dissipation.

Therefore, if a tumor is more than 6 mm deep, the gold nanoparticle concentrations could be increased to offset this coating effect. Also, the biosynthesis method could be tuned to synthesize gold nanoparticles with increased absorbance in the NIR regime to generate hyperthermic temperatures that inhibit cancer cell growth.

Both Robotics assisted laser positioning styles can be used for precision-guided and controlled hyperthermia or higher temperature applications. However, a robotic arm with six degrees of freedom is more prone to heat losses when the laser beam is not in the direct path of the nanoparticles. These associated heat losses can be corrected by optimizing the speed of laser arm positioning and the programmed travel path laser interaction.

5.6.4. Implications

The implications of the above results are significant for the design of gold nanoparticles with favorable photothermal characteristics for localized hyperthermia treatment of TNBC. First, biosynthesis of NIR laser responsive gold nanoparticles with minimal toxicity provides a basis for using biosynthesized gold nanoparticles for potential applications in vivo treatment of TNBC.

Furthermore, the resulting hyperthermia and thermal ranges observed in PEG-coated and TRP functionalized gold nanoparticles suggest that these nanoparticles could facilitate targeted controlled multi-temperature dose treatment of TNBC. However, further work is needed to investigate the thermal ablation properties of these targeted biosynthesized GNP, especially for laser scalpel applications.

Furthermore, the chicken model demonstrates that localized heating within the chicken tissue can be achieved with less than lethal temperatures around the focal point of heat application, which mimics human skin heat dissipation characteristics. This localized heating is significant for reducing non-tumorigenic tissue damage in vivo applications.

The use of robotics-controlled laser positioning provides insights into parametric adjustments to account for heat losses associated with laser source movement. It also can be applied to the treatment of complex tumor geometries.

This study suggests that the unique properties of biosynthesized gold nanoparticles can be used for hyperthermic treatment with the potential for thermal ablation and treatment of near-surface tumors. However, further work is needed to demonstrate the effectiveness of precision nanoparticle-guided laser cutting applications for the treatment of TNBC. These are some of the challenges for future work.

5.7. Conclusions

1. Gold nanoparticle biosynthesis methods with Serratia Marscensces produce nanoparticles with well-defined optical properties in the NIR regime with minimal toxicities. Furthermore, the photothermal properties of these gold nanoparticles differ based on the surface modifications. This difference in photothermal properties is associated with the changes in the rate of photon absorption and heat dissipation from surfaces of TNBC cells and chicken tissue.
2. The cell viability and heat shock protein expressions of heat-treated TNBC cells show that with laser irradiation, the biosynthesized gold nanoparticles can achieve temperatures sufficient for hyperthermia and induce cell death processes within treated TNBC cells.

3. The chicken tissue experiments demonstrate that the hyperthermic heating at depths of 6mm beneath the skin surface can be localized within the incised chicken tissue groove to limit high-temperature tissue damage in the surrounding tissue.
4. Robotics laser positioning can be achieved for applications that require guided laser beams with well-controlled power and wavelengths to interact with magnetite nanoparticles to induce heating that is sufficient to enable photothermal therapy via laser hyperthermia. Higher temperatures may also be generated at higher laser powers, which may be helpful in future robotically-assisted surgical procedures

5.8. References

[1] O. Gluz, C. Liedtke, N. Gottschalk, L. Pusztai, U. Nitz, and N. Harbeck, "Triple-negative breast cancer - Current status and future directions," Ann. Oncol., vol. 20, no. 12, pp. 1913–1927, 2009.

[2] W. J. Irvin and L. A. Carey, "What is triple-negative breast cancer ?," Eur. J. Cancer, vol. 44, no. 18, pp. 2799–2805, 2008.

[3] W. D. Foulkes, I. E. Smith, and J. S. Reis-Filho, "Triple-Negative Breast Cancer," 2010.

[4] J. Qiu et al., "Comparison of clinicopathological features and prognosis in triple-negative and non-triple negative breast cancer," J. Cancer, vol. 7, no. 2, pp. 167-173.pdf, 2016.

[5] S. Y. Bae et al., "Poor prognosis of single hormone receptor- positive breast cancer: Similar outcome as triple-negative breast cancer," BMC Cancer, vol. 15, no. 1, pp. 1–9, 2015.

[6] Y. Pan, Y. Yuan, G. Liu, and Y. Wei, "P53 and Ki-67 as prognostic markers in triplenegative breast cancer patients," PLoS One, vol. 12, no. 2, 2017.

[7] X. Zhu et al., "The prognostic and predictive potential of Ki-67 in triple-negative breast cancer," Sci. Rep., vol. 10, no. 1, 2020.

[8] A. R. T. Bergin and S. Loi, "Triple-negative breast cancer: Recent treatment advances [version 1; peer review: 2 approved]," F1000Research, vol. 8, 2019.

[9] L. Yin, J. J. Duan, X. W. Bian, and S. C. Yu, "Triple-negative breast cancer molecular subtyping and treatment progress," Breast Cancer Res., vol. 22, no. 1, pp. 1–13, 2020.

[10] L. Y. Xia, Q. L. Hu, J. Zhang, W. Y. Xu, and X. S. Li, “Survival outcomes of neoadjuvant versus adjuvant chemotherapy in triple-negative breast cancer: A meta-analysis of 36,480 cases,” World J. Surg. Oncol., vol. 18, no. 1, pp. 1–8, 2020.

[11] M. Núñez Abad et al., “Update on systemic treatment in early triple negative breast cancer,” Ther. Adv. Med. Oncol., vol. 13, 2021.

[12] P. Cherukuri, E. S. Glazer, and S. A. Curley, “Targeted hyperthermia using metal nanoparticles,” Adv. Drug Deliv. Rev., vol. 62, no. 3, pp. 339–345, 2010.

[13] K. Kan-Dapaah, N. Rahbar, and W. Soboyejo, “Implantable magnetic nanocomposites for the localized treatment of breast cancer,” J. Appl. Phys., 2014.

[14] T. M. Zagar et al., “Hyperthermia combined with radiation therapy for superficial breast cancer and chest wall recurrence: A review of the randomised data,” Int. J. Hyperth., vol. 26, no. 7, pp. 612–617, 2010.

[15] M. W. Dewhirst, B. L. Viglianti, M. Lora-Michiels, M. Hanson, and P. J. Hoopes, “Basic principles of thermal dosimetry and thermal thresholds for tissue damage from hyperthermia,” in International Journal of Hyperthermia, 2003, vol. 19, no. 3, pp. 267–294.

[16] G. L. DeNardo and S. J. DeNardo, “Turning the heat on cancer,” Cancer Biother. Radiopharm., vol. 23, no. 6, pp. 671–679, 2008.

[17] M. Dewhirst, P. R. Stauffer, S. Das, O. I. Craciunescu, and Z. Vujaskovic, “Hyperthermia,” in Clinical Radiation Oncology, Elsevier, 2015, pp. 381-398.e6.

[18] A. Granja, M. Pinheiro, C. T. Sousa, and S. Reis, “Gold nanostructures as mediators of hyperthermia therapies in breast cancer,” Biochemical Pharmacology, vol. 190. Elsevier, p. 114639, 01-Aug-2021.

[19] P. S. Yarmolenko et al., “Thresholds for thermal damage to normal tissues: An update,” International Journal of Hyperthermia, vol. 27, no. 4. pp. 320–343, 2011.

[20] H. W. Huang and T. L. Horng, “Bioheat Transfer and Thermal Heating for Tumor Treatment,” in Heat Transfer and Fluid Flow in Biological Processes, Elsevier Inc., 2015, pp. 1–42.

[21] R. Haghniaz, R. D. Umrani, and K. M. Paknikar, “Temperature-dependent and time-dependent effects of hyperthermia mediated by dextran-coated La0.7Sr0.3MnO3: In vitro studies,” Int. J. Nanomedicine, vol. 10, pp. 1609–1623, 2015.

[22] Y. Zhang et al., “Temperature-dependent cell death patterns induced by functionalized gold nanoparticle photothermal therapy in melanoma cells,” Sci. Rep., vol. 8, no. 1, 2018.

[23] R. F. Brem, “Radiofrequency ablation of breast cancer: A step forward,” Radiology, vol. 289, no. 2, pp. 325–326, 2018.

[24] E. Tammam, A. M. Said, A. A. Ibrahim, and A. I. A. Galal, “About the interstitial microwave cancer ablation: Principles, advantages and challenges,” IEEE Access, vol. 8, pp. 49685–49694, 2020.

[25] T. Nguyen, E. Hattery, and V. P. Khatri, “Radiofrequency ablation and breast cancer: a review.,” Gland Surg., vol. 3, no. 2, pp. 128–12835, 2014.

[26] T. P. Ryan and C. L. Brace, “Interstitial microwave treatment for cancer: historical basis and current techniques in antenna design and performance,” International Journal of Hyperthermia, vol. 33, no. 1. pp. 3–14, 2017.

[27] K. Kan-Dapaah, N. Rahbar, A. Tahlil, D. Crosson, N. Yao, and W. Soboyejo, “Mechanical and hyperthermic properties of magnetic nanocomposites for biomedical applications,” J. Mech. Behav. Biomed. Mater., vol. 49, no. April, pp. 118–128, 2015.

[28] S. Krishnan, P. Diagaradjane, and S. H. Cho, “Nanoparticle-mediated thermal therapy: Evolving strategies for prostate cancer therapy,” International Journal of Hyperthermia. 2010.

[29] A. Fernandez-Fernandez, R. Manchanda, and A. J. McGoron, “Theranostic applications of nanomaterials in cancer: Drug delivery, image-guided therapy, and multifunctional platforms,” Appl. Biochem. Biotechnol., vol. 165, no. 7–8, pp. 1628–1651, 2011.

[30] A. Paściak, A. Pilch-Wróbel, Ł. Marciniak, P. J. Schuck, and A. Bednarkiewicz, “Standardization of Methodology of Light-to-Heat Conversion Efficiency Determination for Colloidal Nanoheaters,” ACS Appl. Mater. Interfaces, vol. 13, no. 37, pp. 44556–44567, 2021.

[31] F. Jabeen, M. Najam-Ul-Haq, R. Javeed, C. W. Huck, and G. K. Bonn, “molecules Au-Nanomaterials as a Superior Choice for Near-Infrared Photothermal Therapy,” Molecules, vol. 19, pp. 20580–20593, 2014.

[32] S. Siddique and J. C. L. Chow, “Gold nanoparticles for drug delivery and cancer therapy,” Applied Sciences (Switzerland), vol. 10, no. 11. 2020.

[33] J. Lee, D. K. Chatterjee, M. H. Lee, and S. Krishnan, “Gold nanoparticles in breast cancer treatment: Promise and potential pitfalls,” Cancer Lett., vol. 347, no. 1, pp. 46–53, 2014.

[34] N. Gupta and R. Malviya, “Understanding and advancement in gold nanoparticle targeted photothermal therapy of cancer,” Biochim. Biophys. Acta - Rev. Cancer, vol. 1875, no. 2, p. 188532, Apr. 2021.

[35] S. K. Surapaneni, S. Bashir, and K. Tikoo, “Gold nanoparticles-induced cytotoxicity in triple negative breast cancer involves different epigenetic alterations depending upon the surface charge,” Sci. Rep., vol. 8, no. 1, 2018.

[36] Y. Danyuo et al., “Laser Application of Nanocomposite Hydrogels on Cancer Cell Viability,” MRS Adv., vol. 5, no. 26, pp. 1377–1385, 2020.

[37] S. . Dozie-Nwachukwu et al., “Biosynthesis of Gold Nanoparticles with Serratia marcescens Bacteria,” Adv. Mater. Res., vol. 1132, no. 19, pp. 19–35, 2016.

[38] E. Hampp, R. Botah, O. Odusanya, N. Anuku, K. Malatesta, and W. Soboyejo, “Biosynthesis and adhesion of gold nanoparticles for breast cancer detection and treatment,” J. Mater. Res., vol. 27, no. 22, pp. 2891–2901, 2012.

[39] E. L. Bentzen et al., “Surface modification to reduce nonspecific binding of quantum dots in live cell assays,” Bioconjug. Chem., vol. 16, no. 6, pp. 1488–1494, 2005.

[40] M. Zheng, F. Davidson, and X. Huang, “Ethylene glycol monolayer protected nanoparticles for eliminating nonspecific binding with biological molecules,” J. Am. Chem. Soc., vol. 125, no. 26, pp. 7790–7791, 2003.

[41] G. T. Hermanson, Bioconjugate Techniques: Third Edition. 2013.

[42] Thermo, “Thermo Scientific Pierce Crosslinking Technical Handbook,” Ebooks, 2009.

[43] E. M. Czekanska, “Assessment of cell proliferation with resazurin-based fluorescent dye.,” Methods Mol. Biol., 2011.

[44] F. J. Reynoso, S.-K. Cheong, and S. H. Cho, “Implementation of a multisource model for gold nanoparticle-mediated plasmonic heating with near-infrared laser by the finite element method Chae-Deok Lee 073301-2 Reynoso et al.: Multisource model for gold nanoparticle-mediated plasmonic heating 073301-2,” Med. Phys, vol. 40, no. 7, pp. 73301–73302, 2013.

[45] H. Breitenborn et al., “Quantifying the photothermal conversion efficiency of plasmonic nanoparticles by means of terahertz radiation,” APL Photonics, vol. 4, no. 12, p. 126106, 2019.

[46] M. Noruzi, D. Zare, and D. Davoodi, “A rapid biosynthesis route for the preparation of gold nanoparticles by aqueous extract of cypress leaves at room temperature,” Spectrochim. Acta - Part A Mol. Biomol. Spectrosc., vol. 94, pp. 84–88, 2012.

[47] C. Malarkodi, S. Rajeshkumar, M. Vanaja, K. Paulkumar, G. Gnanajobitha, and G. Annadurai, “Eco-friendly synthesis and characterization of gold nanoparticles using Klebsiella pneumoniae,” J. Nanostructure Chem., vol. 3, no. 1, pp. 1–7, 2013.

[48] S. O. Dozie-Nwachukwu et al., “A comparative study of the adhesion of biosynthesized gold and conjugated gold/prodigiosin nanoparticles to triple negative breast cancer cells,” J. Mater. Sci. Mater. Med., vol. 28, no. 9, 2017.

[49] S. L. Smitha, D. Philip, and K. G. Gopchandran, “Green synthesis of gold nanoparticles using Cinnamomum zeylanicum leaf broth,” Spectrochim. Acta Part A Mol. Biomol. Spectrosc., vol. 74, no. 3, pp. 735–739, Oct. 2009.

[50] M. Kumari et al., “Physico-Chemical Condition Optimization during Biosynthesis lead to development of Improved and Catalytically Efficient Gold Nano Particles,” Sci. Rep., 2016.

[51] J. Kasthuri, S. Veerapandian, and N. Rajendiran, “Biological synthesis of silver and gold nanoparticles using apiin as reducing agent,” Colloids Surfaces B Biointerfaces, vol. 68, no. 1, pp. 55–60, Jan. 2009.

[52] J. L. G. Wade, Organic chemistry, 7th ed., vol. 250, no. 4. 2010.

[53] R. I. Priyadharshini, G. Prasannaraj, N. Geetha, and P. Venkatachalam, “Microwave-Mediated Extracellular Synthesis of Metallic Silver and Zinc Oxide Nanoparticles Using Macro-Algae (Gracilaria edulis) Extracts and Its Anticancer Activity Against Human PC3 Cell Lines,” Appl. Biochem. Biotechnol., vol. 174, no. 8, pp. 2777–2790, 2014.

[54] K. Kalimuthu, B. S. Cha, S. Kim, and K. S. Park, “Eco-friendly synthesis and biomedical applications of gold nanoparticles: A review,” Microchem. J., vol. 152, no. October 2019, p. 104296, 2020.

[55] L. F. Leopold et al., “Assessment of PEG and BSA-PEG gold nanoparticles cellular interaction,” Colloids Surfaces A Physicochem. Eng. Asp., vol. 532, no. July, pp. 70–76, 2017.

[56] B. Bahmani, S. Gupta, S. Upadhyayula, V. I. Vullev, and B. Anvari, “Effect of polyethylene glycol coatings on uptake of indocyanine green loaded nanocapsules by human spleen macrophages in vitro,” J. Biomed. Opt., vol. 16, no. 5, p. 051303, 2011.

[57] J. Hu, S. Youssefian, J. Obayemi, K. Malatesta, N. Rahbar, and W. Soboyejo, “Investigation of adhesive interactions in the specific targeting of Triptorelin-conjugated PEG-coated magnetite nanoparticles to breast cancer cells,” Acta Biomater., vol. 71, no. February, pp. 363–378, 2018.

[58] C. LibreTexts, “Infrared Spectroscopy Absorption Table,” 2019. [Online]. Available: https://chem.libretexts.org/Bookshelves/Ancillary_Materials/Reference/Reference_Tables/Spectroscopic_Parameters/Infrared_Spectroscopy_Absorption_Table.

[59] J. D. Obayemi et al., “Adhesion of ligand-conjugated biosynthesized magnetite nanoparticles to triple negative breast cancer cells,” J. Mech. Behav. Biomed. Mater., vol. 68, no. January, pp. 276–286, Apr. 2017.

[60] J. D. Obayemi et al., “Biosynthesis and the conjugation of magnetite nanoparticles with luteinizing hormone releasing hormone (LHRH).,” Mater. Sci. Eng. C. Mater. Biol. Appl., vol. 46C, pp. 482–496, 2015.

[61] K. Kan-Dapaah, N. Rahbar, and W. Soboyejo, “Polymeric composite devices for localized treatment of early-stage breast cancer,” PLoS One, vol. 12, no. 2, pp. 1–11, 2017.

Chapter 6.0. Summary and Conclusions

This thesis presents the results of a combined experimental, computational, and theoretical study of TNBC cells and non-tumorigenic breast cells and their interactions with biosynthesized triptorelin-conjugated PEG-coated gold nanoparticles that are relevant to triple negative breast cancer treatment. Salient conclusions arising from the study of the adhesion, entry, and photothermal properties of GNP, GNP-PEG, GNP-TRP, and GNP-PEG-TRP in TNBC/non-tumorigenic cells are presented.

1. Force microscopy measurements of the adhesion forces between TNBC cells and Triptorelin-functionalized gold nanoparticles (GNP-TRP and GNP-PEG-TRP) are much greater than the adhesion to non-tumorigenic breast cells. The increased adhesion of GNP-TRP and GNP-PEG-TRP to TNBC is also associated with the over-expression of LHRH receptors on the surfaces of TNBC cells. In addition, this increased adhesion enhances the selective adhesion of LHRH-conjugated gold nanoparticles to TNBC cells.
2. The PEG coating of biosynthesized gold nanoparticles reduces non-specific nanoparticle/cell interactions. It also has a favorable effect on the adhesion between GNP-PEG-TRP/ LHRH receptors . The repulsive interaction between the Triptorelin ligand/ cell membrane and PEG/cell membrane promotes specificity of the GNP-PEG-TRP/ LHRH TMD-n receptors interactions in TNBC. Therefore, the current results suggest that GNP-PEG-TRP nanoparticles could be suitable candidates for the specific targeting of TNBC cells that have over-expressed LHRH receptors on their surfaces.
3. GNP-PEG-TRP preferentially enters the TNBC cells than the non-tumorigenic cells. Furthermore, the selective accumulation of GNP-PEG-TRP in TNBC is also associated

with the over-expression of LHRH receptors on the surfaces of TNBC cells and the combination of PEG and TRP coatings. These enhance the selective uptake of GNP-PEG-TRP to TNBC cells.

4. The thermodynamics-kinetics model shows a critical nanoparticle cluster size for minimum wrapping time. For a finite cell membrane with conserved receptor density, cluster uptake is the number of receptors available for ligand binding and the diffusivity of such receptors. Hence, below a critical size, nanoparticle endocytosis is thermodynamically unfavorable and slow due to the rapid increase in the elastic bending energy. Alternately, when particles sizes are far above the critical size, wrapping is slow due to the diffusive nature of the receptor transport.
5. Thermodynamics-kinetics models also show that the surface energy effects of TRP functionalized gold nanoparticle clusters increase the free energy for wrapping such nanoparticle clusters.
6. The PEG coating of biosynthesized gold nanoparticles enhances uptake processes independent of the LHRH receptors. Furthermore, when PEG is used with the TRP ligand, it promotes the specificity of the GNP-PEG-TRP/ LHRH receptors interactions in TNBC. Therefore, the current results suggest that GNP-PEG-TRP nanoparticles could be suitable candidates for the specific targeting of TNBC cells that have over-expressed LHRH receptors on their surfaces.
7. Gold nanoparticle biosynthesis methods with Serratia Marscensces produce nanoparticles with well-defined optical properties in the NIR regime with minimal toxicities. Furthermore, the photothermal properties of these gold nanoparticles differ based on the surface modifications. This difference in photothermal properties is associated with the

changes in the rate of photon absorption and heat dissipation from surfaces of TNBC cells and chicken tissue.

8. The cell viability and heat shock protein expressions of heat-treated TNBC cells show that with laser irradiation, the biosynthesized gold nanoparticles can achieve temperatures sufficient for hyperthermia and induce cell death processes within treated TNBC cells.
9. The chicken tissue experiments demonstrate that the hyperthermic heating at depths of 6mm beneath the skin surface can be localized within the incised chicken tissue groove to limit high-temperature tissue damage in the surrounding tissue.
10. Robotics laser positioning can be achieved for applications that require guided laser beams with well-controlled power and wavelengths to interact with magnetite nanoparticles to induce heating that is sufficient to enable photothermal therapy via laser hyperthermia. Higher temperatures may also be generated at higher laser powers, which may be helpful in future robotically-assisted surgical procedures.

6.2. Suggestions for Future Work

1. Single-Molecule and Controlled Environment Adhesion Experiments

Adhesion experiments should be done in a physiological environment relevant to live cells to advance the studies on the adhesion between functionalized AFM probes and TNBCs. This can be done by quantifying single LHRH-TRP adhesion interactions and multiple receptor-ligand adhesion interactions in a fluid. Specifically by modifying the dip-coating AFM tip functionalization procedure and by using established protocols for single receptor-ligand interactions[1], [2].

Such adhesion studies could provide insights for using AFM adhesion probes to discriminate between TNBC and non-tumorigenic cells.

2. Cell Viscoelasticity Studies with Different Experimental Techniques

Further investigation into cell viscoelastic properties as diagnostic and prognostic biomarkers are still needed for TNBC. Therefore, there is a need for different experimental techniques that quantify single-cell viscosities and single-cell modulus for both treated and untreated TNBC. This could be achieved by shear flow deformation processes that enable time-dependent creep of cells and subsequently fitting such characteristic curves to viscoelastic models. In addition, the study of the viscoelastic properties of treated TNBC could provide quantitative markers for effective cancer progression and therapeutics.

3. Heat Effects on Surrounding Tissue after Laser Scalpel Experiments

It is essential to investigate the effects of laser power, speed of the robotic laser control, and heat on the surrounding tissue to advance the efforts toward precision nanoparticle-guided laser cutting. The effects of laser cutting could be studied via in vivo models that observe and compare the heat-induced structural and morphological changes within and adjacent to the damaged tissue zone.

4. Heat and Drug Effects on Triple Negative Breast Cancer Cells and Tissue

For targeted treatment of TNBC cells, in vitro and in vivo studies on the combined therapeutic effect of targeted drugs and targeted/localized hyperthermia should be investigated. This could be done sequentially by treating TNBC cells or in vivo models with targeted TNBC cancer drugs [3] and an optimized GNP-PEG-TRP nanoparticle designed for laser-assisted hyperthermia. Combining several therapeutic agents into a treatment protocol may enhance the effectiveness of current TNBC interventions. It could also provide insights into increasing cellular uptake of drugs and the reversal or depreciation of the cancer drug resistance in TNBC cells.

5. Heat Effects on Drug Delivery Systems

The use of hyperthermia-controlled drug release at the tumor site should be investigated for implantable biomedical devices developed for the localized treatment of residual TNBC following surgery. In this way, the thermodynamics and kinetics of controlled drug release as a function of laser-nanoparticle heating can be ascertained and used as a guide for safe and sustained chemotherapeutic doses to reduce the typical side effects associated with bulk/conventional and reduce the chances of tumor reoccurrence.

6.3 References

[1] D. Alsteens, H. E. Gaub, R. Newton, M. Pfreundschuh, C. Gerber, and D. J. Müller, "Atomic force microscopy-based characterization and design of biointerfaces," *Nat. Rev. Mater.*, vol. 2, no. 5, 2017.

[2] C. Lo Giudice, A. C. Dumitru, and D. Alsteens, "Probing ligand-receptor bonds in physiologically relevant conditions using AFM," *Anal. Bioanal. Chem.*, vol. 411, no. 25, pp. 6549–6559, 2019.

[3] J. D. Obayemi *et al.*, "LHRH-Conjugated Drugs as Targeted Therapeutic Agents for the Specific Targeting and Localized Treatment of Triple Negative Breast Cancer," *Sci. Rep.*, 2020.